Intense-field high-order harmonic generation: beyond the standard picture

VNiVERSiDAD
D SALAMANCA
CAMPUS DE EXCELENCIA INTERNACIONAL

José Antonio Pérez Hernández
Departamento de Física Aplicada

A thesis submitted for the degree of
Doctor of Philosophy (Physics) at the Universidad de Salamanca
Supervisor: Prof. Luis Plaja Rustein

LUIS PLAJA RUSTEIN, PROFESOR TITULAR DEL DEPARTAMENTO DE FÍSICA APLICADA DE LA UNIVERSIDAD DE SALAMANCA,

CERTIFICA:

Que el presente trabajo, "**Intense-field high-order harmonic generations: beyond the standard picture**" ha sido realizado bajo su dirección en el Área de Óptica del Departamento de Física Aplicada de la Universidad de Salamanca por José Antonio Pérez Hernández y constituye la Memoria que presenta para optar al Título de Doctor en Física.

Y para que así conste, firma la presente en

Salamanca, a 27 de Marzo de 2015.

Luis Plaja
Departamento de Física Aplicada
Universidad de Salamanca

Abstract

This thesis reports on theoretical investigation of the High-order Harmonic Generation (HHG) process beyond the standard procedure. According to the title, the term *beyond* refers to the fact we have developed and used an extension of the standard Strong-Field Approximation (SFA), denoted by us as SFA+. As we will see, this next order correction to the standard SFA consists of accounting for the ground-state dressing by the electromagnetic field. SFA+ has been developed in the standard framework of the S-matrix formalism without resorting to the saddle point approximation. Therefore it provides a compact, fully quantum (not semiclassical) description, allowing in many cases a more efficient computation. All results are tested against the 3D TDSE in a wide range of parameters, such as different pulse shapes, peak laser intensities and laser wavelengths.

In the second part of this thesis (chapter 3) we will expose two new proposals to achieve high energy photons via HHG. Again, in consistence with the title, in this case the term *beyond* accounts the fact that we study how to increase the harmonic cut-off in the HHG spectra by different techniques from the conventional approaches. Our first method consists of *sculpting* the driving laser pulse delaying in time two pulses of the same color and overlaping they with an adequate delay. The resulting waveform presents particular advantages, in comparision with the conventional approaches, to increase efficiently the harmonic cut-off. Our second proposal emerges from the study of the HHG at ultra-high laser intensities, exceeding the usual regime (tunnel regime) where the HHG takes place. The HHG process beyond the tunnel regime has been scarcely studied in the literature.

In this context a detailed study of the intra-cyle electron dynamics using classical trajectories as well as the full quantum analysis is carried out. Besides, the possibility of synthetising isolated attosecond pulses at this intensity regime, by means of *ionization gating*, is also investigated.

A mis padres y hermanas

Acknowledgements

Agradezco al Prof. Luis Plaja el tiempo y dedicación empleados en la tutela y dirección de esta tesis.

Al Prof. Luis Roso le agradezco el apoyo recibido, y que me diera la oportunidad de formar parte de su grupo cuando un estudiante recién licenciado fue a pedirle, un sitio, un rincón, para poder hacer lo que más le apasionaba (y le sigue apasionando): dedicarse en cuerpo y alma a la investigación científica.

Agradezco a mis compañeros del grupo de Óptica *El fotón Charro*, donde comenzó esta aventura, y de los que siempre tuve el apoyo de la gran mayoría. Guardo muy buenos recuerdos de aquellos días y de los momentos que compartí con ellos dentro y fuera del trabajo.

Agradezco a mis compañeros del Centro de Láseres Pulsados (CLPU), donde me ubico actualmente, y de los que también siempre he percibido un cálido y desinteresado apoyo en todo momento.

Agradezco el apoyo de todos los colegas que me he ido encontrando en este fascinante mundo de los Láseres Intensos, de los que he aprendido mucho y me he nutrido científicamente. El proceso continúa.

No puedo olvidarme de mis amigos, sin nombrar a ninguno, pero sin olvidarme de nadie, les agradezco por estar siempre ahí, en los buenos momentos y en los no tan buenos. GRACIAS!

Por último agradezco a mis padres (mención especial para mi madre) por su apoyo desde sus posibilidades, y por darme libertad para elegir y no imponerme en nigún momento nada por la fuerza. A mis hermanas les agradezco también el apoyo recibido.

Esta tésis ha sido desarrollada con el apoyo económico del proyecto Consolider SAUUL CSD2007-00013, y del proyecto FIS2009-09522 de la Junta de Castilla León así como con el apoyo del Centro de Láseres Pulsados (CLPU).

“ **¿ Qué signos revelan el talento creador y la vocación por la investigación científica?**

Problema grave, capitalísimo, sobre el cual han discurrido altos pensadores e insignes pedagogos, sin llegar a normas definitivas. La dificultad sube de punto considerando que no basta encontrar entendimientos perspicaces y aptos para las pesquisas de laboratorio sino conquistarlos definitivamente para el culto de la verdad original.

Los futuros sabios, blanco de nuestros desvelos educadores, ¿ se encuentran por ventura entre los discípulos más serios y aplicados, acaparadores de premios y triunfadores en oposiciones ?

Algunas veces, sí, pero no siempre. Si la regla fuera infalible, fácil resultaría la tarea del profesor, bastaríale dirigirse a los premios extraordinarios de la licenciatura y a los números primeros de las oposiciones a cátedras. Mas la realidad se complace a menudo en burlar previsiones y malograr esperanzas. Se da con desconsoladora frecuencia, el caso de que los más brillantes jóvenes son mentalidades exquisitamente prácticas, es decir, financieros refinadísimos en embrión. Estudian y se esfuerzan, más que por amor a la Ciencia, por hallarse persuadidos de que el saber constituye excelente negocio, y de que la buena fama cobrada en la escuela cotízase muy alto en el mercado profesional y en las esferas académicas.

Si el lector sonríe ante esta observación, haga memoria y repare en qué vinieron a parar sus más sobresalientes condiscípulos, los monstruos de la memoria y de la aplicación, aquellos en quienes el profesor ponía todos sus mimos y preferencias, y reconocerá con pena que, si en su mayor parte alcanzaron holgada posición social (y en esto no erraron sus cálculos), poquísimos o ninguno ascendieron a las cumbres del saber o se distinguieron por una acción poltica, social o industrial abnegada y fecunda.

Harto más merecedores de predilección para el maestro avisado serán aquellos discípulos un tanto indómitos, desdeñosos de los primeros lugares, insensibles al estímulo de la vanidad, que, dotados de rica e inquieta fantasía, gastan el sobrante de su actividad en la literatura, el dibujo, la filosofía y todos los deportes del espíritu y del cuerpo. Para quien los sigue de lejos, parece como que se dispersan y se disipan, cuando, en realidad, se encauzan y fortalecen. Corazones generosos, poetas a ratos, románticos siempre, estos jóvenes distraídos poseen dos cualidades esenciales de las que el maestro puede sacar gran partido: desdén por el lucro y las *altas posiciones académicas, y espíritu caballeresco enamorado de altos ideales. Al revés de los otros, al abandonar las aulas es cuando realmente comienzan a estudiar y no es raro verlos fatigados ya de elaborar sin provecho, y faltos de orientación definida, presentarse en los laboratorios en súplica de consejos técnicos y de un tema de estudio.*

Con todo eso, los rasgos precedentes no constituyen siempre síndrome cierto del futuro hombre de ciencia. Entre quienes sobresalen aquéllos abundan veleidades y defecciones. Las citadas cualidades representan fuerzas en potencia, que no siempre llegan a ser actuales. Seducido por las apariencias, el maestro corre el riesgo de educar dilettantes del laboratorio o talentos brillantes, pero incapaces de honda y perseverante labor. Resulta, pues, difícil el diagnóstico de la vocación científica. Preciso es apelar a signos más exactamente diferenciadores para discernir la moneda falsa del oro de ley. En su libro sobre los Grandes Hombres, W. Ostwald añade,

” La más importante cualidad del sabio es la originalidad, es decir, la capacidad de imaginar alguna cosa más allá de lo que se enseña; la exactitud en el trabajo, la crítica de sí mismo, conciencia, conocimientos, destreza, son también necesarios, pero esto puede adquirirse más tarde, mediante conveniente educación ”

Así pues, cuando el novel investigador pueda marchar por sí mismo, procúrese imbuirle el gusto por la originalidad. Déjese, pues, sugerir en él la idea nueva con plena espontaneidad, aunque esta idea no concuerde con las teorías de la escuela”.

Santiago Ramón y Cajal, *Reglas y Consejos para el joven investigador*

Contents

List of Publications xi

List of Figures xv

List of Tables xxvii

1 Introduction 1

- 1.1 Laser-atom interaction 1
- 1.2 High-order Harmonic Generation 1
- 1.3 Models for High-order Harmonic Generation 3
  - 1.3.1 Direct resolution of the three Dimensional Time-Dependent Schrödinger Equation 3
  - 1.3.2 The classical Three Step Model 6
  - 1.3.3 Strong Field Approximation for HHG: Lewenstein model . 9
- 1.4 Attosecond pulses 11

2 SFA+ formalism 15

- 2.1 Derivation of SFA+: P and Q projections 15
- 2.2 Test of SFA+ versus SFA and 3D TDSE 22
  - 2.2.1 SFA+ harmonic espectra versus SFA and 3D TDSE 22
  - 2.2.2 Scaling of the harmonic yield with the laser wavelength . 28
  - 2.2.3 Phase and temporal description of the high-order harmonic radiation 34
- 2.3 Full quantum aspects of SFA+ 40
  - 2.3.1 Momentum space description 40

2.3.2 Semiclassical and quantum aspects of harmonic generation via SFA+. Electron wavepacket delocalization 42
2.4 Results for other atomic species: He 47

3 HHG and Attosecond Pulse Generation beyond saturation 51
3.1 Challenges, goals and the problem of saturation in HHG 51
3.2 Extension of the cut-off in HHG using two delayed pulses of the same colour 53
3.3 Potential applications and conclusions 67
3.4 HHG at ultra-high laser intensities: Non Adiabatic Turn-on driving laser pulses 68
3.4.1 Classical analysis 69
3.4.2 Full quantum description: 3D TDSE quantum analysis . . 71
3.4.2.1 Harmonic spectrum 74
3.4.3 Ionization gating with NAT pulses 78
3.5 Attosecond synthesis from NAT pulses 80
3.5.1 Harmonic phase extraction 80

4 Conclusions 85

A Derivation I 87
A.1 From Eqs.(2.4),(2.5) to Eqs.(2.8),(2.9), respectively 87

B Derivation II 91
B.1 From Eqs.(2.8),(2.9) to Eq. (2.14) 91

C Derivation III 93
C.1 Wavepacked spreading: Derivation of Eq. (2.17) 93

D Derivation IV 95
D.1 Derivation of the level shift (Eq. (2.18)). 95

E Derivation V 97
E.1 Derivation of Eq. (2.19) 97

F Derivation VI **99**

F.1 Derivation of Eq. (2.20) 99

References **103**

List of Publications

This thesis is supported by the following publications:

1. A quantitative S-Matrix approach to high-order harmonic generation from multiphoton to tunneling regimes.
   L. Plaja and J. A. Pérez-Hernández,
   Optics Express **15**, 3629-3634 (2007)

2. Quantum description of the high-order harmonic generation in multiphoton and tunneling regimes.
   J. A. Pérez-Hernández and L. Plaja,
   Physical Review A **76**, 023829-1-7 (2007)

3. Harmonic generation beyond the Strong-Field Approximation: the physics behind the short-wave-infrared scaling laws.
   J. A. Pérez-Hernández, L. Roso and L. Plaja,
   Optics Express **17**, 9891-9903 (2009)

4. Extension of the cut-off in high-harmonic generation using two delayed pulses of the same colour.
   J. A. Pérez-Hernández, D. J. Hoffmann, A. Zaïr, L. E. Chipperfield, L. Plaja, C. Ruiz, J. P. Marangos and L. Roso,
   J. Phys. B: At. Mol. and Opt. Phys. **42**, 134004-1-8 (2009)

5. A quantitative-accurate S-matrix model for the description high-order harmonic generation.
   J. A. Pérez-Hernández and L. Plaja,
   Eur. Phys. J-Special Topics **175**, 21-24 (2009)

6. S-Matrix Theory for the High-Order Harmonic Generation beyond the Strong-Field Approximation.
   J. A. Pérez-Hernández, L. Roso and L. Plaja,
   Laser Phys. **19**, 1581-1585 (2009)

7. Harmonic Generation Beyond the Strong-Field Approximation: Phase and Temporal Description.
   J. A. Pérez-Hernández, J. Ramos, L. Roso and L. Plaja,
   Laser Phys. **20**, 1044-1050 (2010)

8. New methods for computing high-order harmonic generation and propagation.
   J. A. Pérez-Hernández, C. Hernández-García, J. Ramos, E. Conejero, L. Plaja and L. Roso,
   Book Chapter:*Progress in Ultrafast Intense Laser Science VII (pp 145-162), Springer (2011)* ISBN 978-3-642-18326-3

9. Valley in the efficiency of the high-order harmonic yield at ultra-high laser intensities.
   J. A. Pérez-Hernández, L. Roso, A. Zaïr and L. Plaja,
   Optics Express **19**, 19430-19439 (2011)

10. Comment on " On the dipole, velocity and acceleration forms in high-order harmonic generation from a single atom or molecule "
    J. A. Pérez-Hernández and L. Plaja,
    J. Phys. B: At. Mol. and Opt. Phys. **45**, 028001 (2012)

11. Perspectives for the generation of intense isolated attosecond pulses at ultra-high laser intensities.
    J. A. Pérez-Hernández and L. Roso,
    Book Chapter:*Springer Series in Optical Sciences. Attosecond Physics, Volume* **177**, *pp 33-45 (2013)* DOI 10.1007/978-3-642-37623-8_3

In addition, below is reported another set of publications not included in this thesis but focussed in the same research line which have been carried out by the author recently:

1. Above-threshold ionization by few-cycle spatially inhomogeneous fields.
   M. F. Ciappina, J. A. Pérez-Hernández, T. Shaaran, J. Biegert, R. Quidant and M. Lewenstein,
   Physical Review A **86**, 023413 (2012)

2. Beyond Carbon K-Edge Harmonic Emission Using a Spatial and Temporal Synthesized Laser Field.
   J. A. Pérez-Hernández, M. F. Ciappina, M. Lewenstein, L. Roso and A. Zaïr,
   Physical Review Letters **110**, 053001-5 (2013)

3. Electron-momentum distributions and photoelectron spectra of atoms driven by an intense spatially inhomogeneous field.
   M. F. Ciappina, J. A. Pérez-Hernández, T. Shaaran, L. Roso and M. Lewenstein,
   Physical Review A **87**, 063833 (2013)

4. High-order-harmonic generation by enhanced plasmonic near-fields in metal nanoparticles.
   T. Shaaran, M. F. Ciappina, R. Guichard, J. A. Pérez-Hernández, L. Roso, M. Arnold, T. Siegel, A. Zaïr and M. Lewenstein,
   Physical Review A (Rapid Communications) **87**, 041402(R) (2013)

5. High energy photoelectron emission from gases using plasmonics enhanced near-fields.
   M. F. Ciappina, T. Shaaran, R. Guichard, J. A. Pérez-Hernández, L. Roso, M. Arnold, T. Siegel, A. Zaïr and M. Lewenstein,
   Laser Physics Letters **10**, 105302 (2013)

6. ClassSTRONG: Classical simulations of Strong Field processes.
   M. F. Ciappina, J. A. Pérez-Hernández and M. Lewenstein,
   Computer Physics Communications **185**, pp 398-406 (2014)

7. High-order harmonic generation driven by metal nanotip photoemission: theory and simulations
   M. F. Ciappina, J. A. Pérez-Hernández, M. Lewenstein, M. Krüger and P. Hommelhoff,
   Physical Review A **89**, 013409 (2014)

8. Coherent XUV generation driven by sharp metal tips photoemission
   Marcelo F. Ciappina, Jose Antonio Pérez-Hernández, Tahir Shaaran, Maciej Lewenstein,
   European Physical Journal D **68**, 172 (2014)

9. High-order harmonic generation driven by plasmonic fields: a new route towards the generation of UV and XUV photons?
   M. F. Ciappina, J. A. Pérez-Hernández, L. Roso, A. Zaïr and M. Lewenstein,
   MPS2014 proceedings, accepted, in press

List of Figures

1.1 Schematic representation of a typical high-order harmonic spectrum resulting from the interaction of an intense laser pulse with a gas of atoms, molecules or ions. 2

1.2 Schematic representation of the dipolar approximation. The typical Ti-Sapphire laser wavelength ($\sim$ 800 nm) is much larger than the the atomic dimensions. In this context the laser field can be considered spatially independent in the zone where the interaction occurs. Under these conditions the Eq. (1.1) represents a realistic approximation. 4

1.3 Effect of the magnetic field of the Lorentz force on the ionized electron and its subsequent recombination with the parent ion. As it is shown in (a), when the electron's velocity is low compared with c, Eq. (1.2) is a reasonable approximation. However, in case that the electron's velocity is closer to c, the magnetic component exerts an important effect on the ionized electron deflecting it from the optimum recombination trajectory as it is shown in (b). . . . 5

1.4 (a) Schematic representation of the classical three step recolision model. (b) Electron kinetic energy (in U_p units) as a function of the phase (ϕ) of the field at the instant of ionization. Blue line and black line represent the ionization and recombination events, respectively. 7

2.1 Laser-atom interaction picture treated under P and Q formalism . 17

2.2 HHG spectra in hydrogen atom computed with SFA+ (green), SFA (red) and 3D TDSE (blue), (this color criteria will be used in the folowing) for four different laser intensities, (a) $5.06 \times 10^{13} W/cm^2$, (b) $8.77{\times}10^{13} W/cm^2$, (c) $1.26{\times}10^{14} W/cm^2$ and (d) 1.57 $\times 10^{14} W/cm^2$. All of them are computed at $800nm$. Note that panels (a) and (b) represent the two cases in multiphoton regime ($\Gamma_K = 1.5$ and $\Gamma_K = 1.14$ respectively) and cases (c) $\Gamma_K = 0.95$ and (d) $\Gamma_K = 0.85$, belong to the tunnel regime. We have used 4-cycle sin^2 pulse envelope. 23

2.3 HHG spectra in hydrogen for two different laser intensities and two different laser wavelengths. Panels (a) and (b) represent the espectra computed both at the same intensity, $5.06 \times 10^{13} W/cm^2$. Panels (c) and (d) are computed both at $8.77 \times 10^{13} W/cm^2$. Panels (a) and (c) are computed at 800nm and panels (b) and (d) correspond to 1600nm. In (a) $\Gamma_K = 1.5$, in (b) and $\Gamma_K = 0.75$, in (c) $\Gamma_K = 0.95$ and in (d) $\Gamma_K = 0.57$. We have used 4-cycle sin^2 pulse envelope. 24

2.4 HHG spectra in hydrogen at four different laser wavelengts, (a) $800nm$, (b) $1000nm$, (c) $1400nm$ and (d) $1600nm$. All cases are computed at the same laser intensity $I = 1.57 \times 10^{14} W/cm^2$. Here, in (a) $\Gamma_K = 0.85$, in (b) $\Gamma_K = 0.68$, in (c) $\Gamma_K = 0.48$ and in (d) $\Gamma_K = 0.42$. The respective insets represent a zoom of the cut-off zone. We have used 4-cycle sin^2 envelope plotted in panel (e). . . 25

2.5 Identical parmeters than in Fig. 2.4 but in this case we have used a 6-cycles trapezoidal shape with 2-cycles of turn-on, 2-cycles of flat-top and two cycles of turn-off plotted in panel (e). 26

2.6 The same as in Fig. 2.4 and Fig. 2.5 but here we have used a 9-cycles trapezoidal shape, with 1/2 of turn-on, 8 cycles of flat-top and 1/2 of turn-off (panel (e)) 27

2.7 Harmonic spectra resulting from the exact integration of the 3D TDSE (blue), SFA in $\mathbf{E}\cdot\mathbf{r}$ and $\mathbf{p}\cdot\mathbf{A}$ gauges (red and orange) and SFA+ (green). Part (a) shows the location of the spectral windows used to compute the harmonic yield in [35, 40, 41] (enclosed between red dashed lines) and the considered here (enclosed between black dashed lines). Part (b) shows the results of the exact 3D TDSE and the three models in the former case (red dashed window). The computation corresponds to a trapezoidal shape of 6 cycles (with 2 cycles of linear turn-on, 2 cycles of constant amplitude and 2 cycles of linear turn-off), peak intensity $I = 1.58 \times 10^{14}$ and wavelength 1600 nm. 30

2.8 Higher frequency part of the HHG spectrum for a 6 cycles driving field of intensity 1.58×10^{14} W/cm^2 and wavelengths 800 nm (a) and 1600 nm (b). Part (b) corresponds to the same case shown in Fig. 2.7. As before, 3D TDSE results are plotted in blue, SFA in red (length gauge) and orange (velocity gauge), and the results of the SFA+ are plotted in green. The limits of the window used to compute the yields of table 2.2 are shown in black dashed lines. . 31

2.9 Harmonic yields computed using the window at the end of the plateau for a 6-cycle pulse of $I = 1.58 \times 10^{14}$ and for wavelengths ranging from 800 to 1600 nm. (a) Comparison between results from the 3D TDSE (blue) and the SFA+ (green), (b) comparison of the 3D TDSE (blue) with the SFA in length (red) and velocity (orange) gauges. 34

2.10 HHG spectra in hydrogen corresponding to a four-cycle sin^2 envelope and peak intensity $1.57 \times 10^{14} W/cm^2$ at $800nm$, computed with the SFA+ (green), SFA (red) and 3D TDSE (blue). 35

2.11 Time-frequency analysis corresponding to the spectra shown in Fig. 2.10: (a) the exact 3D TDSE (b) SFA+ (not rescaled), (c) SFA (rescaled to the same intensity level than the previous cases). The dotted white line represent the driving laser puse. 36

2.12 Harmonic intensity (red, blue and dotted black lines, respectively) and first derivative of the spectral phase, $d\phi(\omega)/d\omega$ (grey line), close to the cut-off for the computations shown in Fig. 2.10. (a) exact results from the 3D TDSE, (b) results from SFA+, and (c) results from the SFA. 38

2.13 Envelopes of the XUV electromagnetic fields resulting from the Fourier synthesis of the last part of the spectrum of Fig. 2.10 (starting from the 21st harmonic). (a) exact results from the 3D TDSE, (b) results from SFA+ model, and (c) results from the SFA. . . . 39

2.14 k_z spectral contributions to the total harmonic radiation corresponding to two different laser intensities, (a) $5.0 \times 10^{13} W/cm^2$ and (b) $3.50 \times 10^{14} W/cm^2$ both at $800nm$, computed with the SFA+. Vertical dashed lines represent the maximum cut-off frequency ($I_p+3.17U_p$) of the integrated spectrum which corresponds to the electrons returning to the atomic core. The vertical dotted lines denote the maximum kinetic energy of the trajectories of the non-returning electrons, $I_p + 8U_p$. The harmonic intensities are plotted in logarithmic scale 41

2.15 (a) electric field (red line) and kinetic energy (black line) associated with the classical trajectory of an electron assumed to be ionized near the peak amplitude (blue arrow). (b) electron trajectory associated to this situation (black line) and dipole's acceleration (in time) computed from SFA+ for the corresponding time window for the multiphoton case of Fig. 2.14(a). (c) the same for the tunnel case of Fig. 2.14(b). The inset shows a zoom of the acceleration close the classical time for recollision. The meaning of the shadow areas in (b) and (c) is explained in the text. 44

2.16 (a) electric field (red line) and kinetic energy (black line) associated with the classical trajectory of an electron assumed to be ionized at the field's zero (blue arrow). (b) electron trajectory associated to this situation (black line) and dipole's acceleration computed from SFA+ for the corresponding time window for the multiphoton case of Fig. 2.14(a). (c) the same for the tunnel case of Fig. 2.14(b). . 45

2.17 Schematic picture of an multi-electron atom in the SAE approximation which assumes that all electrons remain *frozen* in the orbitals forming a core and only one electron (the most external) interacts with the laser field. 47

2.18 HHG spectra in helium atom for two different laser intensities and two different laser wavelengths. Panels (a) and (b) represent the espectra computed both at the same intensity, $5.0 \times 10^{13} W/cm^2$. Panels (c) and (d) are computed both at $3.50 \times 10^{14} W/cm^2$. In addition, panels (a) and (c) are computed at 800nm and panels (b) and (d) correspond to 1600nm. In (a) $\Gamma_K = 1.14$, in (b) and $\Gamma_K = 0.57$, in (c) $\Gamma_K = 0.76$ and in (d) $\Gamma_K = 0.38$. We have used 4-cycle sin^2 pulse envelope. 48

3.1 The typical power spectrum of HHG in the nonperturbative regime where we show schematically the main challenges for HHG optimization. 52

3.2 Scheme of the pulse synthesis. (a) for the delay $\tau = 2T$ where two pulses do not overlap. (b) Both pulses are overlapped for the delay $\tau \approx \pm 0.81T$ wich is foud optimal for the extension of the harmonic spectrum. Note that the peak amplitude of the resultant field, plotted in (b), is always lower than the maximum amplitude of the input replicas as it is denoted by the horizontal black dotted lines. The pulse envelopes are shown in grey dotted lines which account of the envelope maximum E_0. 55

3.3 3D TDSE harmonic spectrum in hydrogen at 1.57×10^{14} W/cm^2 for an isolated pulse of $N = 2$ (in yellow) and for the double pulse (in green). A clear extension of the cut-off up to $5.5U_p + I_p$ is observed for the optimum delay $\tau \approx \pm 0.81T$. 56

3.4 Harmonic spectra as a function of delay between the both *sin-like* replicas. (a) For pulses of $N = 2$ cycles and $I = 10^{14}$ W/cm^2. The two maxima at $\tau \approx \pm 0.5T$ are well explained by a the increase of the laser field amplitude, as the two delayed pulses interfere constructively, while at $\tau \approx \pm 0.81T$ the harmonics extend up to $5.5U_p + I_p$ despite the fieldś amplitude remains below E_0. (b) For pulses of $N = 3$ cycles and $I = 10^{14}$ W/cm^2, a similar behaviour is observed, but with optimum extension now around $4.7U_p + I_p$ at $\tau \approx \pm 0.81T$. 57

3.5 The same scheme that in the Fig. 3.4 but in this case in saturation regime. (a) For pulses of $N = 2$ and 3.0×10^{14} W/cm^2, the extension of the cut-off up to $5.5U_p + I_p$ for delays of $\tau \approx \pm 0.81T$ is preserved. The peak at $\tau \approx \pm 0.5T$ that was present at lower intensities is not observed due to the suppression of the harmonic yield at field amplitudes above saturation.(b) For pulses of $N = 3$ and 3.0×10^{14}W/cm^2, a clear, though slightly smaller extension is again observed for delays of $\tau \approx \pm 0.81T$. 58

3.6 3D TDSE Harmonic spectra at 1.57×10^{14} W/cm^2 for a isolated pulse of $N = 2$ (in yellow) and for the double pulse synthesis (in green). A clear extension of the cut-off up to $5.5U_p + I_p$ is observed for the optimum delay $\tau \approx \pm 0.81T$ in hydrogen (a) and argon (b). 59

3.7 Comparison of 3D TDSE harmonic spectra (a) and the corresponding time-frequency analysis (b) resulting from the double pulse synthesis for the optimum parameters ($N = 2$, $\tau \approx \pm 0.81T$) and $I = 1.57 \times 10^{14}$ W/cm^2, $800nm$. In the time-frequency analysis (panel (b)) is superimposed as black triangles the values corresponding to the rescattering energies of the various classical trajectories generating the harmonic spectra. Three important emission events are observed. The central event at around $1.75T$ is responsible for the highest harmonics and cut-off extension, whilst other events contribute only to the lower harmonics. 60

3.8 (a) Ionization (in grey circles) and recombination energies (in black) resulting from the classical analysis of the isolated sin-like pulse (plotted in red in (b)). (c) similar to (a) but for the case of the double pulse configuration plotted in (b) in solid blue. Points 1 and 2 denote the instant when the electron ionizes and recombines respectively with the maximum energy for the case of isolated sin-like pulse. Points 3 and 4 denote the same for the double pulse synthesis. Note that in the case of double pulse configuration (panel (c)) energies up to $5.5U_p$ are achieved. Note also that in spite of both pulses are identical in the first cycle (see panel (b)) the ionization and recombination events present a temporal shift (see vertical dotted lines) enhancing the ionization-recombination window respect to the isolated pulse. 62

3.9 Panel (a) shows two different types of electron trajectories corresponding to the maximum energy recombination for the isolated sin-like pulse (in solid red line) and for the double pulse synthesis (in solid blue). Note that the velocity in the recombination instant is different. This fact is denoted (qualitatively) by the respective geometrical tangents plotted in solid grey. Giving the same color criteria, panel (b) quantitative shows the velocity which electron recombines giving the trajectories plotted in (a). The vertical arrows shows the recombination instant in both panels. Note that in the case of the double pulse the recombination velocity (solid blue in (b)) is considerably higher than in the isolated pulse (in solid red). In both panels the laser field amplitudes are plotted in dotted lines, in red for the isolated pulse and in blue for the double pulse configuration. 63

3.10 3D TDSE harmonic spectra in hydrogen at $\lambda = 800nm$ resulting from the sin-like isolated pulse of 4 cycles (in yellow) and from the double pulse synthesis for the case of 4 cycles shifted by CEP=π in one of the replicas (in green) and optimum delay τ=1.71 and no shifted (CEP=0) in pink, with delay τ=1.29T. Note that the extension is considerably reduced around $I_p + 4.5Up$. The laser intensity is $I = 1.57 \times 10^{14}$ W/cm^2. Note however that for these longer pulses the CEP is less relevant producing similar extension for the two shaped pulses with different values of the CEP (green and pink spectra). 64

3.11 Idem that the Fig. 3.10 but in this case at $\lambda = 1600nm$. In the case of the doble pulse synthesis, here only have plotted (in green) the case for CEP=0, i.e. not shifted. Note that here the cut-off increases around $49eV$ according to the $I_p + 4.5Up$ prediction. . . 65

3.12 Cut-off scaling as a function of the laser wavelength for the double pulse configuration ($N = 2$ in red), for the double pulse configuration ($N = 4$ in blue) and for the isolated sin-like pulse (in black). The laser intensity is 1.57×10^{14} W/cm^2. Note that in order to predict quantitatively the cut-off spectrum in each particular case, the I_p of the corresponding atom must be taken into account. . . 66

3.13 Recombination (first rescatering) energies of ionized electrons as a function of the ionization time (grey circles) and recombination time (black triangles), for three different driving laser pulses: (a) constant envelope, and (b) and (c) as described in Eq. (3.2) with (b) $\phi = 0$ and (c) $\phi = \pi/2$. The driving field used in each case is shown in red solid lines. Note that for the case $\phi = 0$ (panel b), a new set of trajectories emerges in the turn-on, labeled as NAT. . . 70

3.14 A detailed view of Fig. 3.13(b) ($\phi = 0$) in which is highlighted the NAT trajectories emerging in the turn-on. Note that in this case the electrons ionized at the beginning of the laser pulse (in the early turn-on), recombine during the first cycle with energies around $0.5U_p$. 71

3.15 Estimations of (a) the relative contributions to the harmonic yield at $W_0 = 73$ eV, (b) the probability amplitude of the ground state, and (c) the corresponding continuum state at the moment of recollision for the sets of trajectories highlighted in Fig. 3.13(b). Contributions of NAT trajectories are shown as red circles, long trajectories as open squares and short as blue triangles. The dashed line in (a) is a sketch of the resulting valley structure for the total radiation yield (sum of the above contributions). The laser amplitudes E are given in atomic units (a.u.), corresponding to intensities $E^2 \times 3.5 \times 10^{16} W/cm^2$. 73

3.16 Spectra resulting from the exact integration of the 3-dimensional time dependent Schrödinger equation in hydrogen for the laser pulse described in Eq. (3.2) with $\phi = 0$ (Fig. 3.13(b)), for different values of the field intensity: threshold of saturation ($I = 3.5 \times 10^{14}$ W/cm^2, light grey line), saturation ($I = 5.6 \times 10^{15}$ W/cm^2, blue line) and deep saturation ($I = 4.2 \times 10^{16}$ W/cm^2, red line). 75

3.17 Full 3D TDSE spectrum for the deep saturation case in hydrogen. The water window region (283 eV-583 eV) is delimited by the yellow area. The arrow points the estimated cut-off frequency $\simeq I_p + 0.5U_p$, associated to NAT trajectories. 76

3.18 Time-frequency analysis of the dipole acceleration extracted from the numerical resolution of 3D TDSE, and (superimposed) classical rescattering energies of electrons as a function of the recombination time (black triangles) for the three laser intensities used in Fig. 3.16 (threshold of saturation ($I = 3.5 \times 10^{14}$ W/cm^2, light grey line), saturation ($I = 5.6 \times 10^{15}$ W/cm^2, blue line) and deep saturation ($I = 4.2 \times 10^{16}$ W/cm^2, red line)). 77

3.19 The same parameters as in Fig. 3.16 but here including small fluctuations in the CEP in the case of the deep saturation intensity (green, red and black lines). Note that as long as the CEP fluctuations are small ($\pm 0.1\pi$ rad) the harmonic efficiency practically remains unaltered. 78

3.20 (a) NAT-type driving laser pulses with the same turn-on and different length. In solid grey is plotted the pulse described by Eq. (3.2) with $\phi = 0$. In solid blue is ploted a pulse with the same turn-on as that plotted in grey, but now, followed by two cycles of constant amplitude. The dotted grey lines represent the ground state population corresponding to the pulse in solid grey and the dotted blue lines represent the ground state population related to the pulse in solid blue. The horizontal red band delimits the estimated value of the barrier suppression for hydrogen. In (b) are plotted harmonic spectra in hydrogen generated by each one of driving laser pulses plotted in (a). The dotted grey line represents the spectrum generated by the driving laser pulse shown in solid grey in (a). The spectrum drawn in solid blue corresponds to the pulse plotted in solid blue in (a). 79

3.21 HHG spectra (in red) generated by NAT pulses and the corresponding emission times (in blue) for the threshold of saturation intensity (a) and deep saturation (b). 81

3.22 Temporal synthesis from HHG spectra in hydrogen. Plot (a) represents the HHG spectrum in threshold of ionization and plot (b) represents the deep saturation regime generated by NAT pulses (for the same parameters that in Fig. 3.20(b)). In both the HHG spectra are ploted in solid red line and the ionization times are ploted in solid blue line. The yellow area delimits the high-pass filter used (note that is identical in both cases, from 0 to 30st harmonic order). Plots (c) and (d) shows the corresponding sub-femtosecond temporal structures, respectively. The respective insets, (e) and (f), represent the zoom of these temporal structures. Note that the x-axes in the insets have been changed to attosecond units. . . 82

3.23 Temporal synthesis in the deep saturation regime for hydrogen (the parameters are the same of Fig. 3.20(b)). In this case the high pass filter used (in yellow) covers a wide zone in the harmonic spectrum (from 0 to 800st harmonic order). Note also that here the attosecond waveform is very narrow (see inset (c)) comparing with the cases of Fig. 3.22(d-f). Note, however that the attosecond intensity in this case drops orders of magnitude. 83

List of Tables

2.1 Exponents n of the scalings λ^{-n} of the harmonic yields computed from the exact integration of the 3D TDSE at an intensity $I = 1.58\times10^{14}$ using a fixed energy window (20-50 eV, enclosed between red lines shown in Fig. 2.7(a)), using a 10.2 eV window below the cut-off frequency ω_c (enclosed between black lines in Fig. 2.7(a)) and of the harmonic power at the nearest harmonic to the cut-off frequency. SFA+ result for the case of the fixed window and the field of 9 cycles agrees with the one reported in [41]. 32

2.2 Scaling exponents of λ^{-n} extracted from the harmonic yields computed at the final part of the plateau for the three approaches considered and the 3D TDSE (also shown in the third column of table 2.1). The cases labelled as 6-cycles correspond to the results shown in Fig. 2.9. 33

1

Introduction

> *“ Light and matter are both single entities, and the apparent duality arises in the limitations of our language ”*
> *Werner Karl Heisenberg*

1.1 Laser-atom interaction

The atomic response to a strong laser field produces a large number of physical phenomena of non linear nature. This thesis is focused on the study of one of these processes known as High-order Harmonic Generation (HHG). The progress of laser technology from its first realization in 1960 [1], has led to extraordinary development of table-top intense sources (mainly based in the CPA tecnology [2]) centered in the near infrared and visible wavelength region. HHG constitutes the ”bridge” to translate the coherence of the near infrared and visible wavelengths to the extreme-ultraviolet XUV and x-ray regions. In addition, in the temporal domain, HHG process provides a direct route to achieve the production ultra-short laser pulses of attosecond duration [4, 5].

1.2 High-order Harmonic Generation

A quite fascinating aspect of intense laser-matter interactions is the interplay of atomic physics in the strong field regime and non linear optics. The singular properties of the harmonic emission (ultrashort pulse duration, spatial and temporal coherence, high brightness) make it an unique and unprecedented source of XUV radiation, used in a wide number of research areas and applications, as atomic and molecular physics, solid state physics, plasma physics, chemistry and biology.

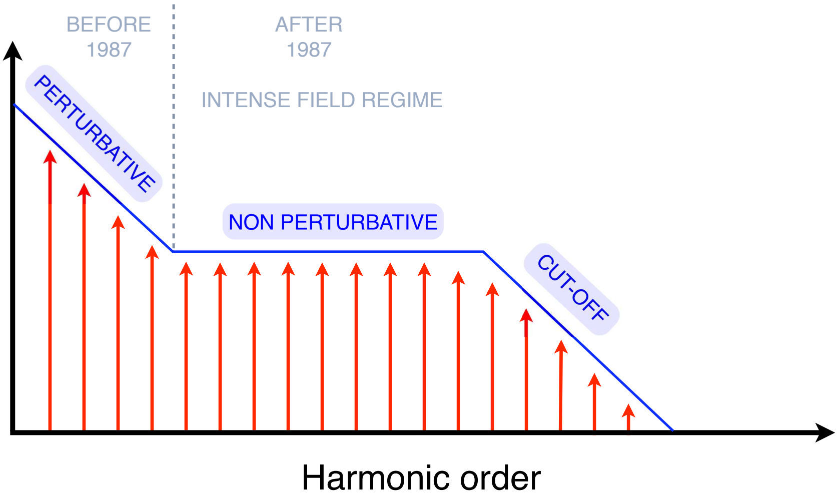

Figure 1.1: Schematic representation of a typical high-order harmonic spectrum resulting from the interaction of an intense laser pulse with a gas of atoms, molecules or ions.

HHG was experimentally observed in 1977, first in plasmas by Burnett *et al.* [6] and ten years later in gases by McPherson *et al.* [7] and Ferray *et al.* [8]. When an intense laser pulse is focused into a jet of noble gas, the non-linear interaction results in a spectrum of odd harmonics, whose amplitudes are approximately equal over a large spectral range, *plateau*, followed by an abrupt decrease, the *cut-off* region. This spectral shape differs strongly from the perturbative prediction, confirming that HHG results from a non-perturbative non-linear process. Consequently non-perturbative theoretical approaches are neccesary to the study of HHG. These will be exposed in the following section.

1.3 Models for High-order Harmonic Generation

Below, we will present briefly some main routes for the study of HHG process: The exact solution of the time-dependent Schrödinger equation, the classical Three Step Model and the Strong Field Approximation (SFA) approach to HHG.

1.3.1 Direct resolution of the three Dimensional Time-Dependent Schrödinger Equation

The interaction of an atomic electron with an electromagnetic field is described in the non-relativistic regime by the 3-dimensional time dependent Schrödinger equation (3D TDSE) [9, 10, 11, 12]. In the context of HHG some approximations are usually done. First of them is considering that the nucleus has an infinite mass (i.e. the nucleus remains frozen). Second, in the non relativistic regime, the electron spin is not coupled with the field. Consequently the electron can be assumed as a spinless particle. On the other hand, HHG is generally considered as a single-active electron process, although presently the many body aspects are currently being addressed [13]. In addition, the dipole approximation can be used, or in other words, the spatial dependence of the electromagnetic field can be neglected (see Fig. 1.2),

$$\mathbf{E}(\mathbf{r},t) \simeq \mathbf{E}(t) = \mathbf{E_o} f(t) sin(\omega_0 t + \phi). \tag{1.1}$$

where ω_0 is the laser frequency, $\mathbf{E_0}$ is the maximum field amplitude, *f(t)* is the pulse envelope and ϕ is the carrier envelope phase (CEP).

Last but not least, the magnetic drift that the ionized electron suffers due to the Lorentz force can be also neglected as long as it is non-relativistic (see Fig. 1.3), since the magnetic component of the Lorentz force is proportional to $(1/c)$.

$$\mathbf{F(t)}_{Lorenzt} = q\mathbf{E}(t) + \frac{q}{c}[\mathbf{V} \times \mathbf{B}] \equiv \mathbf{F}_{Electric} + \mathbf{F}_{Magnetic} \simeq \mathbf{F}_{Electric} \tag{1.2}$$

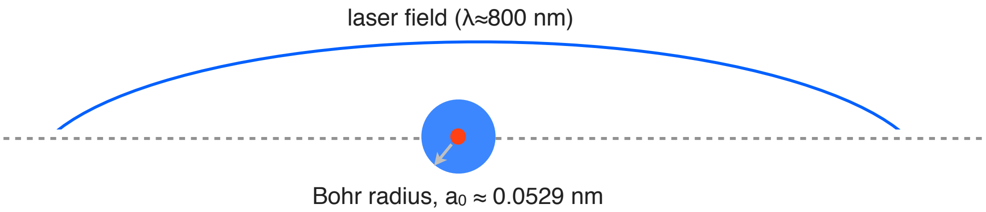

Figure 1.2: Schematic representation of the dipolar approximation. The typical Ti-Sapphire laser wavelength ($\sim$ 800 nm) is much larger than the the atomic dimensions. In this context the laser field can be considered spatially independent in the zone where the interaction occurs. Under these conditions the Eq. (1.1) represents a realistic approximation.

The limit of this approximation is found when the magnetic drift exceeds the spreading of the electron wavefunction. At 800 nm, this limit corresponds, approximately, to laser intensities around the atomic unit (this is studied in detail in [14]). Under these conditions the 3D TDSE can be written as,

$$i\hbar\frac{d}{dt}\psi(\mathbf{r},t) = \left[H_a(\mathbf{r}) + V_{int}(\mathbf{r},t)\right]\psi(\mathbf{r},t) \tag{1.3}$$

In Eq. (1.3), $\psi(\mathbf{r},t)$ is the three-dimensional electronic wavefunction and the Hamiltonian has been splitting in two parts: H_0 is the atomic Hamiltonian,

$$H_a(\mathbf{r}) = \frac{\mathbf{p^2}}{2m} + V(r) \tag{1.4}$$

being for hydrogen atom, $V(r) = -1/\mathbf{r}$. The other term, V_{int} is the part of the Hamiltonian corresponding to the laser-atom interacting with an electron, which in the *length gauge* [15],

$$V_{int}(\mathbf{r},t) = -q\,\mathbf{r}\ \cdot \mathbf{E}(t) \tag{1.5}$$

We will also consider that the laser is linearly polarized along the z-axis, $\mathbf{rE_0} = zE_0 = rE_0cos\theta$, being θ the azimutal angle. Under this assumption the system has a cylindrical symmetry that reduces the dynamics to only two effective dimensions. A suitable form for the numerical integration of the TDSE starts from

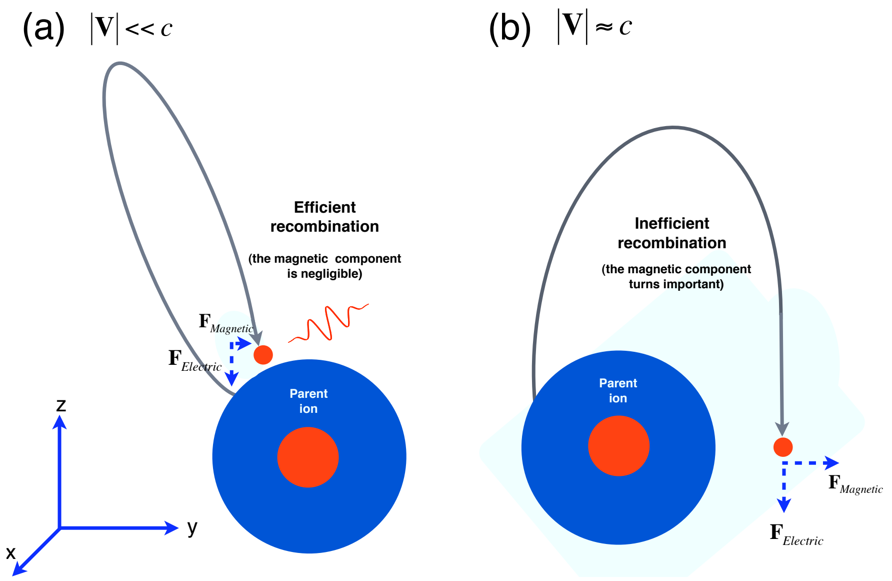
(a) $|\mathbf{V}| << c$
(b) $|\mathbf{V}| \approx c$
Efficient recombination
(the magnetic component is negligible)
$\mathbf{F}_{Magnetic}$
$\mathbf{F}_{Electric}$
Parent ion
z
y
x
Inefficient recombination
(the magnetic component turns important)
Parent ion
$\mathbf{F}_{Magnetic}$
$\mathbf{F}_{Electric}$

Figure 1.3: Effect of the magnetic field of the Lorentz force on the ionized electron and its subsequent recombination with the parent ion. As it is shown in (a), when the electron's velocity is low compared with c, Eq. (1.2) is a reasonable approximation. However, in case that the electron's velocity is closer to c, the magnetic component exerts an important effect on the ionized electron deflecting it from the optimum recombination trajectory as it is shown in (b).

the splitting of the wavefunction in the angular momentum basis,

$$\psi(\mathbf{r},t) = \sum_{\ell=0}^{\infty} \frac{1}{r}\chi_\ell(r,t)Y_\ell^0(\theta) \tag{1.6}$$

We consider that the hydrogen atom is initially in the $1s$ state, consequently only spherical harmonics with $m = 0$ are coupled, since the field is linearly polarized. Substituting the expansion of the wavefunction into the Schrödinger equation, and projecting on spherical harmonics, one gets a system of coupled partial differential equations, one for each value of ℓ [16, 17],

$$\begin{aligned} i\hbar\frac{\partial}{\partial t}\chi_\ell(r,t) = \left[-\frac{1}{2m}\frac{\partial^2}{\partial r^2} - \frac{1}{r} + \frac{\ell(\ell+1)}{2r^2}\right]\chi_\ell(r,t) + \\ rE(t)\left[C_\ell^+\chi_{\ell+1}(r,t) + C_\ell^-\chi_{\ell-1}(r,t)\right] \end{aligned} \tag{1.7}$$

for $\ell > 0$, and for $\ell = 0$

$$i\hbar\frac{\partial}{\partial t}\chi_0(r,t) = \left[-\frac{1}{2m}\frac{\partial^2}{\partial r^2} - \frac{1}{r}\right]\chi_0(r,t) + rE(t)C_0^+\chi_\ell(r,t) \tag{1.8}$$

Were $C_\ell^{\mp}$ coefficients account for the coupling between consecutive spherical harmonics components, and are closely related with the Clebsch-Gordan coefficients,

$$C_{\ell-1}^{+} = C_{\ell}^{-} = \left[\frac{\ell^2}{(2\ell+1)(2\ell-1)}\right]^{1/2} \tag{1.9}$$

To obtain numerical solutions it is necessary to truncate the expansion in spherical harmonics at a maximum value of the angular momentum, ℓ_{max}. Consequently one has to deal with a system of ℓ_{max} partial differential equations (in time t and in radius r). Eqs.(1.7) and (1.8) are propagated in time using a semi-implicit Crank-Nicholson scheme. In order to ensure the numerical convergence, each specific simulation requires different numerical parameters such as the numerical grid size, spacial step and temporal step depending on, in each case, of the laser intensity and/or wavelength and the pulse length. We also use an absorbing mask function at the boundary. The time-dependent population can be computed projecting the wavefunction into the ground state,

$$P(t) = |\langle\psi_0|\psi(\mathbf{r},t)\rangle|^2 \tag{1.10}$$

The single-atom harmonic espectrum is computed using the acceleration form as

$$|a(\omega_0)|^2 = \int_0^T \ddot{d}(t) e^{-i\omega_0 t} dt \tag{1.11}$$

where T is the duration of the laser pulse. $\ddot{d}(t)$ is the acceleration of the dipole moment which can be calculated via Ehrenfest theorem,

$$\ddot{d}(t) = -\frac{d^2}{dt^2}\langle\psi(\mathbf{r},t)|z|\psi(\mathbf{r},t)\rangle = \frac{1}{m}\langle\psi(\mathbf{r},t)|\frac{\partial}{\partial z}\left[V(r)+qV_{int}\right]|\psi(\mathbf{r},t)\rangle \tag{1.12}$$

When a multi-electronic atoms, such as He, are considered, additional approximations are necessary. Those ones will be exposed in section 2.4

1.3.2 The classical Three Step Model

The three-step model is an intuitive approach developed in the early 90's [18, 19, 20] which provides a qualitative description of the HHG process. According to this picture (see Fig. 1.4(a)), in a first step (ionization) the electron tunnels out into the continuum starting with zero kinetic energy. In a second step (acceleration), the electron evolves under the effect of the laser field, gaining kinetic energy. In the third step (recombination), that takes place after the laser field reverses its sign in the next half period, the electron recombines with the parent ion and a harmonic photon is emitted. The energy of the associated photon is the

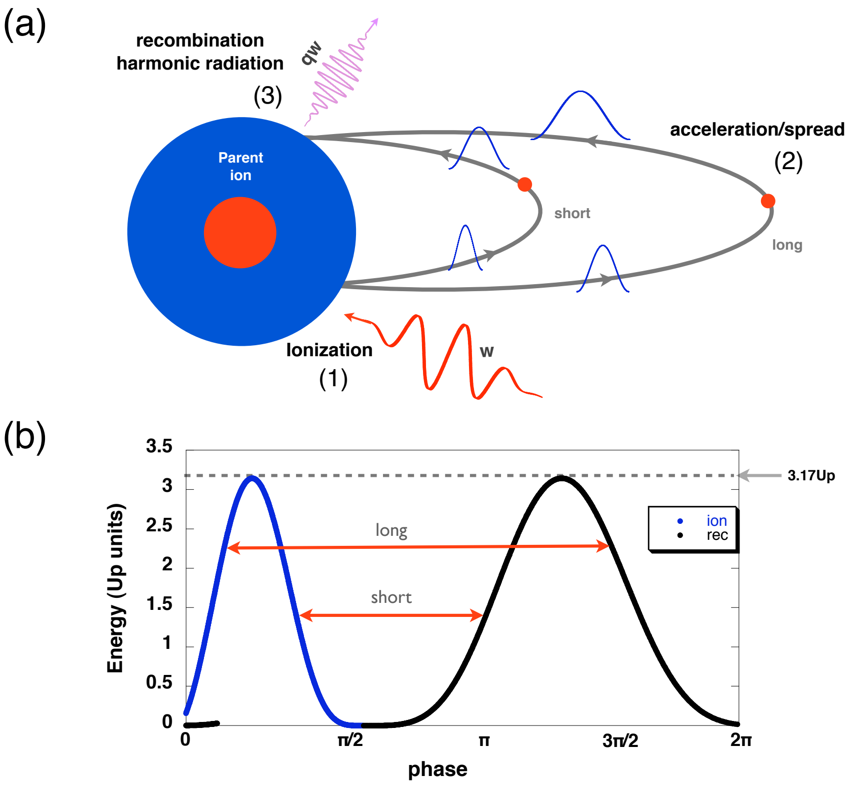
(a)
recombination
harmonic radiation
qw
(3)
acceleration/spreading
(2)
Parent
ion
short
long
Ionization
(1)
w
(b)
3.17Up
ion
rec
long
short
Energy (Up units)
3.5
3
2.5
2
1.5
1
0.5
0
0
π/2
π
3π/2
2π
phase

Figure 1.4: (a) Schematic representation of the classical three step recolision model. (b) Electron kinetic energy (in U_p units) as a function of the phase (ϕ) of the field at the instant of ionization. Blue line and black line represent the ionization and recombination events, respectively.

sum of the ionization potential of the corresponding atom and the kinetic energy accumulated by the electron in the continuum. This model does not consider the quantum effects, such as the spreading of the wavepacket during the excursion in the continuum. However, the predictions of the three-step model (such as the law describing the frequency of the spectral cut-off) are supported by the more elaborated direct solution of the time-dependent Schrödinger equation and for the SFA models for HHG.

According to the three-step model, the maximal photon energy, $E_{cut-off}$, in the harmonic spectrum is given by the cut-off law [18],

$$E_{cut-off} = I_p + 3.17Up \tag{1.13}$$

where I_p is the atomic ionization potential of the corresponding atom and $U_p = q^2E_0^2/4m\omega_0^2$ is the ponderomotive energy. To deduce the cut-off law we shall consider a z-linearly polarized laser field[1],

$$E(t) = E_0 cos(\omega_0 t) \tag{1.14}$$

and consider that the electron is ionized at some particular time, with t_i the initial conditions $z(t_i) = 0$ and $\dot{z}(t_i) = 0$. Solving the Newton-Lorentz equation of motion for the free electron we obtain,

$$z(\phi) = \frac{qE_0}{m\omega_0^2}\left[cos\phi - cos\phi_i + (\phi - \phi_i)sin\phi_i\right] \tag{1.15}$$

where we have denoted $\phi \equiv \omega_0 t$. We also compute the kinetic energy,

$$E_{kin}(\phi) = 2U_p(sin\phi - sin\phi_i)^2 \tag{1.16}$$

The phase of the field at the moment of recombination, ϕ_r, can be obtained as the roots of the equations $z(\phi_r) = 0$. Therefore, the energy of the emitted photon upon recombination is given by $E_{kin}(\phi) + I_p$. In Fig. 1.4(b) we plot the kinetic energy (in U_p units) as a function of the phase of the field at ionization ϕ_i and recombination ϕ_r for approximately $0 < \phi_i < \pi$. The recombination occurs only if $0 < \phi_i < \pi/2$ and the electron never returns to the atomic core if $\pi/2 < \phi_i < \pi$. $E_{kin}(\phi)$ takes the maximum value $3.17U_p$ at $\phi_i = 0.094\pi$ and $\phi_r = 1.416\pi$. These trajectories are the responsible to the emission of the highest frequency harmonics, given by the cut-off law Eq. (1.13). In fact, at the instant of ionization of these trajectories, the laser field is close to its maximum, consequently, the tunneling ionization probability is high. For this reason harmonic generation is quite efficient near the cut-off.

---

[1] In order to simplify the mathematical approach we have consider a monochromatic field (without envelope). However this assumption is not relevant for the final result

For a particular value of E_{kin}, we can find ϕ_i and ϕ_r as solutions of the following coupled equations:

$$\big(cos\phi - cos\phi_i + (\phi - \phi_i) sin\phi_i\big) = 0 \tag{1.17}$$

$$\big(sin\phi_r - sin\phi_i\big)^2 = \frac{E_{kin}}{2U_p} \tag{1.18}$$

Note that, for rescatterings with energies below $3.17Up$ there are always two trajectories every half cycle with the same kinetic returning energy. One of them for $0.094\pi < \phi_i < \pi/2$, $\pi/2 < \phi_r < 1.416\pi$ is known in the literature as *short trajectory*, and the other, $0 < \phi_i < 0.094\pi$, $1.416\pi < \phi_r < 2\pi$ known as *long trajectory*.

1.3.3 Strong Field Approximation for HHG: Lewenstein model

As described above, the three step model is entirely classical. Lewenstein and co-workers developed the first quantum mechanical model for HHG based on the Strong Field Approximation (SFA) which is reported in a seminal paper [21] published in the early nineties. From the quantum view point, the trajectory description is replaced by a wavefunction, initially bound in an atom or molecule, which is drastically deformed by a strong laser field. Part of the wavefunction is pulled away from the binding potential through the classically forbidden barrier and eventually interferes with the part left in the bound state.

Lewenstein's approach is based on the standard SFA assumptions,

(i) The contribution of the excited bound levels can be neglected.

(ii) The effect of the atomic potential on the motion of the continuum electron can be neglected. (i.e. in the continuum, the electron can be treated as a free particle moving in the electric field.)

Assuming these approximations, the time dependent dipole moment defined as $x(t) = \langle\psi(\mathbf{r},t)|z|\psi(\mathbf{r},t)\rangle$ can be found to be,

$$x(t) = i\int_{-\infty}^{t} dt' \int d^3\mathbf{p}d^*(\mathbf{p}+q\mathbf{A}(t)/c)e^{-iS(\mathbf{p},t,t')/\hbar}E(t')d(\mathbf{p}+q\mathbf{A}(t')/c) + c.c., \tag{1.19}$$

being $\mathbf{p}+q\mathbf{A}(t)/c$ the kinetic momentum and $d(\mathbf{p})$ the dipole transition matrix element, $\mathbf{A}(t) = -c\int \mathbf{E}(t)dt$ the vector potential and $S(\mathbf{p},t,t')$ the semiclassical action,

$$S(\mathbf{p},t,t') = \int_{t'}^{t} dt'' \left(\frac{[\mathbf{p}+q\mathbf{A}(t'')/c]^2}{2m} + I_p \right) \tag{1.20}$$

The physical interpretation of Eq. (1.19) can be addressed in consistence with the three step model. The term $E(t')d(\mathbf{p}+q\mathbf{A}(t')/c)$ represents the ionization at time t', the term $e^{-iS(\mathbf{p},t,t')}$ corresponds to the evolution from t' to t and $d^*(\mathbf{p}+q\mathbf{A}(t)/c)$ describes the recombination at time t. Here is assumed that in the time interval from t' to t the electron evolves as a free particle without the effect of the atomic potential. The Fourier transform of Eq. (1.19) can be written as,

$$\begin{aligned}\hat{x}(\omega_h) = i\int_{-\infty}^{\infty} dt \int_{-\infty}^{t} dt' \int d^3\mathbf{p}d^*(\mathbf{p}+q\mathbf{A}(t)/c)e^{[i\omega_h t - iS(\mathbf{p},t,t')]/\hbar} \\ E(t')d(\mathbf{p}+q\mathbf{A}(t')/c) + c.c.,\end{aligned} \tag{1.21}$$

Eq. (1.21) encloses nested integrals that make the computation extremely heavy. For this reason, the standard procedure is to resort to a saddle-point approximation. The stationary conditions can be found equalling the first derivatives of the exponent $[\omega_h t - iS(\mathbf{p},t,t')]/\hbar$ with respect to $\mathbf{p}$, t and t' to zero, leading to the following equations,

$$p(t-t') + \frac{q}{c}\int_{t'}^{t} A(t'')dt'' = 0 \tag{1.22}$$

$$\frac{[p+qA(t')/c]^2}{2m} = -I_p \tag{1.23}$$

$$\frac{[p+qA(t)/c]^2}{2m} = \omega_h - I_p \tag{1.24}$$

Eq. (1.23) can be written as $\int_{t'}^{t}(p+qA(t'')/c) = 0$ which indicates that the electron appears in the continuum and recombines later at the same position. Eq. (1.24) rewritten toghether with Eq. (1.24) as $(p+qA(t)/c)^2/2m-(p+qA(t')/c)^2/2m = \omega_h$ represents the energy conservation in the harmonic radiation process. The interpretation of Eq. (1.23) is not easy due to its negative right-hand side, which implies that the solutions of the saddle-point equations are complex. The complex time t' is usually interpreted in terms of a tunneling time [21]. Note that replacing in these equations I_p by zero and $\omega_h - I_p$ by E_{kin} we recover Eq. (1.17) and Eq. (1.18) for the classical three step model. As is reported in [21] the Lewenstein model predicts a cut-off energy slightly higher that the three step model,

$$E_{cut-off} = 3.17U_p + gI_p \tag{1.25}$$

with $g \sim 1.3$. This can be justified by the fact that there is a finite distance between the nucleus and the tunnel exit. The electron which has returned to the position of the tunnel exit is further accelerated till it reaches the nuclear position.

We shall see in the following chapters that the saddle point can be avoided while retaining the efficiency of the calculation. Our method for this is developed in the frame of the our SFA+ approach, but can be equally applied to the standard SFA equations.

1.4 Attosecond pulses

According to the Fourier analysis, the temporal duration τ, for a given laser pulse reciprocally depends on its spectral bandwidth $\Delta\omega_0$ in the frequency domain. Consequently the shortest possible pulse to achieve, for a given spectrum, is limited by the so called *transform-limited pulse duration*,

$$\tau \geq \frac{2\pi c_B}{\Delta\omega_0} \tag{1.26}$$

where c_B is a constant factor which, depending on the pulse envelope, it takes different values. In the case of *Gaussian* envelopes c_B=0.441 and for the *Hyperbolic secant* c_B=0.315. From the Eq. (1.26) is followed that to produce ultrashort pulses a very broad spectral bandwidth is required. On this manner the HHG process constitutes the optimal candidate to provide a direct route to synthesize attosecond (1 attosecond=10^{-18}s) pulses. In the early nineties, Farkas and Tóth, in a pioneering theoretical work, suggest the possibility to synthesize pulses of near attosecond duration based on the multiple harmonic generation in gases [3]. In this paper the authors conclude:

> *"... the described idea and technique seems to be realizable in all non-linear processes, where high harmonic generation takes place, e.g., in the case of collinear harmonic generation on metal surfaces - in which case both odd and even harmonics appear - observed by us recently, in the case of multiphoton light scattering by free electrons, etc. "*.

If odd harmonics are emitted, and they are locked in phase, the corresponding temporal profile would consist of a train of pulses separated by half the laser period and of duration in the attosecond range, or in other words, the coherent sum of a set of harmonics from the plateau would result on a train of attosecond pulses from the Fourier synthesis of the harmonic spectra. However, the high harmonics were, in general, not in phase, due to the interference of various energetically allowed electronic trajectories leading to the harmonic emission. The characteristics of the attosecond pulses (central wavelength, width and dispersion) depend on the particular relation of the spectral phase and amplitudes between successive high harmonics. The emission of each specific harmonic is associated with its corresponding long and short trajectories. The emission time $t_e = \frac{\partial \phi}{\partial \omega}$, where ϕ is the harmonic phase, accounts the synchronization of the harmonics in the emission process. According to the three step model, t_e varies almost linearly with the harmonic order (with a positive slope for the short trajectory and negative slope for the long). It has confirmed experimentally, see for instance [25, 26]. Close to the cut-off, the emission time associate with long and short trajectories overlaps in one unique trace with a plane slope [25].

Nowadays trains of attosecond pulses are routinely produced [22, 23, 24, 25, 27]. In principle, the schemes based on HHG require filtering of the phase locked harmonics out of the entire spectrum; in particular from the low harmonics to the fall-off region of the spectrum. However, at the end of chapter 3 we will present a different technique to achieve a single attosecond pulse based on the fast and total depopulation of the atom by using a particular driving laser pulses.

2

SFA+ formalism

> *“ Contraria non contradictoria sed complementa sunt ”*
>
> *Niels Henrik David Bohr*

2.1 Derivation of SFA+: P and Q projections

As has been stressed above, the strong field interaction with atoms must be treated within non-perturbative context. Here we will study the theoretical modelization of strong field high-order harmonic generation. For this goal we have extended the standard SFA approach avoiding the semiclassical approximations to preserve the complete quantum description of the single-atom response and including the effect of the external field on the dynamic of the ground state of the target atom. In the following, we shall refer to our extension of the SFA as SFA+.

Our results show that SFA+ improves the quantitative accuracy of the SFA HHG spectra when compared with the exact results of the ab-initio computation of the 3D TDSE. Also, our study reports that SFA+ is found to describe corrrectly the dependence of the harmonic yield with the laser wavelength.

In this section we will derive the SFA+ approach for HHG from the S-matrix formalism. The interaction of a single atom with an intense electromagnetic field assuming the approximations exposed in the previous chapter is described by the temporal evolution of the electron wavefunction according to the Schrödinger equation,

$$i\hbar\frac{\partial}{\partial t}|\psi(t)\rangle = \left[H_a + V_i(t)\right]|\psi(t)\rangle \tag{2.1}$$

being $H_a = \frac{p^2}{2m} - V_c(r)$ the atomic Hamiltonian ($V_c(r)$ represents the electron potential energy in the atom) and $V_i(t) = -(q/mc)A(t)p_z + q^2/(2mc^2)A^2(t)$ represents the interaction term in the velocity gauge.

In terms of the Green's propagators the electron evolution is given by,

$$G^+(t,t_0) = G_a^+(t,t_0) + \frac{1}{\hbar}\int_{t_0}^{t} G^+(t,t_1)V_i(t_1)G_a^+(t_1,t_0)dt_1 \tag{2.2}$$

where G_a^+ is the propagator of the atomic electron in the field free case. The wavefunction at any given time t may be found as $\psi(t) = iG^+(t,t_0)\psi(t_0)$. Consequently the exact integral solution of Eq. (2.1) is given by

$$-i|\psi(t)\rangle = G_a^+(t,t_0)|\psi(t_0)\rangle + \frac{1}{\hbar}\int_{t_0}^{t} dt_1 G^+(t,t_1)V_i(t_1)G_a^+(t_1,t_0)|\psi(t_0)\rangle \tag{2.3}$$

If we consider a splitting of the Hilbert space into bound (Q) and continuum subspaces (see Fig. 2.1).

We can define $\hat{Q}$ and $\hat{P}$ as the corresponding projectors. These operators, by definition, satisfy the following mathematical identities: $\hat{Q}+\hat{P}=1$, $\hat{Q}\hat{P}=\hat{P}\hat{Q}=0$, $\hat{Q}^2=\hat{Q}$ and $\hat{P}^2=\hat{P}$, also $|\psi(t_0)\rangle = \hat{Q}|\psi(t_0)\rangle$, since $|\psi(t_0)\rangle$ represents an initial bound state and according to these definitions, Eq. (2.3) results in two coupled equations which represents the bound part of the wavefunction,

$$\begin{aligned}
-i\hat{Q}|\psi(t)\rangle &= G_a^+(t,t_0)\hat{Q}|\psi(t_0)\rangle \\
&+ \frac{1}{\hbar}\int_{t_0}^{t} dt_1\hat{Q}G^+(t,t_1)(\hat{P}+\hat{Q})V_i(t_1)(\hat{P}+\hat{Q})\ G_a^+(t_1,t_0)|\psi(t_0)\rangle \\
&= G_a^+(t,t_0)|\psi(t_0)\rangle \\
&+ \frac{1}{\hbar}\int_{t_0}^{t} dt_1\hat{Q}G^+(t,t_1)\hat{Q}V_i(t_1)\hat{Q}\ G_a^+(t_1,t_0)|\psi(t_0)\rangle
\end{aligned} \tag{2.4}$$

and the continuum part

$$-i\hat{P}|\psi(t)\rangle = \frac{1}{\hbar}\int_{t_0}^{t} dt_1\hat{P}G^+(t,t_1)\hat{P}V_i(t_1)\hat{Q}\ G_a^+(t_1,t_0)|\psi(t_0)\rangle \tag{2.5}$$

The second term in the *rhs* of Eq. (2.4) describes the non-ionizing excitation of the ground-state at t_1 and its subsequent evolution until t in the combined influence

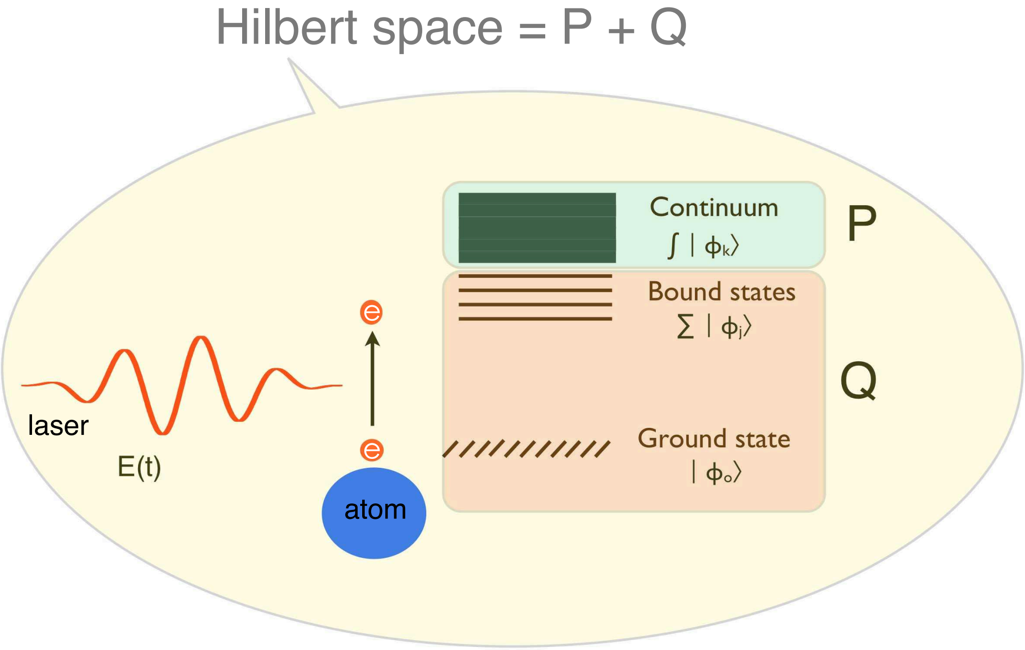

Figure 2.1: Laser-atom interaction picture treated under P and Q formalism

of the atom and the field. Therefore Eq. (2.4) describes the evolution of the bound part of the wavefunction as the superposition of the bare (field free) evolution and the bound-state excitations (field-dressing). The standard SFA consists of setting $\hat{Q}V_i(t_1)\hat{Q} = 0$ in Eq. (2.4), considering that the field interaction leads invariably to ionization, together with the condition $\left[H, \hat{P}\right] = 0$, which prevents the recombination of an ionized state. Thus, in considering $\hat{Q}V_i(t_1)\hat{Q} \neq 0$ in Eq. (2.4), we soften the constraints of standard SFA. We shall, therefore, refer to this approach as SFA+.

On this manner, as we exposed in the precedent chapter, the single-atom radiation is proportional to the Fourier transform of the mean dipole acceleration, $a(t) = \langle\psi(t)|\hat{a}|\psi(t)\rangle$, that can be calculated according to the Ehrenfest theorem, $\hat{a} = -(q/m)\partial V_c/\partial z$ (V_c represents the electrons potential energy). The higher-frequency harmonics correspond to the most energetic photons, thus involving the most energetic transitions, i.e. free to bound. Therefore, for HHG it is reasonable to approximate

$$a(t) \simeq \langle\psi(t)|\hat{Q}\hat{a}\hat{P}|\psi(t)\rangle + c.c. \tag{2.6}$$

where a_b and a_d are two interfering contributions to the total acceleration, associated with transitions between the continuum to the bare ground state or to its field-dressing (this later effect is not considered in the standard SFA). From Eqs.(2.4),(2.5) and after some algebra (see Appendix A[1]) we obtain,

$$a(t) = a_b(t) + a_d(t) + c.c. \tag{2.7}$$

being

$$\begin{aligned} a_b(t) &= \frac{1}{\hbar}\int_{t_0}^{t} dt_1 \langle\phi_0|G_a^-(t_0,t)\hat{a}\hat{P}G^+(t,t_1)\hat{P}V_i(t_1)\hat{Q}G_a^+(t_1,t_0)|\phi_0\rangle & (2.8)\\ a_d(t) &= \frac{1}{\hbar^2}\int_{t_0}^{t} dt_2 \langle\phi_0|G_a^-(t_0,t_2)\hat{Q}V_i(t_2)\hat{Q}G^-(t_2,t)\hat{Q}\hat{a} \\ &\quad \int_{t_0}^{t_2} dt_1 \hat{P}G^+(t,t_1)\hat{P}V_i(t_1)\hat{Q}G_a^+(t_1,t_0)|\phi_0\rangle & (2.9) \end{aligned}$$

where we have taken the initial bound state as the atomic ground state, $|\psi(t)\rangle \equiv |\phi_0\rangle$ and introduced a time-ordering $t_2 > t_1$.

Now, we will describe the operators $\hat{P}V_i(t_1)\hat{Q}$, $\hat{P}G^+(t,t_1)\hat{P}$, $\hat{Q}V_i(t_2)\hat{Q}$ and $\hat{Q}G^-(t,t_2)\hat{Q}$. The operators $\hat{P}V_i(t_1)\hat{Q}$ and $\hat{P}G^+(t,t_1)\hat{P}$ in Eqs. (2.5), (2.8) and (2.9) can be evaluated according to the standard procedure in SFA: First we consider a planewave basis, $\{\mathbf{k}\}$, for the subspace defined by $\hat{P}$, therefore

$$\hat{P} \simeq \int d\mathbf{k}|\mathbf{k}\rangle\langle\mathbf{k}| \tag{2.10}$$

Each planewave evolves as a Volkov wave of momentum $\mathbf{p} = \hbar\mathbf{k}$ under the influence of the electromagnetic field. Therefore,

$$\hat{P}V_i(t_1)\hat{Q} \simeq \int d\mathbf{k}V_i(\mathbf{k},t_1)|\mathbf{k}\rangle\langle\mathbf{k}|\frac{C_F}{r^n} \tag{2.11}$$

---

[1] In the final part of this thesis have been included several Appendices were you can find, in detail, all algebraic approaches which have been omitted in the main text. All of them have been denoted along the text by "Appendix ..."and the corresponding letter. In the electronic version, by "double-clicking" over each one, you will be redirected to the Appendix required.

with $V_i(\mathbf{k}, t_1) = -(q/mc)A(t_1)k_z + q^2/(2mc^2)A^2(t_1)$. Note also that we have included in Eq. (2.11) the Coulomb factor introduced by the first time by Krainov [30] in the literature, whose general form is $C_F/r^n = (2Z^2/n^2E_0r)^n$ (for hydrogen atom $n = 1$ and $Z = 1$).
In addition we have

$$\hat{P}G^+(t, t_1)\hat{P} = -i\exp\left[-(i/\hbar)\int_{t_1}^{t} d\tau\hat{P}H(\tau)\hat{P}\right] \tag{2.12}$$

with

$$\hat{P}H(\tau)\hat{P} \simeq \int d\mathbf{k}\ \epsilon(\mathbf{k}, \tau)|\mathbf{k}\rangle\langle\mathbf{k}| \tag{2.13}$$

being $\epsilon(\mathbf{k}, \tau) = \hbar^2k^2/2m-(q/mc)A(\tau)k_z+q^2/(2mc^2)A^2(\tau)$. With this definitions and some algebra (see Appendix B) the bare state contribution to the acceleration, Eq. (2.8), can be written as $a_b(t) = \int d\mathbf{k}a_b(\mathbf{k}, t)$ where

$$a_b(\mathbf{k}, t) = -\frac{i}{\hbar}C_F\int_{t_0}^{t} dt_1 e^{i\epsilon_0(t-t_1)/\hbar}e^{-i\frac{1}{\hbar}\int_{t_1}^{t}\epsilon(\mathbf{k},\tau)d\tau}\langle\phi_0|\hat{a}|\mathbf{k}\rangle V_i(\mathbf{k}, t_1)\langle\mathbf{k}|r^{-n}|\phi_0\rangle \tag{2.14}$$

Note that in the general case, the evaluation of the operators of the field-dressing part, Eq. (2.9), is not trivial. However, for the particular case of the study of harmonic generation some simplifications/approximations can be assumed. As it is well known high-order harmonics are generated through transitions from continuum to bound states that take place during the process of rescattering of the previously ionized electron with the parent ion. Instead of assuming this process as instantaneous, let us consider that the harmonic generation at time t is triggered by the collision of the ionized electron taking place over the small time interval, $t - \delta t_s$ to t. Assuming the bound state wavefunction to be the ground state at the beginning of this interval, Eq. (2.4) predicts its evolution during the temporal lapse of rescattering, by setting the lower limit t_0 of the time integral to the initial time $t - \delta t_s$,

$$\begin{aligned} -i\hat{Q}|\psi(t)\rangle \;&\simeq\; G_a^+(t, t_0)|\phi_0\rangle \\ &+\; \frac{1}{\hbar}\int_{t-\delta t_s}^{t} dt_1\hat{Q}G^+(t, t_1)\hat{Q}V_i(t_1)\hat{Q}\ G_a^+(t_1, t_0))|\phi_0\rangle \end{aligned} \tag{2.15}$$

and

$$\begin{aligned} a_d(t) &\simeq \frac{1}{\hbar^2}\int_{t-\delta t_s}^{t} dt_2 \langle\phi_0|G_a^-(t_0,t_2)\hat{Q}V_i(t_2)\hat{Q}G^-(t_2,t)\hat{Q}\hat{a} \\ &\int_{t_0}^{t_2} dt_1 \hat{P}G^+(t,t_1)\hat{P}V_i(t_1)\hat{Q}G_a^+(t_1,t_0)|\phi_0\rangle \end{aligned} \tag{2.16}$$

The dynamics of the bound excitations during the time lapse δt_s is given by the operator $\hat{Q}G^-(t_2,t)\hat{Q}$ which is a function of the total Hamiltonian $H(t) = H_a + V_i(t)$. The rescattering event is defined by the overlap of the of the free electron wavepacket with the coordinate origin, where the potential singularity is located. With this definition, for the most energetic electrons, the scattering time lapse can be evaluated as

$$\delta t_s \simeq (3\pi/2\omega_0)\sqrt{|\epsilon_0|/3.17U_p} \tag{2.17}$$

being U_p the ponderomotive energy (see Appendix C for more details). For large U_p, this time lapse is small enough to approximate the time dependent operator $V_i(t)$ in Eqs. (2.15) and (2.16) by its time average over δt_s (see Appendix D)

$$\Delta_s = \langle V_i(t)\rangle = (1/\delta t_s)\int_{t-\delta t_s}^{t}\left[-(q\hbar/mc)A(\tau)k_z + (q^2/2mc^2)A^2(\tau)\right]d\tau \tag{2.18}$$

where $\hbar k_z$ is a particular momentum of the state, than can be evaluated as (see Appendix E)

$$k_z = -\frac{2}{\hbar}\sqrt{mU_p}\frac{\sin\omega_0\delta t_s}{\omega_0\delta t_s}\left[1-\sqrt{1-\frac{1}{6}\left(1+\frac{\epsilon_0}{U_p}+\frac{\sin 2\omega_0\delta t_s}{2\omega_0\delta t_s}\right)\left(\frac{\sin\omega_0\delta t_s}{\omega_0\delta t_s}\right)^{-2}}\right] \tag{2.19}$$

Using Eq. (2.18) and Eq. (2.19) the total Hamiltonian during the recollision can be approximated as $H = H_a + V_i \simeq |\epsilon_0 + \Delta_s|$ being ϵ_0 the energy of the bound state. Therefore $\hat{Q}G^-(t_2,t)\hat{Q}$ can be approximated by $i\exp[i(\epsilon_0+\Delta_s)(t-t_2)]$. On the other hand, we should also look for a simplified form of the interaction operator $\hat{Q}V_i(t_2)\hat{Q}$. A first choice would be to replace it by its time-averaged form Δ_s, but it proves not to be a sufficiently accurate approximation. We shall, therefore consider the factorization $V_i(t) = H(t) - H_a \simeq p^2/2m + \Delta_s - H_a$. Note that in this factorization, the Coulomb term in $H(t)$ is neglected as we assume the ground-state excitations to have minimal probability near the origin. With these approximations, and after some algebra the dressing contribution to the acceleration can be written in terms of the bare contribution as (see Appendix F)

$$a_d(\mathbf{k},t) \simeq -\left[1+\frac{k^2/2m-\epsilon_0}{\Delta_s}\right] a_b(\mathbf{k},t) \tag{2.20}$$

Therefore the total acceleration is given by

$$a(t) = -\int d\mathbf{k}\frac{\hbar^2 k^2/2m-\epsilon_0}{\Delta_s} a_b(\mathbf{k},t) + c.c. \tag{2.21}$$

Note that the opposite sign of a_d relative to a_b, see Eq. (2.20), leads to an interference between the bare and dressing contributions to the acceleration. This is a main result of the SFA+ approach, as the standard SFA considers only the bare contribution, a_b. The strength of the interference changes with the laser parameters and affects the harmonic yield. In particular, SFA+ gives a proper account of the scaling of the harmonic intensities with the laser wavelength [31]. This will be studied in detail later, in 2.3.1 and 2.3.2.

As a final step, the time integral leading to $a_b(\mathbf{k})$ can be computed numerically very effectively without resort to the saddle-point approximation and, thus, retaining the full quantum description of the process. This is done by integrating the set of (uncoupled) one dimensional ordinary differential equations, each associated with a particular Volkov wave $\mathbf{k}$, that results from differentiating Eq. (2.14)

$$\frac{d}{dt}a_b(\mathbf{k},t) = \frac{i}{\hbar}\left[\epsilon_0-\epsilon(\mathbf{k},t)\right] a_b(\mathbf{k},t) - \frac{i}{\hbar}C_F\langle\phi_0|\hat{a}|\mathbf{k}\rangle V_i(\mathbf{k},t)\langle\mathbf{k}|r^{-n}|\phi_0\rangle \tag{2.22}$$

Note also that this equation is also highly parallelizable, if even shorter computing times are needed, for instance, in the case of the study of the macroscopic response where fast single-atom computations are required.

In summary, in this part we have developed the SFA+ based on the S-Matrix formalism operators that goes beyond the standard SFA. As we will show later, SFA+ provides good quantitative agreement compared with the exact integration of the 3D TDSE, reproducing correctly the harmonic efficiency of the higher frequency part of the HHG spectra, providing a compact formulation in a reasonable time of computation. We also point out that although the recurrence to the concept of field dressing of states to overcome the limitations of the standard SFA is not new [32, 33, 34]. This is usually introduced for the description of the electron ionization. Also, they cosider the dressing over all times, leading to Stark shifts of the ground level, while here we introduce the concept of field dressing during the short time interval where the rescattring occurs.

2.2 Test of SFA+ versus SFA and 3D TDSE

Next we will compare several results provided by the SFA+ approach against the results of the standard SFA and the exact integration of the 3D TDSE . We point out that there are different versions of the standard SFA, and probably all of them report similar results but not exactly the same [35, 36, 37]. A complete comparison would demand to test our results (SFA+) with all of them, but this goal would require to implement, in detail, one by one, constituting an important effort that falls out of the scope of this thesis. Consequently, here we have chosen to compare SFA+ results with the SFA form without resorting to the saddle point approximation, avoiding the possible effects that this approximation may cause. In order to avoid ambiguities, in the following, the *SFA* accounts the SFA without the saddle point approximation.

2.2.1 SFA+ harmonic espectra versus SFA and 3D TDSE

Before showing the comparisons between the different HHG spectra we shall discuss the forms of the driving laser pulses used in our simulations. These are described analytically by the Eq. (1.1) where $f(t)$ represents the pulse envelope. Along this thesis we will use two kind of envelopes. On the other hand we will consider sin^2-envelopes defined by $f(t) = sin^2(\omega_0 t/2N)$, being ω_0 the laser frequency and N the total number of cycles. Although *gaussian* envelopes may be considered a most realistic description of the laser pulse. They present an asymptotic behaviour in the respective tails forcing to extended integration times, increasing considerably the time of computation. However according to our tests, the numerical HHG spectra obtained from sin^2-envelopes does not differ substantially from *gaussian* pulses. The second envelope form is *trapezoidal* with turn-on, flat-top and turn-off times. Trapezoidal pulses are useful to describe the HHG from long pulses, that have almost a constant envelope, using relatively small integration time grid.

Having this in mind, we will now compare the harmonic spectra computed using

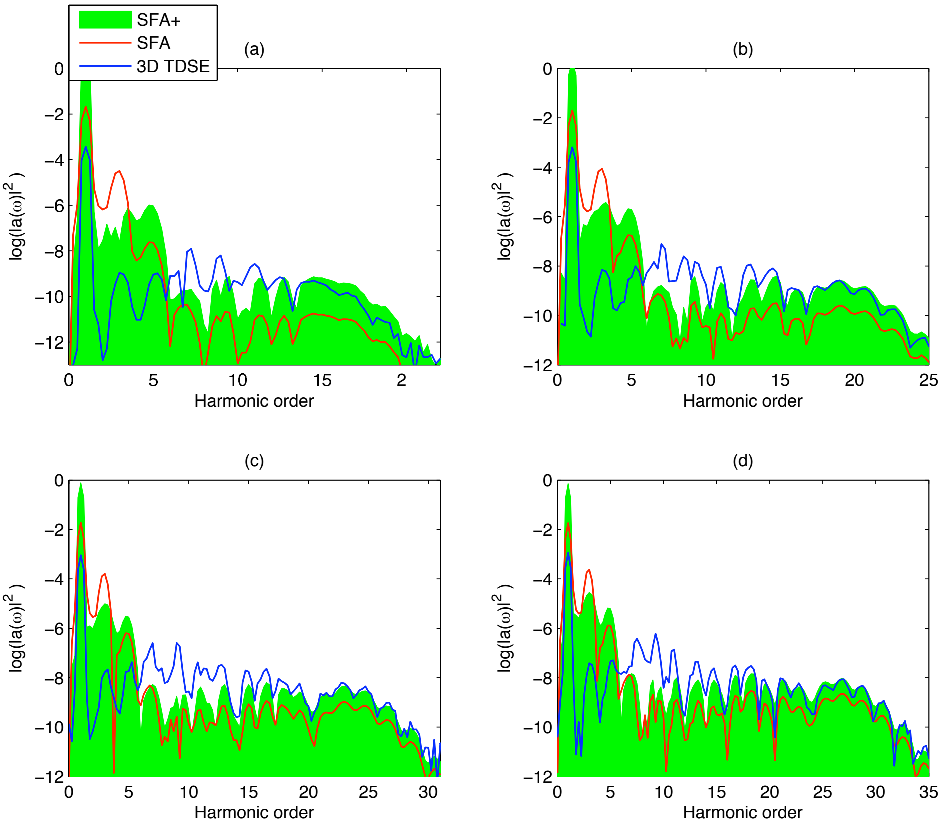

Figure 2.2: HHG spectra in hydrogen atom computed with SFA+ (green), SFA (red) and 3D TDSE (blue), (this color criteria will be used in the folowing) for four different laser intensities, (a) $5.06 \times 10^{13} W/cm^2$, (b) $8.77 \times 10^{13} W/cm^2$, (c) $1.26 \times 10^{14} W/cm^2$ and (d) $1.57 \times 10^{14} W/cm^2$. All of them are computed at $800 nm$. Note that panels (a) and (b) represent the two cases in multiphoton regime ($\Gamma_K = 1.5$ and $\Gamma_K = 1.14$ respectively) and cases (c) $\Gamma_K = 0.95$ and (d) $\Gamma_K = 0.85$, belong to the tunnel regime. We have used 4-cycle sin^2 pulse envelope.

SFA+ with the exact 3D TDSE and with the predictions of SFA. Let us start testing our SFA+ model in the two different regimes of ionization: multiphoton and tunneling.. According to the Keldysh criteria [38], $\Gamma_K = \sqrt{I_P/2U_P}$, there are two ways to transit from the multiphoton to the tunnel ionization regime: either increasing the laser intensity and/or increasing the laser wavelength. Fig. 2.2 shows

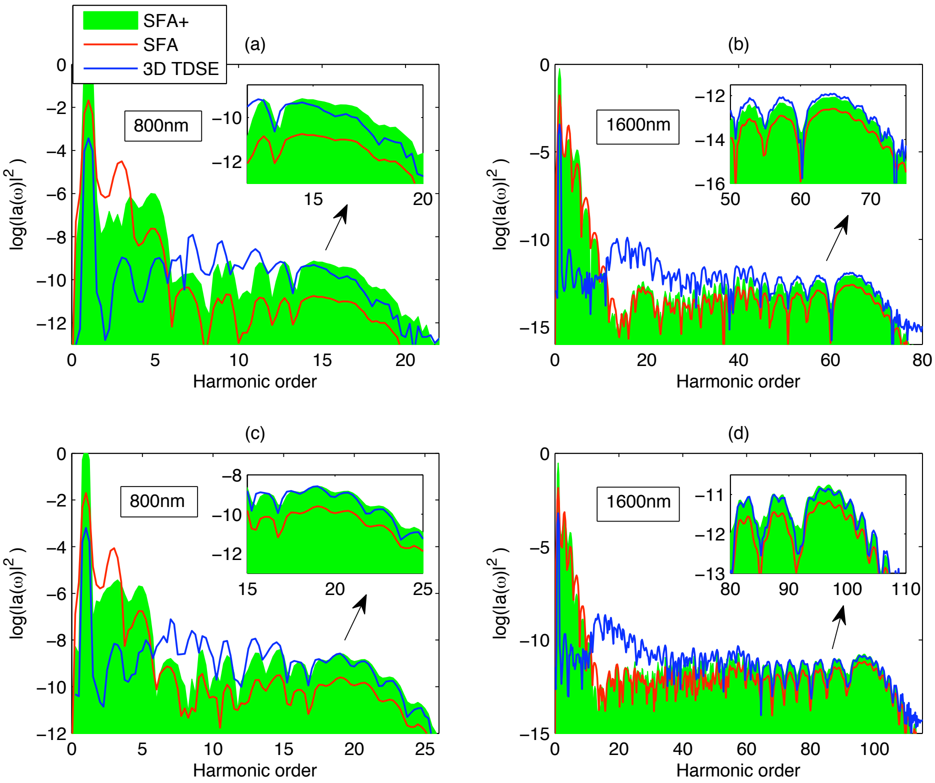

Figure 2.3: HHG spectra in hydrogen for two different laser intensities and two different laser wavelengths. Panels (a) and (b) represent the espectra computed both at the same intensity, $5.06 \times 10^{13} W/cm^2$. Panels (c) and (d) are computed both at $8.77 \times 10^{13} W/cm^2$. Panels (a) and (c) are computed at 800nm and panels (b) and (d) correspond to 1600nm. In (a) $\Gamma_K = 1.5$, in (b) and $\Gamma_K = 0.75$, in (c) $\Gamma_K = 0.95$ and in (d) $\Gamma_K = 0.57$. We have used 4-cycle sin^2 pulse envelope.

the transition from multiphoton to tunnel by increasing the laser peak intensity (see the caption of the figures for more details). Panels (a) and (b) correspond to multiphoton cases and panels (c) and (d) to tunnel cases. By a simple inspection it is possible to conclude that SFA+ reproduces with a noticiable degree of accuracy the higher frequency part of the harmonic plateau in the multiphoton regime (panels (a) and (b)) where the SFA presents a stronger discordance with the 3D TDSE. Note however that in tunnel regime (panels (c) and (d)) the agreement with the 3D TDSE is excellent in the high part of the plateau. However

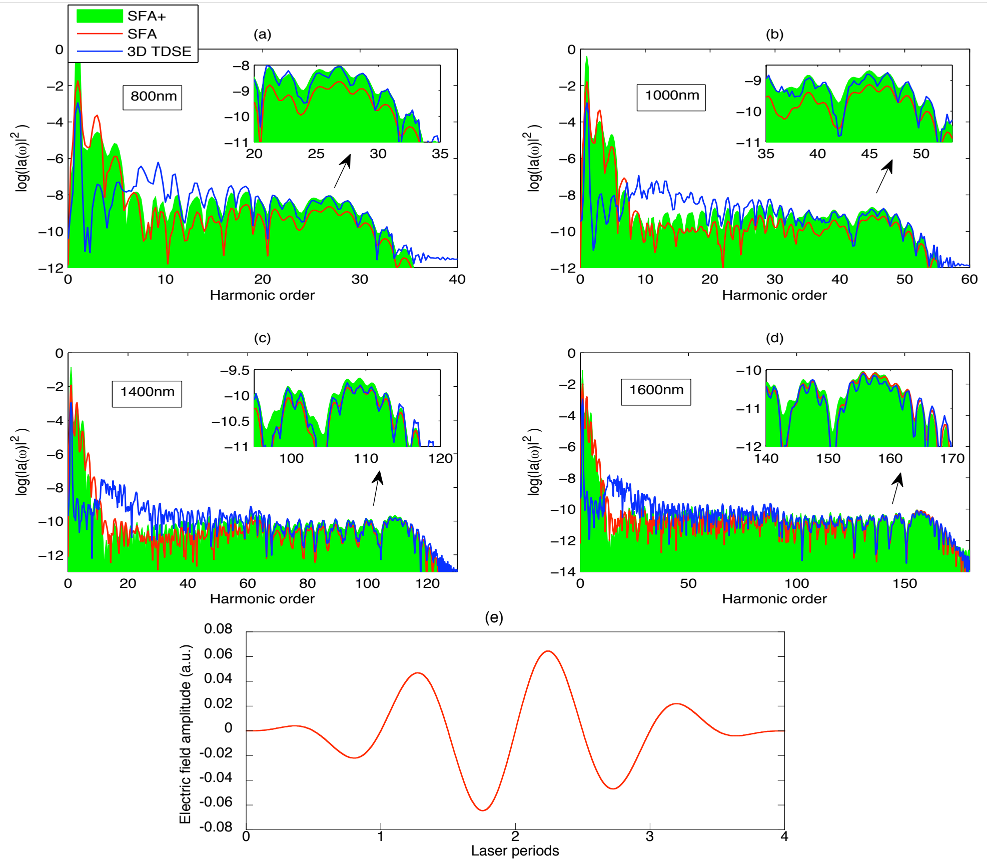

Figure 2.4: HHG spectra in hydrogen at four different laser wavelengts, (a) $800nm$, (b) $1000nm$, (c) $1400nm$ and (d) $1600nm$. All cases are computed at the same laser intensity $I = 1.57 \times 10^{14} W/cm^2$. Here, in (a) $\Gamma_K = 0.85$, in (b) $\Gamma_K = 0.68$, in (c) $\Gamma_K = 0.48$ and in (d) $\Gamma_K = 0.42$. The respective insets represent a zoom of the cut-off zone. We have used 4-cycle sin^2 envelope plotted in panel (e).

is not surprising that the SFA and SFA+ fails to reproduce quantitatively the lower order harmonics. In other words, considering the plateau located in the lower part of the spectra which corresponds to the first excited state of hydrogen

($I_p = 0.125 a.u.$). The corresponding cut-off appears around $0.375 a.u.$ from the cut-off of the ground state. For $\lambda = 800nm$ it corresponds approximately to $7th$ harmonic (see Fig. 2.2). Consequently, the degree of discordance with respect to the 3D TDSE depends on the degree of excitation of the excited state. Note that when the intensity is increased the tunnel barrier decreases, and the tunnel ionization grows exponentially. For this reason, for instance, in panel (c) of Fig. 2.2 the accuracy with the 3D TDSE for the lower harmonics is better than in panel (b). The same effect occurs when the wavelength is increased up to $1600nm$ due to the degree of excitation is lower. Under this situation a double number of photons is required to achieve the atomic resonance.

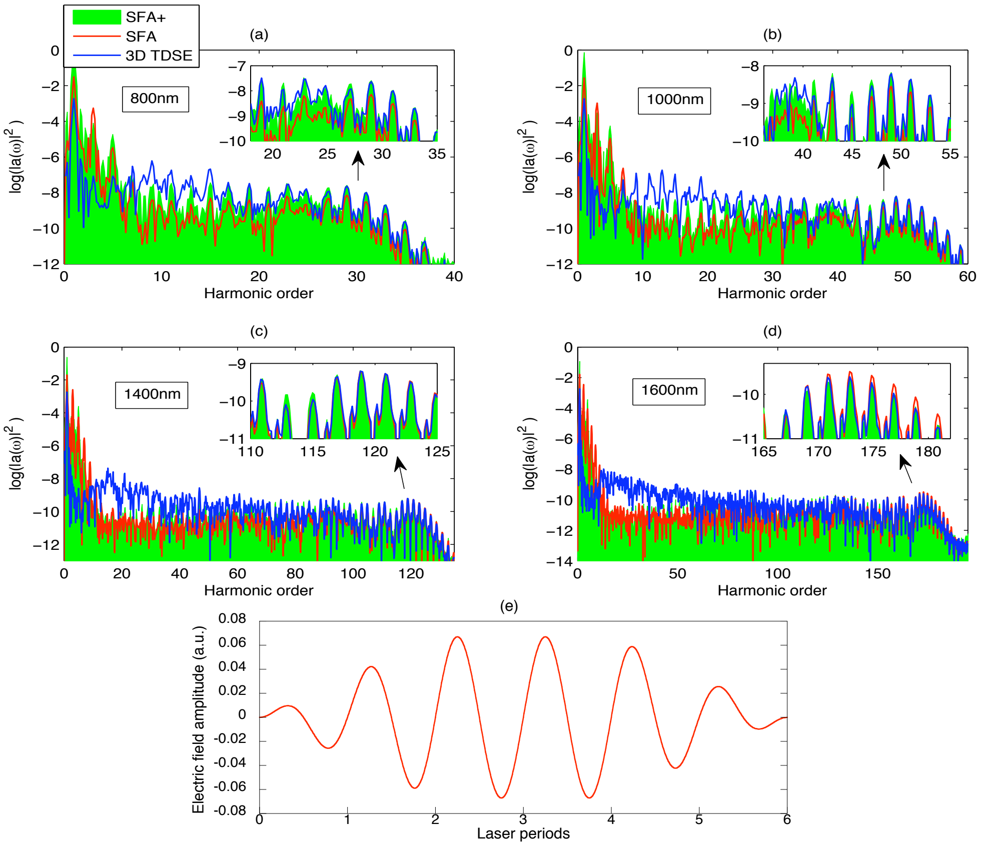

Figure 2.5: Identical parmeters than in Fig. 2.4 but in this case we have used a 6-cycles trapezoidal shape with 2-cycles of turn-on, 2-cycles of flat-top and two cycles of turn-off plotted in panel (e).

The next test is to study the accuracy of SFA+ in the transition from multiphoton to tunnel by increasing the laser wavelength. In Fig. 2.3 we present the HHG spectra corresponding to wavelengths increasing from near infrared (NIR) ($800nm$) to mid infrared (MIR) ($1600nm$). Increasing the laser wavelength causes

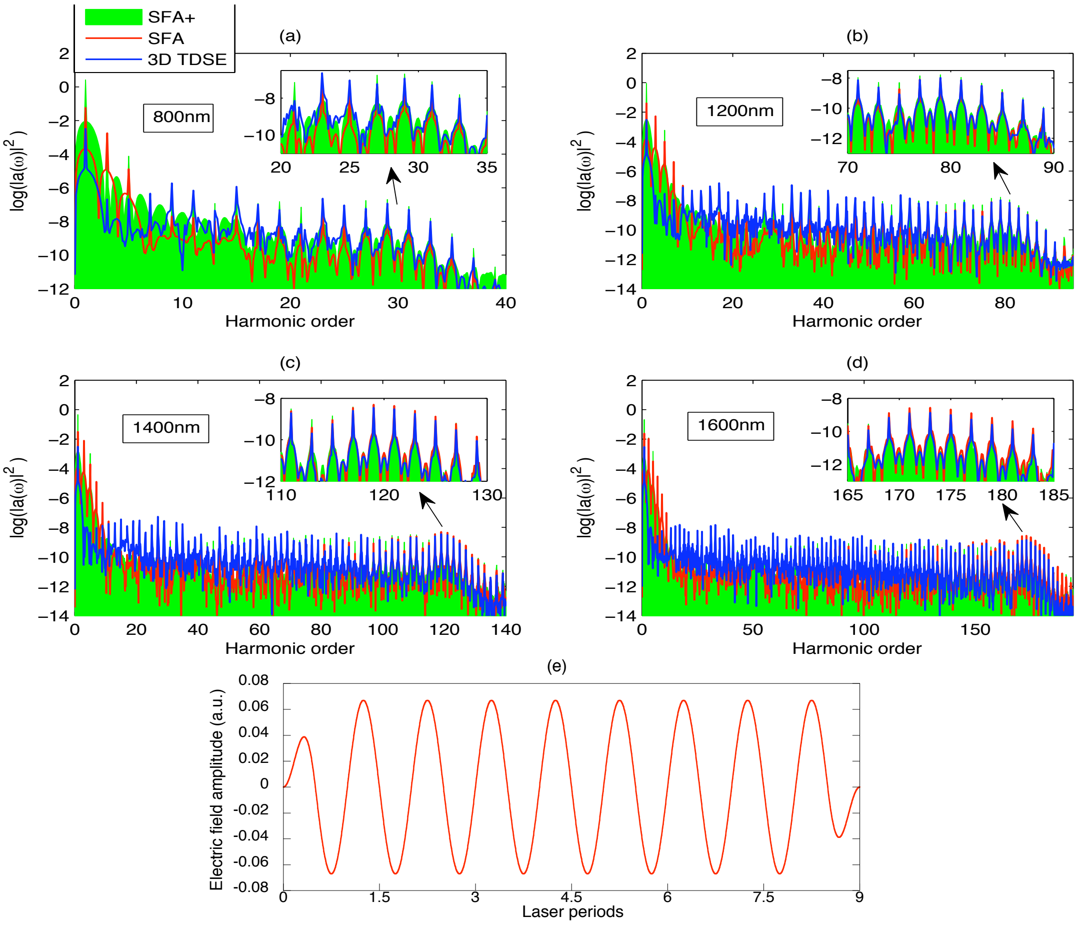

Figure 2.6: The same as in Fig. 2.4 and Fig. 2.5 but here we have used a 9-cycles trapezoidal shape, with 1/2 of turn-on, 8 cycles of flat-top and 1/2 of turn-off (panel (e))

the transition bewteen the multiphoton ionization regime cases, panels (a) and (c) to the tunnel regime, panels (b) and (d). Note that SFA+ adjusts correctly in the the cut-off with the 3D TDSE spectra in all cases. In order to extend our tests we will now study the HHG spectra in tunneling regime at different laser wavelengths, and using diferent input pulse shapes. The Fig. 2.4 shows HHG spectra in a typical tunnel situation (see the caption of this figure), at different laser wavelengths. Note that the SFA tends to converge with the SFA+ and 3D TDSE in the case of $1600nm$, in consistence with the fact that the SFA works better in the more tunnel situations. Note however that in this case SFA works just in the cut-off at long wavelengths (see panels (c) and (d) in Fig. 2.4), but fails just before the cut-off (see the insets in the same panels) in contras with the SFA+ that reproduces accurately a wide zone in the high frequency part of the plateau. As we will show in the next section, this fact is crucial to estimate correctly the harmonic yield integrated over the corresponding range of energy in the HHG spectrum. The two following figures, Fig. 2.5 and Fig. 2.6 represents the same situation of Fig. 2.4 but computed with different pulse shapes. In the spectra of Fig. 2.5 a 6-cycles trapezoidal shape with two cycles of turn-on, two cycles of flat-top and two cycles of turn-off is used in our simulations. Note that the accuracy of SFA+ HHG spectra seems not altered by the form of the pulse shape. Similar results are obtained for a longer trapezoidal shape with a more abrupt turn-on and turn-off, as it is shown in Fig. 2.6. The last cases plotted in Fig. 2.5 and Fig. 2.6 will be studied and analyzed in detail in the next section, to estimate the behaviour of the harmonic yield when the laser wavelength is increased.

2.2.2 Scaling of the harmonic yield with the laser wavelength

The study of the HHG in the short-wave infrared (SWI) nowadays constitutes a hot topic due to the rapid development of high-power lasers sources in this spectral range, based on optical parametric amplification. It is, therefore, of interest to explore the efficiency of the HHG process with the increase of the wavelength. We may note, however, that the efficiencies measured in an experiment are subjected to the details of the propagation of the fields in the target [39]. In the simplest case of an isolated atom, we may expect to derive some conclusions that may have a more universal character. Therefore, the study of the single-atom response still appears to be the most reliable source for the understanding of wavelength-dependent characteristics HHG. Previous theoretical studies on the scaling of the harmonic yield with wavelength show a divergence between the predictions of standard SFA and the exact 3D TDSE [40, 41]. From the viewpoint of this thesis, this issue is of fundamental interest as it constitutes an interesting divergence from the predictions of the standard SFA model, that may be reduced using SFA+. From a practical side, the correct scaling of the harmonic yield is fundamental for the quantitative description of the HHG with short- and mid-wave infrared sources, which may be used to generate shorter single attosecond pulses [42]. Here we will first drive a critical discussion of the results reported on these previous works [35, 40, 41]. In a first place, we shall derive a critial discussion of these studies as, to our understanding, they are comparing TDSE with SFA in spectral zones where the latter is not applicable. Second, we will demonstrate that even in its region of applicability, there is still a discrepancy between SFA and the exact results from the 3D TDSE. Finally, in the third place, we will demonstrate that SFA+ gives a more accurate account of the scaling law, demonstrating therefore that the physics involved in the scaling laws falls beyond the standard SFA.

As discussed above since the standard SFA neglects atomic bound-state excitations, we should expect SFA theories to reproduce faithfully only the higher frequency part of the harmonic spectra and not the whole (this fact is also recognized in [35]). In contrast to compute the harmonic yield, references [35, 40, 41] consider a *fixed* energy interval from 20 eV to 50 eV that falls deeply inside the harmonic plateau as the wavelength increases. To avoid this, our choice is to consider a spectral window of 10.2 eV right below the end of the plateau (i.e. the cut-off frequency), which is moved jointly with the spectrum cut-off as the wavelength increases.

Fig. 2.7(a) shows, for a particular case, the location of the window used by us (dashed black lines) and the one used in these previous works (dashed red lines). Fig. 2.7(b) shows the detail of the spectrum in the later case jointly with the results computed for the S-Matrix SFA models in $\mathbf{E}\cdot\mathbf{r}$ and $\mathbf{p}\cdot\mathbf{A}$ gauges (red and orange graphs), SFA+ (green) and the exact 3D TDSE result (blue). Note that the SFA is known to break the gauge invariance of the theory. This, therefore, imposes a stricter test of our approach, since it must be tested against

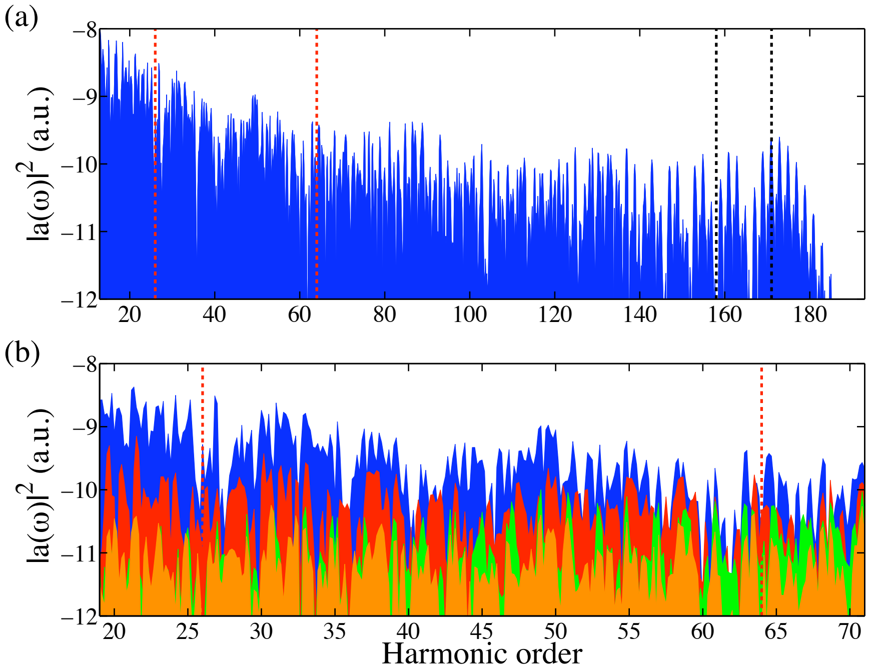

Figure 2.7: Harmonic spectra resulting from the exact integration of the 3D TDSE (blue), SFA in $\mathbf{E}\cdot\mathbf{r}$ and $\mathbf{p}\cdot\mathbf{A}$ gauges (red and orange) and SFA+ (green). Part (a) shows the location of the spectral windows used to compute the harmonic yield in [35, 40, 41] (enclosed between red dashed lines) and the considered here (enclosed between black dashed lines). Part (b) shows the results of the exact 3D TDSE and the three models in the former case (red dashed window). The computation corresponds to a trapezoidal shape of 6 cycles (with 2 cycles of linear turn-on, 2 cycles of constant amplitude and 2 cycles of linear turn-off), peak intensity $I = 1.58 \times 10^{14}$ and wavelength 1600 nm.

the SFA results in both gauges. The failure of the three models to reproduce accurately the 3D TDSE spectrum in this window becomes apparent and suggest, as discussed above, that the process of harmonic radiation in the inner part of the plateau has a complex nature. On the other hand, the spectra computed at the window near the cut-off show a more accurate resemblance with the 3D TDSE (see Fig. 2.8), as will be discussed below. In table 2.1 we show the results of the scaling exponents derived from the exact computations of the 3D TDSE for three different laser pulse envelopes: sin^2 shape for the 4 cycle pulse, trapezoidal shape of 6 cycles (with 2 cycles of linear turn-on, 2 cycles of constant amplitude

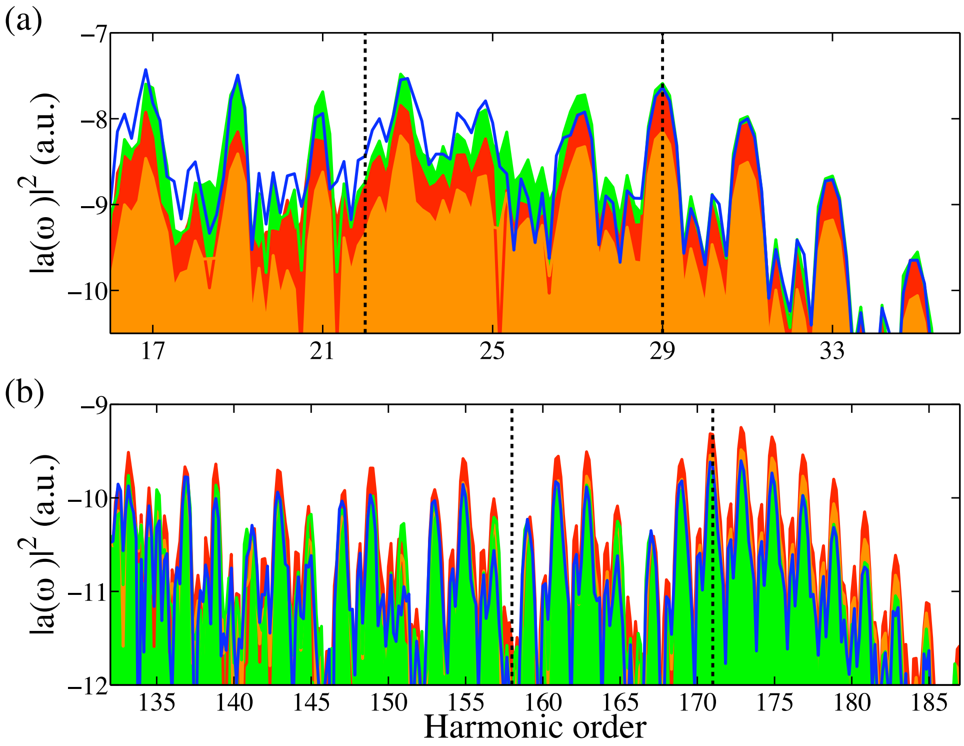

Figure 2.8: Higher frequency part of the HHG spectrum for a 6 cycles driving field of intensity 1.58×10^{14} W/cm^2 and wavelengths 800 nm (a) and 1600 nm (b). Part (b) corresponds to the same case shown in Fig. 2.7. As before, 3D TDSE results are plotted in blue, SFA in red (length gauge) and orange (velocity gauge), and the results of the SFA+ are plotted in green. The limits of the window used to compute the yields of table 2.2 are shown in black dashed lines.

and 2 cycles of linear turn-off), and a trapezoidal shape of 9 cycles (with 1/2 cycle of linear turn-on, 8 cycles of constant amplitude and 1/2 cycle of linear turn-off). This later corresponds to the field used in the previous works [40, 41]. The yields are computed integrating the harmonic spectra over the two spectral windows discussed above, and multiplying by the integration time. The scaling of the harmonic power (last column) corresponds to the closest harmonic near the cut-off frequency in order to avoid the energy difference between the 1s and 2p states (10.2 eV) in H. On this manner the chosen window excludes the possible interference with the harmonics generated through the 2p state. The tabulated results show stronger dependences of the scaling exponent with the pulse shape for the case of a fixed energy interval ($n \simeq 3.9 \pm 0.4$) than for the translating window near the cut-off ($n \simeq 5.6 \pm 0.1$). This suggests that this latter case is less sensitive to the details of the electromagnetic pulse. Moreover, the difference between the scaling powers of the yields computed at each window suggests a different mechanism for HHG. In any case, as a main conclusion, our results confirm the discrepancy between the scaling powers of the exact 3D TDSE results ($n \simeq 5.6$) and the expectations of the standard SFA models (n between 3 and 4) also for the higher frequency part of the harmonic spectrum.

Table 2.1: Exponents n of the scalings λ^{-n} of the harmonic yields computed from the exact integration of the 3D TDSE at an intensity $I = 1.58 \times 10^{14}$ using a fixed energy window (20-50 eV, enclosed between red lines shown in Fig. 2.7(a)), using a 10.2 eV window below the cut-off frequency ω_c (enclosed between black lines in Fig. 2.7(a)) and of the harmonic power at the nearest harmonic to the cut-off frequency. SFA+ result for the case of the fixed window and the field of 9 cycles agrees with the one reported in [41].

envelope	yield (20 eV- 50 eV)	yield ($\hbar\omega_c$-10.2 eV)	Power @ $\hbar\omega_c$
4 cycles	3.63	5.38	6.82
6 cycles	3.20	5.59	6.82
9 cycles	4.88	5.92	6.67

Fig. 2.8 shows the higher frequency part of the harmonic spectrum for the six-cycle electromagnetic driving field at wavelengths of 800 nm and 1600 nm (part (a) and (b) of the figure). The results of the exact solution of the 3D TDSE are plotted in blue color, the results of the SFA are shown in red (length gauge) and orange (velocity gauge), finally the results of our model are plotted in green.The most relevant conclusion of this figure is that the SFA+ has the best quantitative agreement with the 3D TDSE for both wavelengths. Incidentally, note also in Fig. 2.8 that SFA in the length gauge is more accurate for the smaller wavelengths, while the velocity gauge is more accurate for the longer wavelengths. The better accuracy of SFA+ approach is a general behaviour at least for wavelengths between 800 and 1600, as it is shown in Fig. 2.9. Part (a) of this figure shows the harmonic yields computed from the exact integration of the 3D TDSE

(blue) and the present model (green), while part (b) shows the comparison between 3D TDSE (blue) and the S-Matrix SFA models in the length (red) and velocity (orange) gauges. We have also plotted the best fit to λ^{-n} in solid lines. Note that, linked to its better accuracy, SFA+ reproduces also quite accurately the scaling of the yields with the wavelengths. Therefore, as a main result, we conclude that the physical reason for the divergence between the scaling laws predicted by standard SFA models and the exact 3D TDSE can be attributed to the influence of the electromagnetic field in the ground state. It is important to stress that the dressing term in Eq. (2.16) imposes a new restriction which interferes with the standard. A higher scaling involves the destructive interference of two contributions to the total acceleration.

Table 2.2 shows the scaling exponents extracted from the three approaches and the 3D TDSE for the different pulse shapes used. The yields are computed using the window near the cut-off frequency and, therefore, are quite stable against the change of shape of the pulse. Note that the exponents derived from the SFA ($n = 3.61 \pm 0.16$ and $n = 3.06 \pm 0.06$) are also consistent with the expectations of the standard model (n between 3 and 4), as discussed above. On the other hand, it is also apparent the discrepancy of the standard SFA models with the exact 3D TDSE results ($n = 5.63 \pm 0.22$), and with the prediction of SFA+ ($n = 5.41 \pm 0.21$).

Table 2.2: Scaling exponents of λ^{-n} extracted from the harmonic yields computed at the final part of the plateau for the three approaches considered and the 3D TDSE (also shown in the third column of table 2.1). The cases labelled as 6-cycles correspond to the results shown in Fig. 2.9.

envelope	SFA $\mathbf{E}\cdot\mathbf{r}$	SFA $\mathbf{p}\cdot\mathbf{A}$	SFA+	3D TDSE
4 cycles	3.68	3.10	5.12	5.38
6 cycles	3.76	3.10	5.62	5.59
9 cycles	3.39	2.97	5.49	5.92

In conclusion we have demonstrated our theory to account for the proper scaling of the harmonic yields at the higher frequencies of the spectrum. Therefore

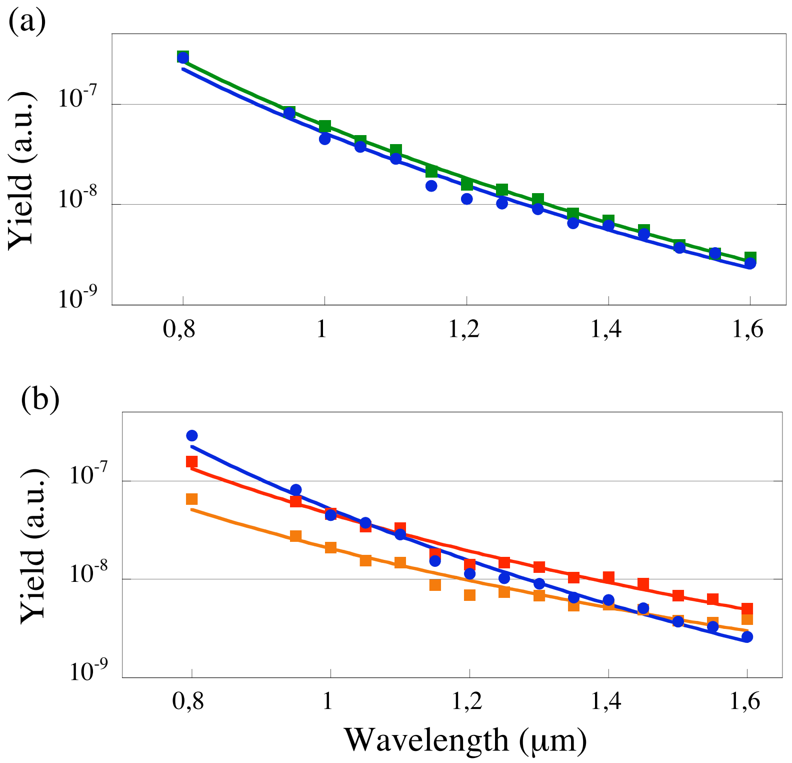

Figure 2.9: Harmonic yields computed using the window at the end of the plateau for a 6-cycle pulse of $I = 1.58 \times 10^{14}$ and for wavelengths ranging from 800 to 1600 nm. (a) Comparison between results from the 3D TDSE (blue) and the SFA+ (green), (b) comparison of the 3D TDSE (blue) with the SFA in length (red) and velocity (orange) gauges.

our interpretation of the discrepancy of the scalings of the harmonic yield between the standard model (based on SFA and saddle point approximation) and the exact results of the 3D-TDSE, reported in [40], is the influence of the electromagnetic field in the bound-state dynamics of the atom.

2.2.3 Phase and temporal description of the high-order harmonic radiation

As we have seen before SFA+ provides a quantitative accurate description at the high frequency part of the HHG spectra in a wide variety of situations, including different pulse shapes, pulse lengths, intensities and wavelengths. In this section we will analyze the accuracy of the SFA+ to describe the harmonic phase of the HHG spectra. This can be done either comparing the spectral phases between

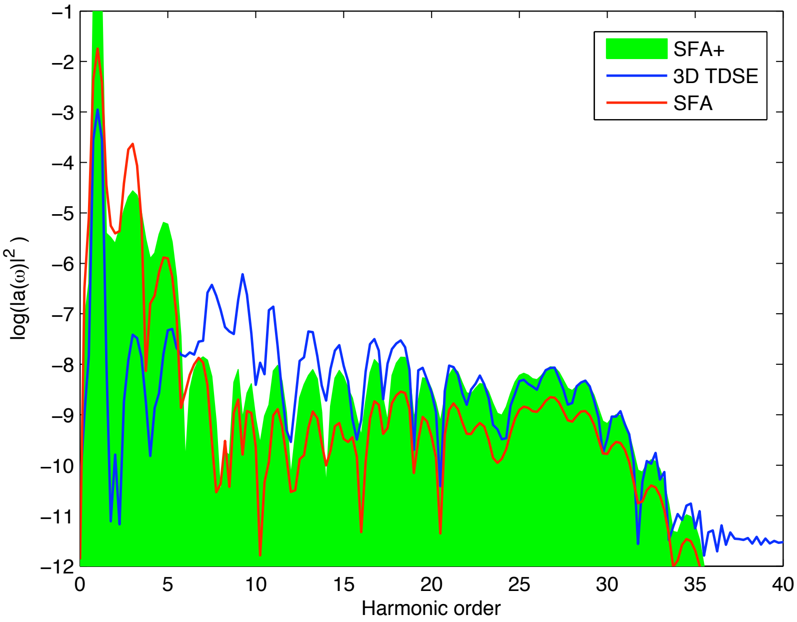

Figure 2.10: HHG spectra in hydrogen corresponding to a four-cycle sin^2 envelope and peak intensity $1.57 \times 10^{14} W/cm^2$ at $800nm$, computed with the SFA+ (green), SFA (red) and 3D TDSE (blue).

the different methods, studying the differences in the time-frequency analysis or, alternatively, comparing the inverse Fourier transform of the spectra, i.e. $a_b(t)$ in Eq. (2.14) (SFA), with $a(t)$ in Eq. (2.21) (SFA+) and with the results of the exact integration of the 3D TDSE. We will consider as a test case the interaction with a four-cycle sin^2 pulse at peak intensity $1.57 \times 10^{14} W/cm^2$ at a wavelength of $800nm$. The value of peak intensity of the laser does not exceed the saturation value of the target atom (in this case, hydrogen), to avoid the complete suppression of the tunnel barrier (which is not included in the SFA approaches considered in this thesis). The spectra obtained for this case are plotted in Fig. 2.10. In previous analysis, we have demonstrated that the magnitude of the error of the SFA

prediction depends on the particular case considered (field intensity, wavelength and pulse-shape) while the SFA+ approach reproduces the 3D TDSE results with errors tipically within a factor less than 1.5 in all cases.
To explore the detailed spectral and temporal behaviour of HHG, in Fig. 2.11 we perform the time-frequency analysis by means of the wavelet transform [43, 44, 45, 46] of the induced dipole acceleration responsible of the HHG spectrum of Fig. 2.10. On this manner is possible to identify the recombination events or,

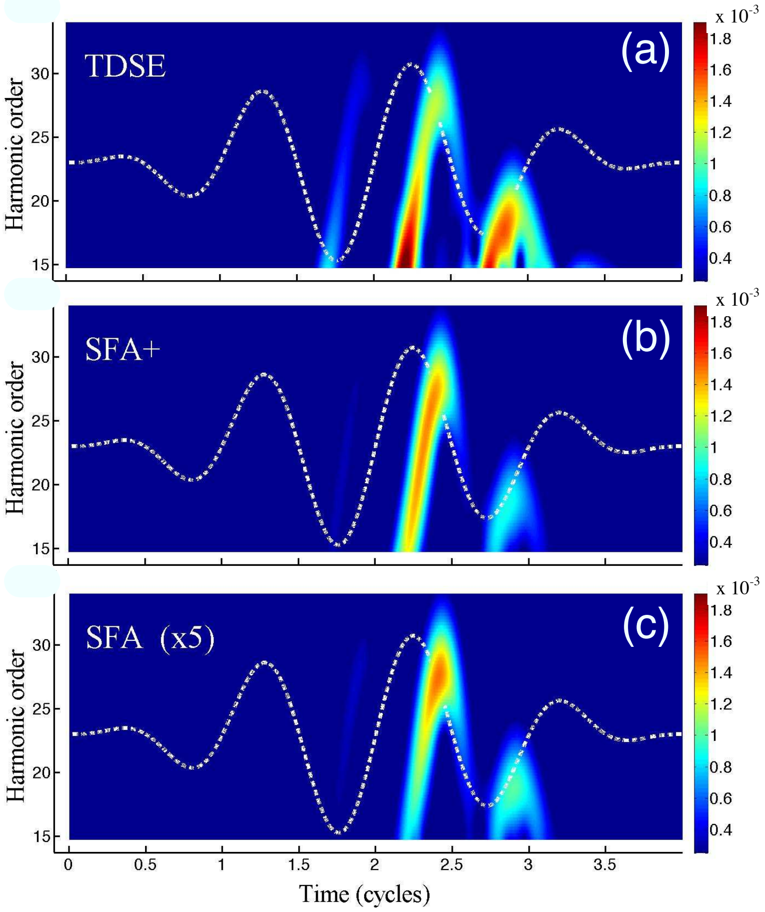

Figure 2.11: Time-frequency analysis corresponding to the spectra shown in Fig. 2.10: (a) the exact 3D TDSE (b) SFA+ (not rescaled), (c) SFA (rescaled to the same intensity level than the previous cases). The dotted white line represent the driving laser puse.

in other words, the instant when the harmonics are emitted along the laser pulse and its corresponding recombination energy.

Note that to allow for a better comparison, in panel (c) of Fig. 2.11 the SFA results have been scaled by a factor 5 in order to match the same scale as the 3D TDSE and SFA+ cases (panels (a) and (b) respectively). The harmonics below the order $15th$ have not been included in the y-axis as their correspond to the lower frequency region, where none of the SFA approaches is accurate. The exact computation via 3D TDSE shows that the harmonics are generated in three bursts, corresponding to the rescattering of electrons ionized near the field maxima at approximately $1.25T$, $1.75T$ and $2.25T$, being T the laser period. The maximum harmonic frequencies correspond to the second burst for which the ionized electrons accumulate the maximum kinetic energy before rescattering. These overall features are also found in the SFA models, however the intensity first burst seems to be much weaker in these cases. The reason for that is not clear, but suggests that the ionization at lower field amplitudes is less efficient in the SFA models compared with the 3D TDSE.

SFA and SFA+ models predict that the efficiency of the harmonic generation via shorter paths is greater than via longer paths. This is in agreement with the 3D TDSE and should be interpreted in terms of the spreading of the wavefunction of the recolliding electron, which is greater for the longer trajectories. As mentioned above, the accuracy of SFA+ in the description of the harmonic intensity spectrum does not need to imply that the spectral phases are well reproduced. To adress this question, Fig. 2.12 shows a detail of the higher-order harmonic spectral phases. The red, blue and dotted black lines, respectively in panels (a), (b), (c) in this figure, correspond to the intensity spectrum (shown for all frequencies in Fig. 2.10) and the grey lines to the derivative of the spectral phase $d\phi(\omega)/d\omega$. These two quantities provide the complete information of the radiated field. As we have exposed in section 1.4 the derivative of the spectral phase is proportional to the difference of the harmonic emission times, i.e. the chirp of the harmonic emission. Positive derivatives correspond to negative time intervals and reverse. Note that, as a general trend, the derivative of the spectral phase near the end of the harmonic plateau tends to increase with the harmonic frequency. Therefore, higher harmonic frequencies are emitted at shorter times and the harmonic yield is positively chirped for the highest frequencies [47]. This behavior is found in the 3D TDSE as well as in both SFA models. An additional test is shown in

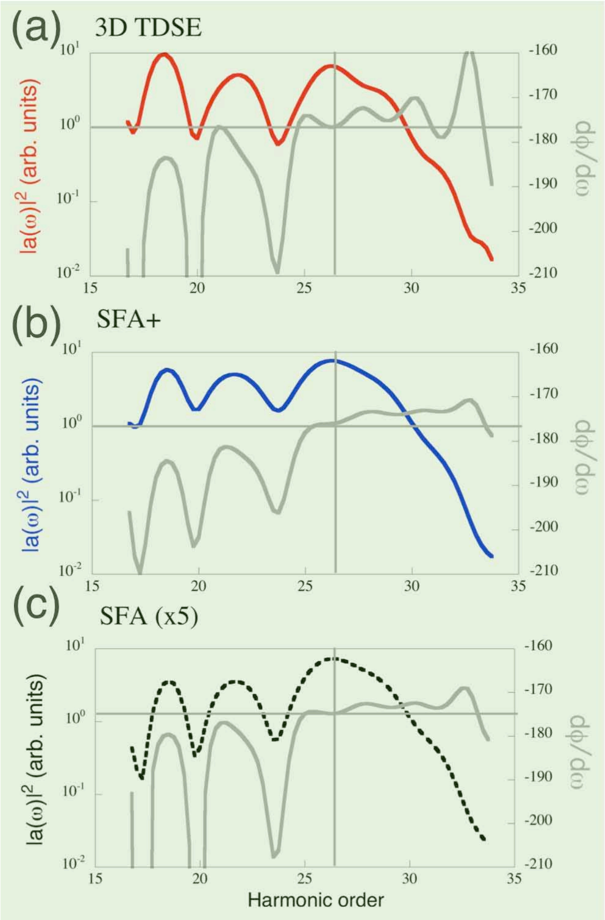

Figure 2.12: Harmonic intensity (red, blue and dotted black lines, respectively) and first derivative of the spectral phase, $d\phi(\omega)/d\omega$ (grey line), close to the cut-off for the computations shown in Fig. 2.10. (a) exact results from the 3D TDSE, (b) results from SFA+, and (c) results from the SFA.

Fig. 2.13 where we plot the inverse Fourier transform of the higher prequency part of the plateau. The Fourier synthesis of the final part of the harmonic spectrum (spectral window starting at the harmonic 21st). The higher frequency part of the harmonic spectra is known to posses phase-locking properties and, therefore, corresponds to a temporally narrow high-frequency pulse of durations typically below the femtosecond. The figure shows the envelope of the pulses

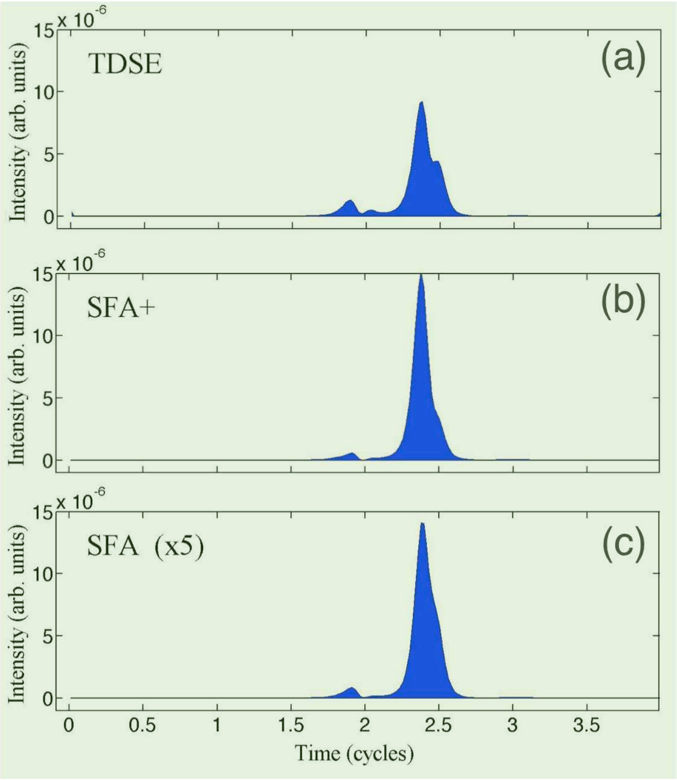

Figure 2.13: Envelopes of the XUV electromagnetic fields resulting from the Fourier synthesis of the last part of the spectrum of Fig. 2.10 (starting from the 21*st* harmonic). (a) exact results from the 3D TDSE, (b) results from SFA+ model, and (c) results from the SFA.

synthesized using the SFA models and the 3D TDSE. For better comparison, the results of the SFA are rescaled by a factor five, while the 3D TDSE and SFA+ results are plotted in absolute scale. Probably the most appealing result is that the Fourier synthesis of the SFA spectra gives rise to a sharper attosecond peak with a duration smaller than the exact 3D TDSE. This means that SFA models overestimate the phase locking of the harmonics and, therefore, provide pulses closer to the Fourier limit than in the exact 3D TDSE case. This is consistent with the data plotted in Fig. 2.12, where the derivative of the spectral phase was oscillating more strongly in this later case and, therefore, the phase distribution is less ordered.

In conclusion, in this section we have analyzed the time and spectral phase descriptions of the harmonic field generated by a hydrogen atom, comparing the results of the exact solution of the Schrödinger equation and two SFA models. We have demonstrated that the standard SFA approach leads to an underestimation of the harmonic intensities near the plateau's cut-off while our correction to the SFA (SFA+) gives a better absolute description. This is in agreement with our previous results, in which the error of the SFA approach is shown to depend on the parameters of each particular case while SFA+ results generally agree within a factor 1.5. From the point of view of the spectral phases, we have seen that both SFA models describe correctly the positive chirp of the harmonic radiation near the plateau's end. In a more detailed scale, both SFA models also show an oscillating pattern of the derivative of the spectral phase which is qualitative accurate in comparison with the 3D TDSE results, but with amplitudes significantly smaller. The source of this modulations is identified as the interference of two consecutive burst of harmonic emission approximately separated by half of the field cycle. Our wavelet analysis show that the SFA models underestimate the intensity of the first burst. On the other hand, both SFA models predict the harmonic generation as a result of two collisional paths related with short and long electron trajectories. We finally we would like to stress once more that our tests of the SFA models are done without resort to the standard saddle-point approximation. As a result the models considered here are fully quantum, not semiclassical. Our data show that the radiation bursts related with the shorter trajectories are more intense than those related with the longer, a result that agrees with the exact 3D TDSE integration.

2.3 Full quantum aspects of SFA+

2.3.1 Momentum space description

As we have stressed above, if the stationary phase approximation is avoided the full quantum description is retained, making possible to extract information beyond the picture of quantum trajectories. In the following we will show that the fact that the SFA+ do not uses the stationary phase approximation constitutes a practical tool to make a fine study of the quantum nature of the harmonic radiation. We shall remind that the SFA+ computes the harmonic spectrum from the superposition of independent contributions of each Volkov wave. In contrast, the standard SFA approaches, based on the saddle point approximation, consider only the most relevant contributions to the momentum space integral, leading to a semiclassical description in terms of quantum trajectories. It is, therefore, of interest to analyze the role of the different momentum space regions to the harmonic generation process. For this goal we consider the Fourier transform of $a_b(\mathbf{k}, \mathbf{t})$, as given by Eq. (2.22). We define the total contribution of continnum states with axial momentum k_z as the integral over the transverse plane

$$a(k_z, \omega) = -\int dk_\rho k_\rho d\phi \frac{\hbar^2 k^2/2m - \epsilon_0}{\Delta_s} a_b(\mathbf{k}, \omega) \tag{2.23}$$

Figure 2.14 shows these contributions for the case of two different intensity regimes in hydrogen atom. Panel (a) represents the multiphoton regime ($I = 5.0 \times 10^{13} W/cm^2$) and panel (b) corresponds to the tunneling regime ($I = 3.50 \times 10^{14} W/cm^2$). An interesting feature of this plot is the presence of spectral contributions well above the spectral cut-off Eq. (1.13), which is marked by vertical

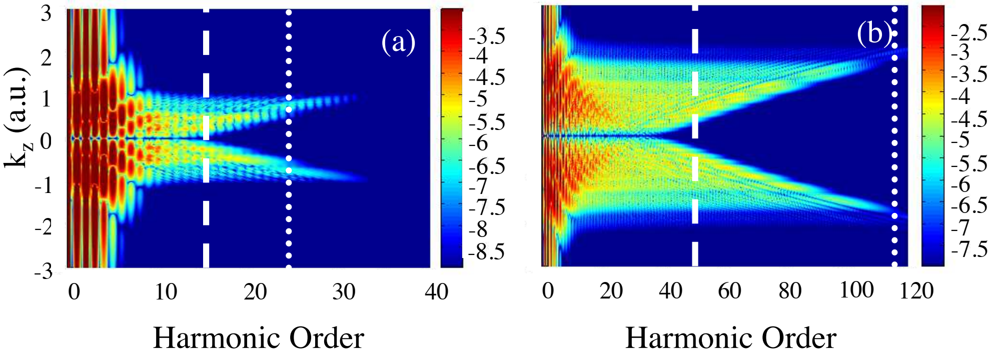

Figure 2.14: k_z spectral contributions to the total harmonic radiation corresponding to two different laser intensities, (a) $5.0 \times 10^{13} W/cm^2$ and (b) $3.50 \times 10^{14} W/cm^2$ both at $800nm$, computed with the SFA+. Vertical dashed lines represent the maximum cut-off frequency ($I_p + 3.17U_p$) of the integrated spectrum which corresponds to the electrons returning to the atomic core. The vertical dotted lines denote the maximum kinetic energy of the trajectories of the non-returning electrons, $I_p + 8U_p$. The harmonic intensities are plotted in logarithmic scale

lines. Note that in both cases (multiphoton and tunnel) harmonics higher can be generated with frequencies far beyond this semiclassical cut-off, reaching photon energies up to $I_p + 8.0U_p$ which is the maximum kinetic energy can be achieved by an electron ionized with zero initial velocity [48, 49]. The study carried out in these references reports on that in spite of the trajectory with energy $8.0U_p$ has its maximum so far from the parent ion, the harmonic emission can be possible as long as there are another centre of scattering (for instance, a second ion resulting from a dissociated molecule). Since the momentum wavefunctions are planewaves, they are extended in space, therefore there exists always an overlap with the parent ion and, thus, the harmonic emission can be emitted to the upper limit, $8Up$. Therefore, each momentum may contribute with radiation of frequencies well above the semiclassical limit, $I_p + 3.17U_p$. Note however that, as the integration in momentum space is carried on, these high-energy contributions cancel with each other and the final spectrum converges to the semiclassical limit. This cancellation is carried on directly in the theory if the stationary phase approximation is employed. However, the fact that in the tunneling case the radiated energy remains always below the $I_p + 8.0U_p$ limit, gives ground to the semiclassical assumption that in this regime the electrons are ionized with zero velocity. Also, in this later case, the fact that the total spectrum still shows contributions above the $I_p+3.17U_p$ limit, points out the possibility of recombination associated with non-returning classical trajectories. The ultra-high frequencies do not show up in the total spectrum due to the rapid change of the phases of $a(k_z, \omega)$ with k_z, that leads to a destructive interference.

2.3.2 Semiclassical and quantum aspects of harmonic generation via SFA+. Electron wavepacket delocalization

As we have mentioned above, from the semiclassical point of view, the high-order harmonic generation process can be drawn directly from the Eq. (2.14): the electron remains in the ground state of the atom until it is perturbed by the field, at some time instant t_1. Afterwards, it evolves under the influence of the field and the Coulomb potential, until it recombines with the ground state, emitting radiation. The SFA simplifies this picture by assuming that the electron previously ionized, evolves in the continuum neglecting the influence of the atomic potential. Applying the stationary phase approximation, a semiclassical picture emerges in which the electron appears in the continuum with zero velocity and localized at the ion, then evolves as a classical particle, and recombines when its trajectory crosses again the electrons birth coordinate. The maximum energy of the harmonics radiated is, then, directly related with the electron's kinetic energy at the moment of the recollision. In this context, therefore, the whole process of harmonic generation is the sum of the contributions of each possible electron trajectory associated to a particular ionization event during the interaction. Two of these classical trajectories are plotted as black lines in Fig. 2.15(b) and 2.16(b), corresponding to the electron ionized when the electric field is close to its maximum and when it is zero, respectively. As can be easily seen, harmonic generation differs substantially between these two cases: when the electron is released near the field maximum it rescatters with the nucleus after less than a half laser period while, if released at a zero of the field, no rescattering occurs after ionization. Therefore, according to the semiclassical picture, harmonics are only generated in the first case.

The structure of Eq. (2.14) allows to isolate the contribution of a particular ionization instant in a natural way, by simply replacing $V_i(t_1)$ by $V_i'(t_1) \equiv W(t_1)V_i(t_1)$, being $W(t_1)$ a time window defined as $W(t_1) = \exp\left[-(t-t_c)^2/\tau^2\right]$. Note that $W(t_1)$ only restricts the time interval allowed for ionization process, i. e. the electron dynamics in the continuum is unaltered. According to the semiclassical view exposed above, Fig. 2.15(b-c) and Fig. 2.16(b-c) show the time dependence of the total acceleration Eq. (2.21) when the time window $W(t_1)$ is centered near the maximum ($t_c = 3.29$T) and the zero of the field ($t_c = 3.5$T), respectively. In both cases the width of the window is defined as $\tau = 1/16T$. A close inspection of both cases reveal some features unexpected with the semiclassical analysis. In the following we will analyze the results shown in Fig. 2.15. Part (b) corresponds to the multiphoton case discussed in the last section in Fig. 2.14(a), and part (c) to the tunneling case of Fig. 2.14(b). In both situations, the black line corresponds to the classical trajectory of an electron born near the field maximum, at the time where the window $W(t_1)$ is centered. There are two interesting features, in both ionization regimes, which depart from the ideas drawn by the semiclassical approach. On one hand, a strong acceleration (and therefore harmonic radiation) is generated *before* the rescattering event. Therefore, this demonstrates that harmonics are also generated in the *way out* of the ionization process, when the electron departures from the atom. In the tunneling case, however, the acceleration is strongly chirped, so that the higher spectral frequencies are generated near the classical times of the rescattering.

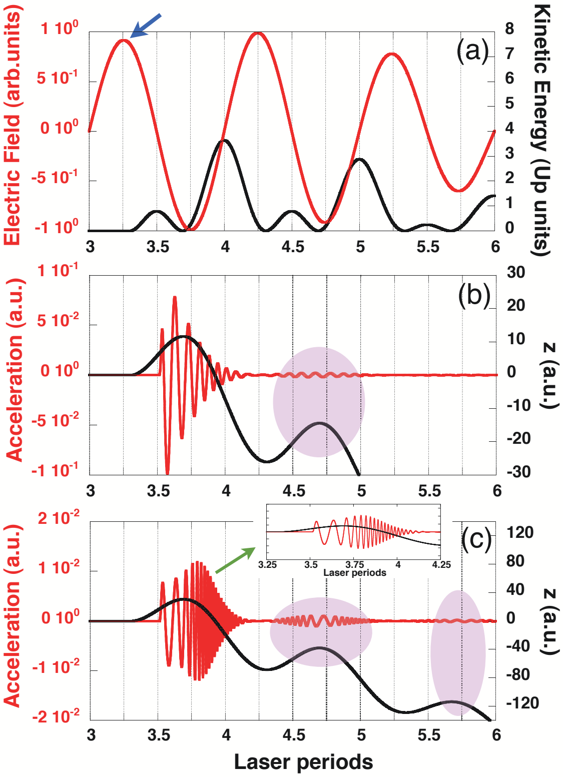

Figure 2.15: (a) electric field (red line) and kinetic energy (black line) associated with the classical trajectory of an electron assumed to be ionized near the peak amplitude (blue arrow). (b) electron trajectory associated to this situation (black line) and dipole's acceleration (in time) computed from SFA+ for the corresponding time window for the multiphoton case of Fig. 2.14(a). (c) the same for the tunnel case of Fig. 2.14(b). The inset shows a zoom of the acceleration close the classical time for recollision. The meaning of the shadow areas in (b) and (c) is explained in the text.

This explains the success of the semiclassical theory to describe the nature of the harmonic radiation at the higher frequency part of the spectrum. Note that the up chirping near the time of rescattering, can be interpreted classically as due to the contribution of short trajectories. However, in the multiphoton regime the chirp is reduced and the frequencies of the harmonics generated during the *way-out* are similar to those generated at the rescattering.

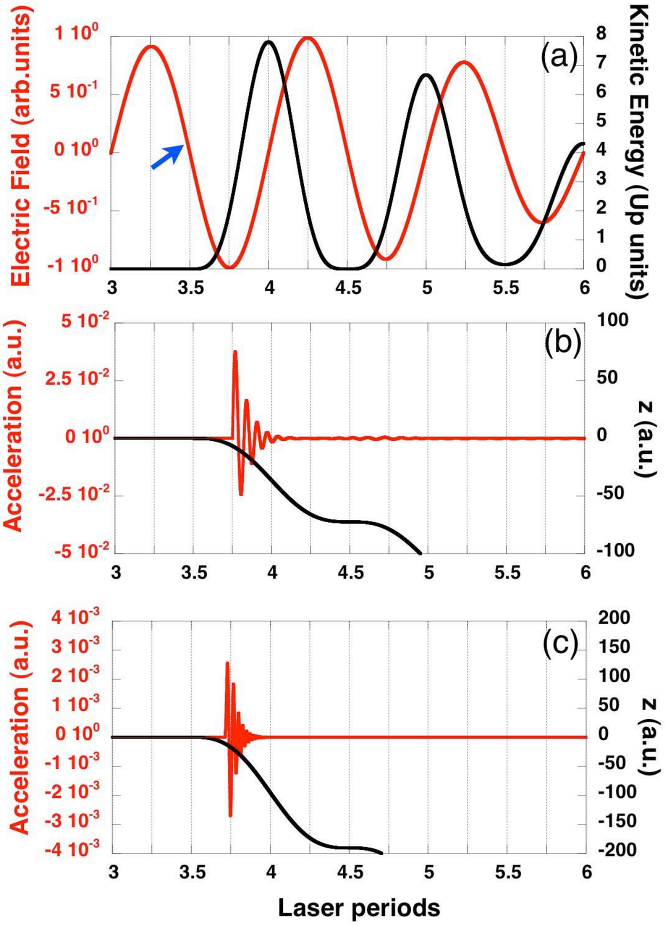

Figure 2.16: (a) electric field (red line) and kinetic energy (black line) associated with the classical trajectory of an electron assumed to be ionized at the field's zero (blue arrow). (b) electron trajectory associated to this situation (black line) and dipole's acceleration computed from SFA+ for the corresponding time window for the multiphoton case of Fig. 2.14(a). (c) the same for the tunnel case of Fig. 2.14(b).

The second interesting feature is the presence of secondary bursts of radiation associated with times in which the distance of the quivering electron with the parent atom reaches a minimum (see the shadow areas in the plots (b) and (c) of Fig. 2.15). Note that, as the electron trajectory does not cross the coordinate origin, this mechanism of *close up* radiation is no described in the semiclassical theory. These bursts are found to be down chirped in their first half and up-chirped in the second, in correspondence to the kinetic energy of the electron around the time instant of maximal approach to the atom. In the tunneling regime, the maximum frequency of these burst falls well into the plateau region, so the semiclassical theory is safe when neglecting its contribution to describe the higher spectral frequencies. In the multiphoton case, the frequency of the close-up radiation is again similar to the those at the end of the plateau, and cannot be neglected to explain the source of the higher-order harmonics.

To our understanding, the physical mechanisms underlying *way-out* and *close-up* harmonic radiation are associated with the delocalization of the wavefunction in the continuum: first, the electron's wavepacket is not perfectly localized at the instant of ionization, second, the wavepacket spreads during the excursion through the continuum and, finally, the recombination does not take place at the coordinate origin, as the acceleration operator has some spatial extension. As a result, the overlap of the ionized wavefunction with the ground state and the acceleration operator remains operative in situations where the classical trajectories are far from the nucleus.

The same analysis can also applied to the case of Fig. 2.15 (b-c) where we show the acceleration associated to the ionization of a wavepacket near the zero of the field. In this case, the classical trajectory never comes back to the nucleus, therefore the harmonic generation is forbidden semiclassically. Our results show, however, that harmonics are generated right after the ionization, when the electron leaves the parent ion. This *way-out* radiation is typically decreasing shortly after ionization and has frequencies also in the middle of the plateau. Note that although the electron's kinetic energy can reach $8U_p$ in its way out (for instance at the beginning of the 4 cycle), this possibility is not mapped into the harmonic frequencies, since they are dominated by the slower part of the wavefunction, which is the one remaining closer to the parent ion. Note that, in the tunneling case, the amplitude of the acceleration during this way-out process is substantially smaller than when the electron departs near a maximum of the field. This later fact is consistent with the known dramatic decrease of the tunnel ionization probabilities when the field amplitude decreases.

2.4 Results for other atomic species: He

As we mentioned in the introduction, multi-electron atoms in intense laser fields need to be treated within an additional approximation known as: the *Single Active Electron approximation* (SAE), in which is assumed that only one electron, the most external (i.e. the most weakly bound), interacts with the laser field. This approximation neglects the correlations between the electrons considers that they remains in the ion as a *frozen core*.

So far, we have developed the SFA+ formalism considering the hydrogen as a target atom. However in the HHG experiments the chemical specimens most commonly used are noble gases. Therefore the next step is to extend the SFA+ formalism to these gases. For this goal we need to calculate the corresponding matrix elements in Eq. (2.14). For this purpose we use the generic atomic potential reported in [50] that describes accurately the helium and the rest of the gases

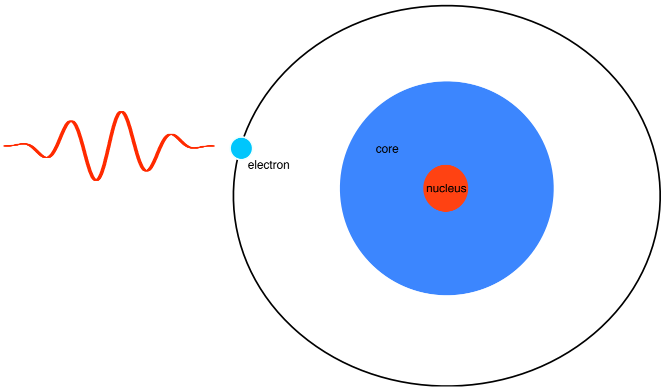

Figure 2.17: Schematic picture of an multi-electron atom in the SAE approximation which assumes that all electrons remain *frozen* in the orbitals forming a core and only one electron (the most external) interacts with the laser field.

nobles. On the other hand, we use the atomic wavefuncions for the gases nobles tabulated in [51]. To simplify this section, we shall only compare results computed by SFA+ with the 3D TDSE, as the SFA shows a behavior against SFA+ very similar to the already discussed in the previous section. Fig. 2.18 shows the HHG spectra in helium at two different laser intensities and two different laser wavelengths. Panel (a) corresponds to the multiphoton regime panels (b), (c) and (d) respectively, to the tunnel regime. As this figure shows, the SFA+ presents

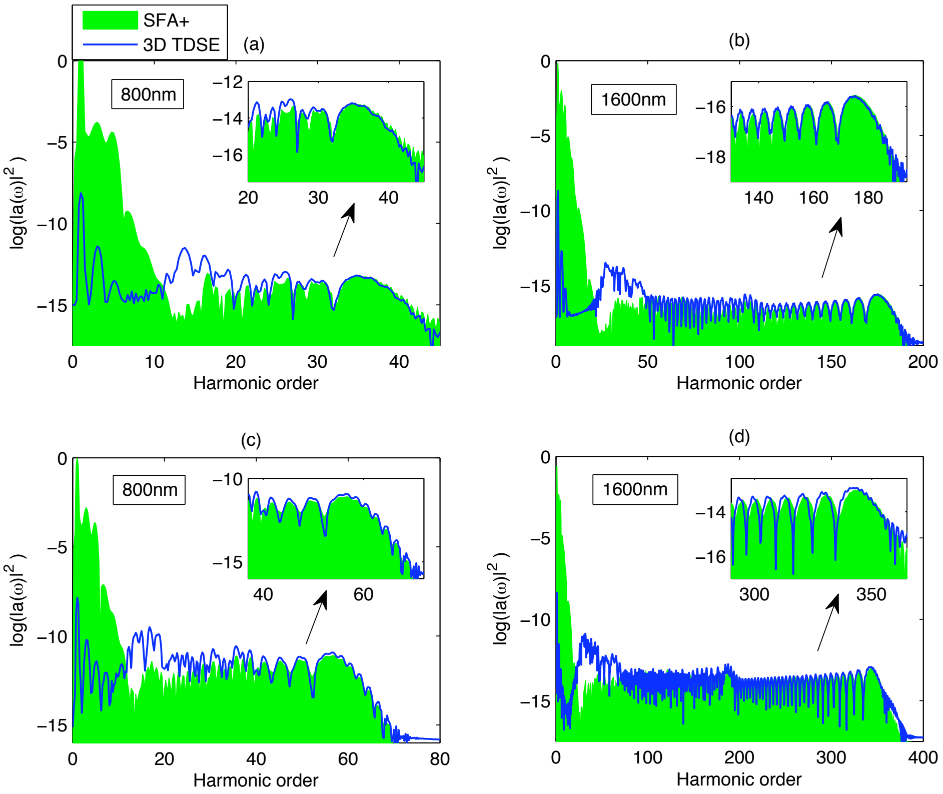

Figure 2.18: HHG spectra in helium atom for two different laser intensities and two different laser wavelengths. Panels (a) and (b) represent the espectra computed both at the same intensity, $5.0\times10^{13}W/cm^2$. Panels (c) and (d) are computed both at $3.50 \times 10^{14}W/cm^2$. In addition, panels (a) and (c) are computed at 800nm and panels (b) and (d) correspond to 1600nm. In (a) $\Gamma_K = 1.14$, in (b) and $\Gamma_K = 0.57$, in (c) $\Gamma_K = 0.76$ and in (d) $\Gamma_K = 0.38$. We have used 4-cycle sin^2 pulse envelope.

a high degree of agreement with the 3D TDSE results. Additional test in helium (not sown) with different intensities, pulse envelopes and different temporal duration reports also positives results.

3

HHG and Attosecond Pulse Generation beyond saturation

“ The more original a discovery, the more obvious it seems afterwards ”
Arthur Koestler

Before starting this chapter we would like to mention three questions that were proposed in the nineties (1993) by Ph. Balcou, P. Salières and A. L’Huillier in a seminal proceeding of the third SILAP meeting [52]: *How far* (in energy) can harmonics be generated?, *How many* photons can be produced? and *How well* is the radiation emitted?, or in other words, What is the spatial and temporal coherence of the harmonic radiation?. A high number of experiments carried out in the last two decades have been gradually addressing these questions. However, nowadays these questions still enclose a challenge.

3.1 Challenges, goals and the problem of saturation in HHG

As has been pointed out along this manuscript, HHG provides a direct and elegant route to achieve coherent radiation in the range from UV to soft x-rays using table-top laser sources. In the HHG spectrum, the cut-off frequency determines the highest possible photon energies for each particular driving laser pulse in terms of its intensity and wavelength.

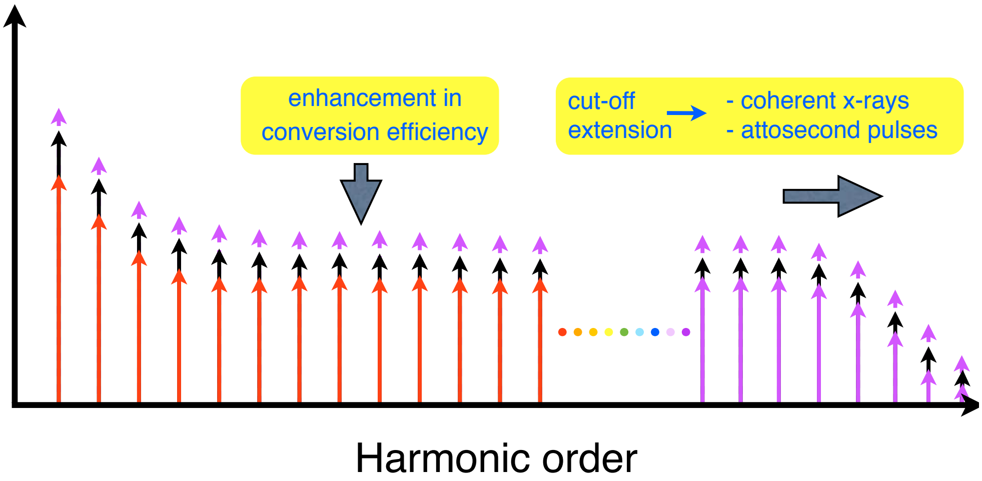

Figure 3.1: The typical power spectrum of HHG in the nonperturbative regime where we show schematically the main challenges for HHG optimization.

According to the cut-off law (Eq. (1.13)), the two possible ways to extend the harmonic cut-off to a higher frequency (i.e. high energy photons) consist in either increasing the intensity or increasing the wavelength of the input laser pulse, or both. It is however well known that when the laser wavelength is increased the harmonic generation efficiency decreases exponentially as $\lambda^{-5.5}$ [36, 40, 41, 53], although some works have demonstrated that this loss of efficiency can be compensated optimizing the phase matching conditions in hollow fibers [54, 55]. Another difficult aspect is that long wavelength MID sources sources are presently less developed than the standard NIR. These OPCPA devices, based in parametric conversion combined with CPA, are based on a technology not as mature as convetional CPA.

Therefore it is of interest to explore ways to extend the harmonic spectrum without incresing the driving laser wavelength. Chipperfield and coworkers [56] proposed theoretically *a perfect wave* form of the fundamental pulse, to optimize the rescattering energy of the electronic trajectories. The proposal suggest sculpting the perfect wave form from a controlled mixture of laser beams of different colors. This method predicts larger cut-offs and has been confirmed experimentally very recently [57]. Other approaches intend to increase the cut-off using chirped laser pulses [58] or choosing an appropriate target medium may be result in a significative extension of the cut-off frequency as predicted, in the last case, in dissociating molecules [48, 49, 61]. However this method needs a very precise control of the internuclear separation of the molecule.

An alternative way of achieving higher harmonics cut-offs is to increase the intensity of the driving laser, since, according to the cut-off law, the plateau's extension increases linearly with it. Unfortunately this growth is not unlimited, as it exists a *saturation* limit above this critical value, the harmonic efficiency drastically drops making HHG inefficient [62, 63].

In the two following sections we will expose two proposals to achieve high energetic harmonic cut-offs. Our first method (section 3.2) considers a driving laser consisting of two delayed pulses of the same color. The resulting waveform presents particular advantages to increase efficiently the harmonic cut-off. Our second proposal emerges from the detailed study of the intra-cycle electronic dynamics during the turn-on of the driving laser pulses. This will be detailed in section 3.4.

3.2 Extension of the cut-off in HHG using two delayed pulses of the same colour

In this section, we focus our attention into the *sculpting* of the input laser waveform in order to make more efficient the electron recombination, achieving higher harmonic cut-offs. Our technique consists of delaying the relative time between two replicas of an CEP-stabilized ultra-short pulse. One of the replicas is then shifted in phase in π with respect to the other (as a result, for instance of a reflection). The two replicas are then overlapped with a chosen relative delay [64]. We will show that the pulse sinthesized by this method presents considerable advantages, making more efficient the HHG process in comparison with the conventional approaches.

A preliminary low resolution scan over the CEP values of each pulse directed us towards the use of two sine-like pulses, as particularly suitable choice for extending the harmonic cut-off without increasing the peak intensity. Therefore, we fix these two parameters (peak intensity and CEP) and performed a detailed scan over the possible delays. The analytical expression of the resultant shaped field is given by

$$E(t,\tau) = \epsilon\left(t+\tau/2\right) - \epsilon\left(t-\tau/2\right) \tag{3.1}$$

being

$$\epsilon(t) = \begin{cases} E_0 f(t)\sin(\omega_0 t) & \text{if } 0 < t < NT \\ 0 & \text{otherwise} \end{cases}$$

where E_0 is the peak pulse amplitude, $f(t) = \sin^2\left(\frac{\omega_0 t}{2N}\right)$ is the shape of the envelope, ω_0 is the central frequency corresponding to $\lambda = 800$ nm, T is the laser period, τ represents the delay between both pulses, N is the total number of cycles in the laser pulse corresponding to an intensity envelope of FWHM $0.36NT$. In our case, $N = 2$ which corresponds to 0.72-cycle FWHM ($\simeq 1.87fs$ FWHM for $\lambda = 800nm$). This value is not so far for the pulse durations recently achieved, see for instance [65]. Fig. 3.2 shows the scheme of our temporal pulse shapping technique. The dotted line shows the maximum field value E_0 which is used to calculate $U_p = q^2E_0^2/4m\omega_0^2$. We highlight that this definition is taken as the reference energy unit in this chapter. In Fig. 3.2(b) we show the double pulse scheme shown in Eq. (3.1), for the case $\tau = 0.81T$

The TDSE is numerically solved for these fields, obtaining the harmonic spectra. In order to approach the conditions for optimal cut-off extension we have made extense scans over the delays using the one dimensional TDSE, (1D TDSE). The 3D TDSE is then used for the fine tuning of the optimal cases. For the case of 1D simulations we use a soft core potential of the form $V_c = -1/\sqrt{a^2+x^2}$, where $a = \sqrt{2}$ has been set to give ground state ionisation potential very close to the hydrogen (-13.6 eV). The integration scheme used in the 1D case is a split operator method. For the 3D case our code is based on spherical harmonics expansion, Y_l^m, considering only the $m = 0$ terms because of the cylindrical symmetry of the problem. The numerical technique is based on a Crank-Nicholson scheme implemented together with a splitting of the time evolution operator that preserves the norm of the wave function.

We use an intensity of $I = 10^{14}$ W/cm^2 ($\Gamma_K \simeq 1$) to compute high-order harmonics while remaining within the tunneling regime using a 800nm laser. We

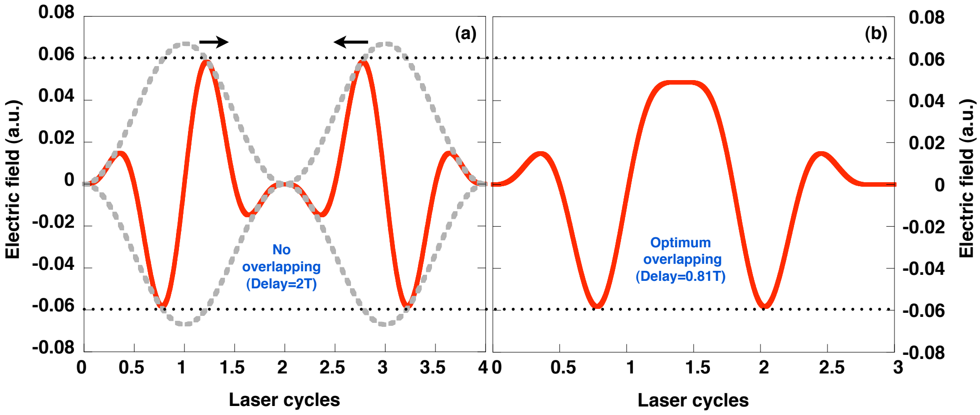

Figure 3.2: Scheme of the pulse synthesis. (a) for the delay $\tau = 2T$ where two pulses do not overlap. (b) Both pulses are overlapped for the delay $\tau \approx \pm 0.81T$ wich is foud optimal for the extension of the harmonic spectrum. Note that the peak amplitude of the resultant field, plotted in (b), is always lower than the maximum amplitude of the input replicas as it is denoted by the horizontal black dotted lines. The pulse envelopes are shown in grey dotted lines which account of the envelope maximum E_0.

plot the results of our calculation in Fig. 3.3. In yellow we show the harmonic spectrum of a single pulse and in green for the doble pulse configuration shown in Fig. 3.2(b). Note that in Fig. 3.2(b) the field amplitude remains always lower than E_0, yet we observe in Fig. 3.3 an extension of the cut-off frequency up to $5.5U_p+I_p$. Therefore the observed extension of the cut-off is not due to the increasing of the field maxima, but to some other process that modifies the electron trajectories, in such a way that the rescatterings become more energetic.

We plot the harmonic spectra obtained for different time delays for the case of pulse lengths N=2 (Fig. 3.4(a)) and N=3 (Fig. 3.4(b)). We can observe two

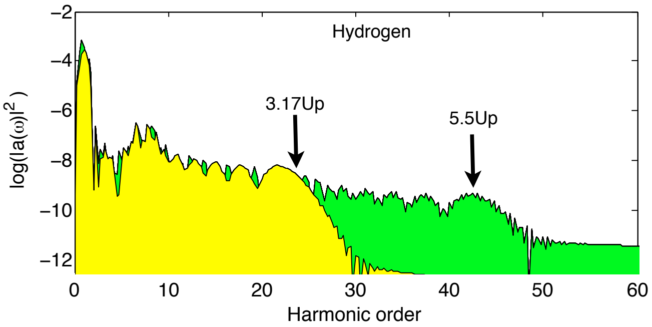

Figure 3.3: 3D TDSE harmonic spectrum in hydrogen at 1.57×10^{14} W/cm^2 for an isolated pulse of $N = 2$ (in yellow) and for the double pulse (in green). A clear extension of the cut-off up to $5.5U_p + I_p$ is observed for the optimum delay $\tau \approx \pm 0.81T$.

peaked structures around $\tau = \pm 0.5T$ corresponding to the maximum overlapping of two replicas. Around $\tau = 0$ the HHG signal drops to zero due to both components of the pulse are dephased by π. The region around $|\tau| \simeq 0.81T$ has a different peak structure, with harmonics extending up to $5.5U_p + I_p$. The peak at $|\tau| \simeq 1.5T$ corresponds to the ordinary extension of the plateau's cut-off due to the increase of the field's intensity, since for this case the overlap of the two replicas is constructive, leading to a maximum field amplitude above E_0 due to constructive interference, therefore, its origin is not related to the mentioned extension, but to the increase of the total fields amplitude, from the constructive interference of both pulses. For longer delays, the pulses no longer overlap and the cut-off frequency is slightly lower than $3.17U_p + I_p$ recovering the results of isolated sin-like pulses.

Therefore, our computations show an abnormal extension of the cut-off for time delays of $\tau = \pm 0.81T$, that does not corresond to an increase of intensity and, therefore, it does not correspond to the standard cut-off law (Eq. (1.13)), valid for isolated pulses. The cut-off will be extended while the peak laser intensity does not exceed the saturation threshold. We must note that the cut-off frequency at time delays $\tau = \pm 0.81T$ cannot be reached for other configurations by simply increasing the intensity of the driving field. This is so, because the intensity needed for the standard cut-off law to reach this photon frequencies falls above the

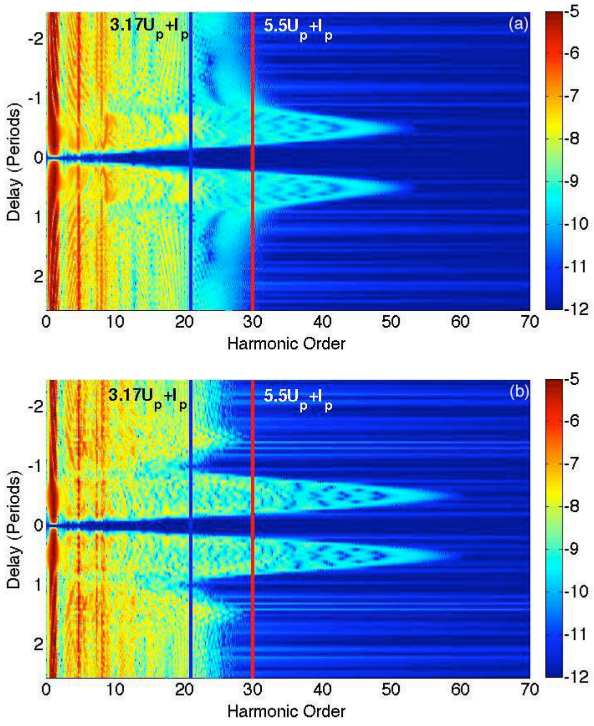

Figure 3.4: Harmonic spectra as a function of delay between the both *sin-like* replicas. (a) For pulses of $N = 2$ cycles and $I = 10^{14}$ W/cm^2. The two maxima at $\tau \approx \pm 0.5T$ are well explained by a the increase of the laser field amplitude, as the two delayed pulses interfere constructively, while at $\tau \approx \pm 0.81T$ the harmonics extend up to $5.5U_p + I_p$ despite the fieldś amplitude remains below E_0. (b) For pulses of $N = 3$ cycles and $I = 10^{14}$ W/cm^2, a similar behaviour is observed, but with optimum extension now around $4.7U_p + I_p$ at $\tau \approx \pm 0.81T$.

saturation and, therefore, the HHG will be severely degraded. As a demonstration of this, in Fig. 3.5 we present the same situation than in Fig. 3.4 but in this case for an intensity of $I = 3.0 \times 10^{14}$ W/cm^2 such that, for hydrogen, each individual pulses are below the single atom saturation threshold but the intensity of the combined pulse with $\tau = \pm 0.5T$ is above the saturation, greatly suppressing the HHG yield.

We find in both cases a clear maximum in the cut-off for delays around $\tau = \pm 0.81T$. In contrast to the previous case, for delays around $\tau = \pm 0.5T$ there is no maxima but rather a sharp drop of the harmonic signal. As in the

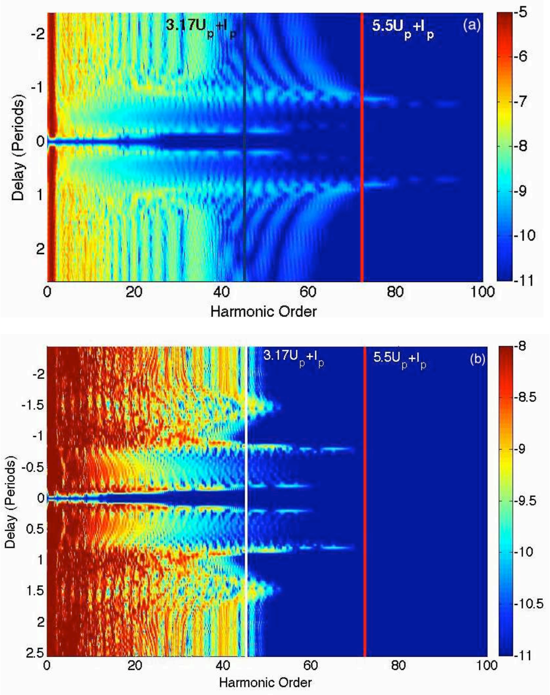

Figure 3.5: The same scheme that in the Fig. 3.4 but in this case in saturation regime. (a) For pulses of $N = 2$ and 3.0×10^{14} W/cm^2, the extension of the cut-off up to $5.5U_p + I_p$ for delays of $\tau \approx \pm 0.81T$ is preserved. The peak at $\tau \approx \pm 0.5T$ that was present at lower intensities is not observed due to the suppression of the harmonic yield at field amplitudes above saturation.(b) For pulses of $N = 3$ and 3.0×10^{14}W/cm^2, a clear, though slightly smaller extension is again observed for delays of $\tau \approx \pm 0.81T$.

previous example, for this delay the resulting field has a higher maxima than E_0, the maxima of each of the pulses, but in this case, that maxima is well into the saturation regime where the harmonic signal drops as previously explained. This is the reason why we only observe harmonics for the delay $\tau = 0.81T$, all other fields higher than E_0 will cause the signal to drop. For the optimal delay, the signal does not drop but rather the cut-off frequency is extended. A close inspection of both panels in Fig. 3.5 shows the set of delays (around $\tau = \pm 0.81T$) where this mechanisms holds. Note that the high frequency structure seen in Fig. 3.5(a) above the $5.5U_P + I_P$ extension is an order of magnitude below the plateau yield so its contribution is not considered relevant to the discussion of the plateau extension. For the case of $N = 3$, the extension is shorter than in the case of $N = 2$, but we still see an extension up to $4.7U_p + I_p$.

Due to the fact that noble gases are the chemical species more commonly used in the HHG experiments, we shall to extend our study to argon atom, exposed to the same laser parameters as used in Fig. 3.3 for hydrogen. For this goal we solve the 3D TDSE for argon using the atomic potential to model this atom reported in [50] and considering the SAE approximation exposed in the previous chapter. In Fig. 3.6 is plotted in panel (a) the HHG for hydrogen and the panel (b) represents the HHG spectrum in argon for identical laser parameters. Note that

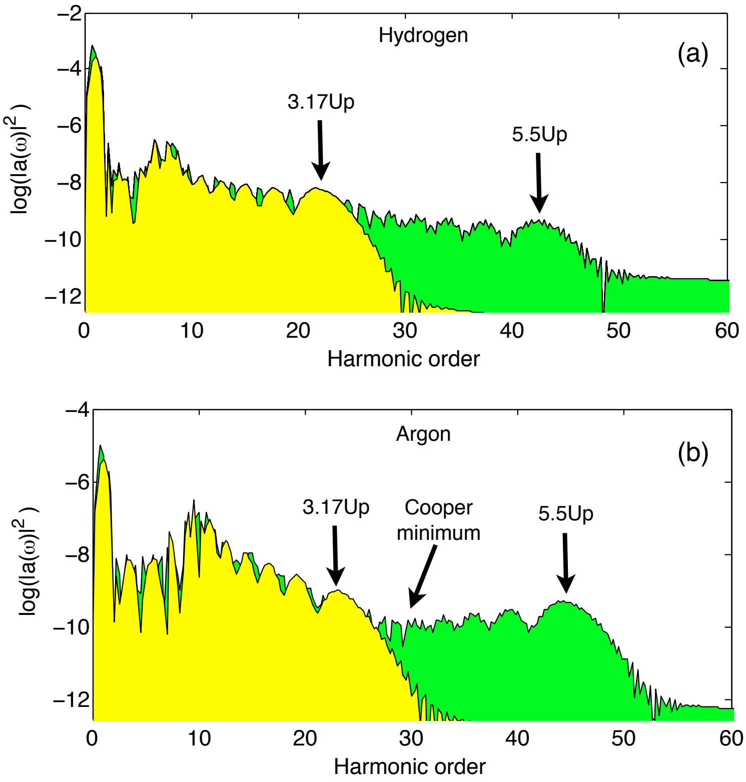

Figure 3.6: 3D TDSE Harmonic spectra at 1.57×10^{14} W/cm^2 for a isolated pulse of $N = 2$ (in yellow) and for the double pulse synthesis (in green). A clear extension of the cut-off up to $5.5U_p + I_p$ is observed for the optimum delay $\tau \approx \pm 0.81T$ in hydrogen (a) and argon (b).

except some peculiarities, such as the Cooper minimum [37, 66, 67] in argon, both spectra presents very similar behavior since both atoms presents similar ionization potentials (-13.6 eV for hydrogen and -15.7 eV for argon). To discuss the exact mechanism producing the extension of the harmonic spectra, we have carried out a time-frequency analysis for the optimum delay $\tau = 0.81T$ and $N = 2$. As commented in chapter 1 this analysis can be used to establish the time instants when the harmonics are produced. Fig. 3.7 shows the HHG spectrum in panel (a) and the wavelet analysis in panel (b) for an intensity of $I = 1.57 \times 10^{14}$ W/cm^2 ($E_0 = 0.067$ a.u.) in hydrogen. We can distinguish three important recollision

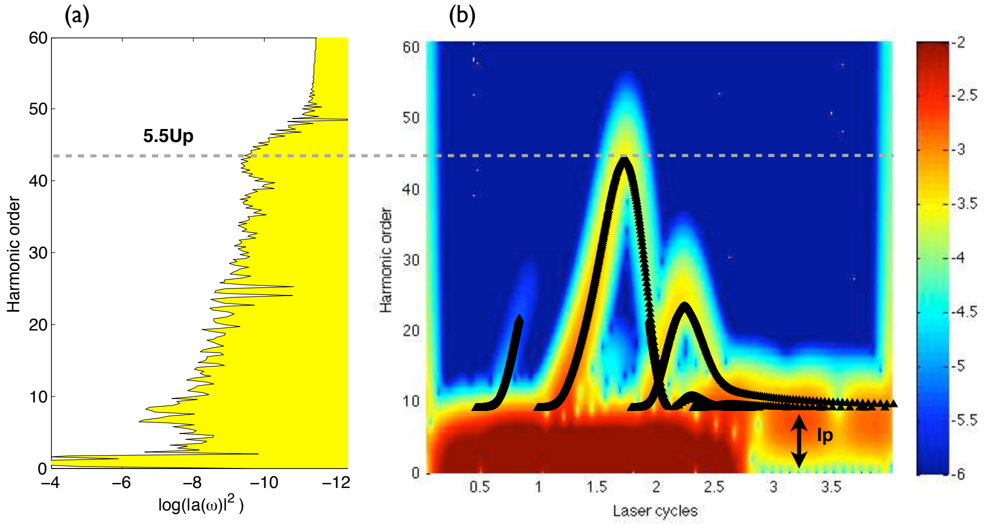

Figure 3.7: Comparison of 3D TDSE harmonic spectra (a) and the corresponding time-frequency analysis (b) resulting from the double pulse synthesis for the optimum parameters ($N = 2$, $\tau \approx \pm 0.81T$) and $I = 1.57 \times 10^{14}$ W/cm^2, 800nm. In the time-frequency analysis (panel (b)) is superimposed as black triangles the values corresponding to the rescattering energies of the various classical trajectories generating the harmonic spectra. Three important emission events are observed. The central event at around $1.75T$ is responsible for the highest harmonics and cut-off extension, whilst other events contribute only to the lower harmonics.

events, the first one correspond to the electrons released at the first field maximum (around $0.35T$) and recombining shortly after the ionization, around $0.87T$, and with a very small amount of energy, leading to low order harmonics. On the other hand, we recognize a last recollision event near the end of the interaction, which is also low energetic and consists on electrons that recollide around $2.25T$ contributing only to low order harmonics.

The most energetic recollisions correspond to electron rescatterings inside the time window from $1.15T$ to $2.1T$. These events produce the high-harmonics well beyond the conventional cut-off limit. The fact that the same conclussion may be reached from the classical trajectories, whose rescattering kinetic energies are superimposed (as black triangles) in Fig. 3.7(b), means that the quantum details of the ionization and recombination have a smaller role in the cut-off extension and justifies the use of classical arguments to understand the mechanism leading to the cut-off extension.

In order to understand the electron dynamics responsible of this unusual cut-off extension, in Fig 3.8 we show the results of the calculation of the kinetic energy at recollision as a function of ionization (grey circles) and recombination (black triangles) time for electrons returning to the origin. Fig. 3.8(a) represents our results for the ordinary sin-like pulse and in Fig. 3.8(c) is plotted the same analysis for the double pulse configuration. In 3.8(b) we plot the corresponding laser fields.

By inspection of Fig. 3.8(c), we can identify again the three relevant recollision events. It becomes clear that the observed extension of the high-harmonic cut-off originates from the central recombination event, in agreement with the wavelet analysis of Fig. 3.7(b). This recollision event corresponds to trajectories which recombine $\approx 1.75T$. Therefore, during the electron's evolution in the continuum the action of the electric field on the electron can be decoupled into three separated sequences (see *e.g.* [56]). As commented in chapter 1, according to the three step model, in the first part of the field, from the time of ionization until the next zero of the field (marked as a point 1 in Fig. 3.8(a) for the isolated sin-like pulse and as a point 3 in Fig. 3.8(c) for the double pulse configuration) the electron is driven away from the core. After that, the sing of the field reverses, decelerating the electron until it is at rest far away from the origin. The kinetic energy of the electron upon recollision is acquired during the final sequence until recombination instant (points 2 and 4 respectively) where the energy is upconverted into the high-harmonic radiation. Fig. 3.8(b) shows that the temporal ionization/recombination window for the case of shaped pulse (delimited by the vertical dotted blue lines) is longer that the corresponding temporal window of the single pulse (delimited by the vertical dotted red lines). The increased range of ionisation times leading to recombination also opens up the temporal window of recollision times. The trajectories originating before the preceding extrema of the field amplitude, at point 3 in Fig. 3.8(c) which would otherwise have not led to recombination are strongly modified to return to the parent ion (point

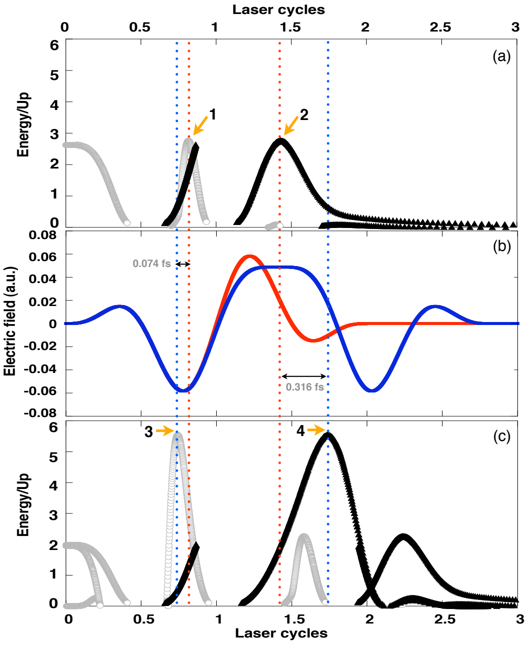

Figure 3.8: (a) Ionization (in grey circles) and recombination energies (in black) resulting from the classical analysis of the isolated sin-like pulse (plotted in red in (b)). (c) similar to (a) but for the case of the double pulse configuration plotted in (b) in solid blue. Points 1 and 2 denote the instant when the electron ionizes and recombines respectively with the maximum energy for the case of isolated sin-like pulse. Points 3 and 4 denote the same for the double pulse synthesis. Note that in the case of double pulse configuration (panel (c)) energies up to $5.5U_p$ are achieved. Note also that in spite of both pulses are identical in the first cycle (see panel (b)) the ionization and recombination events present a temporal shift (see vertical dotted lines) enhancing the ionization-recombination window respect to the isolated pulse.

4 in Fig. 3.8(c)), with a high recollision energy, producing the harmonic cut-off enhancement. Also, the electrons ionized on this manner spend longer time in the continuum, leading to greater spreading of the wavepacket and the associated decrease in the recollision amplitude.

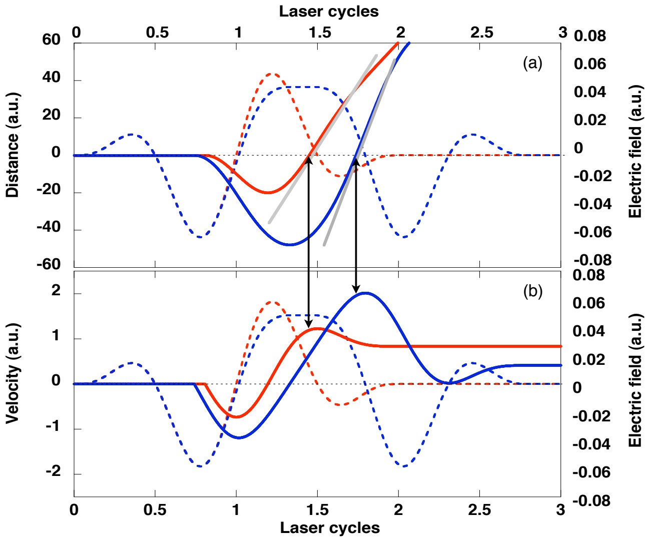

Figure 3.9: Panel (a) shows two different types of electron trajectories corresponding to the maximum energy recombination for the isolated sin-like pulse (in solid red line) and for the double pulse synthesis (in solid blue). Note that the velocity in the recombination instant is different. This fact is denoted (qualitatively) by the respective geometrical tangents plotted in solid grey. Giving the same color criteria, panel (b) quantitative shows the velocity which electron recombines giving the trajectories plotted in (a). The vertical arrows shows the recombination instant in both panels. Note that in the case of the double pulse the recombination velocity (solid blue in (b)) is considerably higher than in the isolated pulse (in solid red). In both panels the laser field amplitudes are plotted in dotted lines, in red for the isolated pulse and in blue for the double pulse configuration.

Conversely, in the case of purely sinusoidal field (Fig. 3.8(a)), the cut-off trajectory is ionised after the field extrema (point 1) and while the field is decreasing, so that the short trajectories are ionised by a lower field. This compensates for the reduction in the recollision amplitude due to the increased wavepacket spreading, in contrast to achieving a comparable cut-off extension through simply increasing the central wavelength. In Fig. 3.9(a) we have selected the classical trajectory which recombines with maximum energy for the isolated sin-like pulse (in red) and for double pulse synthesis (in blue). Comparing both is easy to conclude that this set of trajectories which leads to the highest recollision energy responsible for the harmonic cut-off emission, in the case of the shaped pulse has a duration significantly above the well known monochromatic pulse cut-off trajectory duration $\sim 0.65T$. The tangents shows that electron recombines with higher velocity in the case of shaped pulse that in the case of single pulse. Giving the same color criteria, Fig. 3.9(b) shows the recombination velocity in both cases confirming that in the shaped pulse the electron recombines with velocity considerably higher than in the case of single pulse. In order to explore the limits of this technique with respect to the temporal duration of the driving pulses, in the following we study the double pulse synthesis delaying in time two longer replicas of 4-cycles sin-like

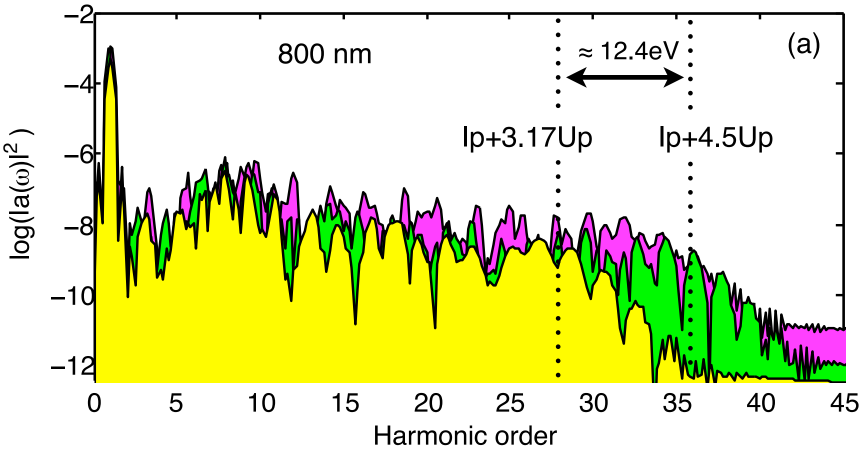

Figure 3.10: 3D TDSE harmonic spectra in hydrogen at $\lambda = 800nm$ resulting from the sin-like isolated pulse of 4 cycles (in yellow) and from the double pulse synthesis for the case of 4 cycles shifted by CEP=π in one of the replicas (in green) and optimum delay τ=1.71 and no shifted (CEP=0) in pink, with delay τ=1.29T. Note that the extension is considerably reduced around $I_p + 4.5Up$. The laser intensity is $I = 1.57 \times 10^{14}$ W/cm^2. Note however that for these longer pulses the CEP is less relevant producing similar extension for the two shaped pulses with different values of the CEP (green and pink spectra).

pulse (N=4) each other. The reason is that the longer pulses makes more realistic the experimental feasibility. In Fig. 3.10 are plotted the 3D TDSE spectra, for a single pulse (in yellow), and for a double pulse configuration, CEP=0 (in pink) and CEP=π (in green). By inspection of this figure we can conclude that in spite of in this case ($N = 4$) the cut-off extension reported, $I_p + 4.5Up$, is lower than for $N = 2$ ($I_p + 5.5Up$) and for $N = 3$ ($I_p + 4.7Up$), however is still important. Also, from Fig. 3.10 is easy to deduce that the CEP is less crucial than in the case of N=2. In the present case both synthesis, CEP=0 and CEP=π provides similar cut-off extensions.

Therefore one should expect that the cut-off extensions reported above turn more relevant if the pulses used for the synthesis are centered in long wavelengths. It is shown in Fig. 3.11 where are represented the HHG spectra in hydrogen using two 4-cycles replicas centered at $\lambda = 1600nm$. Taking into accound that in this case ($N = 4$) the CEP is less relevant, in Fig. 3.11 we only have considered the HHG spectrum for one CEP value, CEP=0 (no shifted). Note that here the cut-off extends up to 49 eV. For pulses with $N > 4$ our simulations reports negligible values for the cut-off extensions.

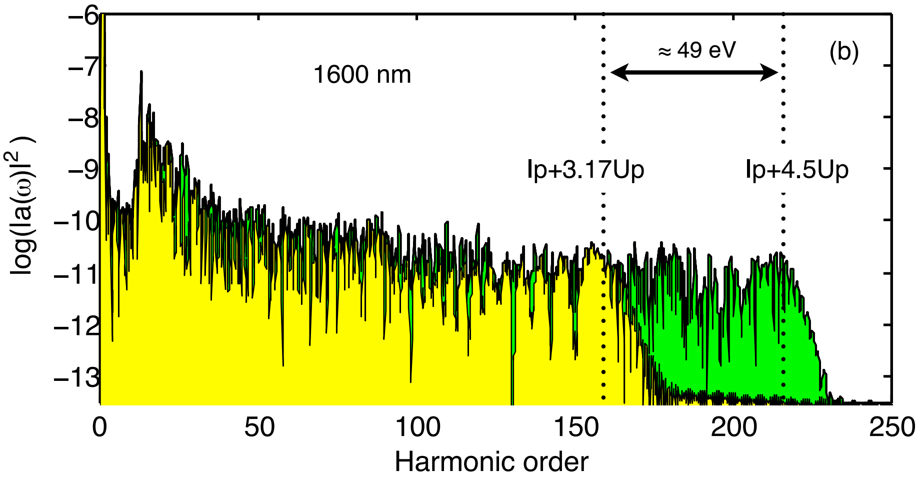

Figure 3.11: Idem that the Fig. 3.10 but in this case at $\lambda = 1600nm$. In the case of the doble pulse synthesis, here only have plotted (in green) the case for CEP=0, i.e. not shifted. Note that here the cut-off increases around $49eV$ according to the $I_p + 4.5Up$ prediction.

To conclude, based on the simulations exposed above, in Fig. 3.12 we have summarized the potentials cut-off extensions can be achieved by double pulse synthesis for N=2 and N=4 in the range from $\lambda = 800$ nm to $\lambda = 1600$ nm in which we have tested by 3D TDSE simulations. However, is possible to extrapolate free of doubts, that for wavelengths beyond $\lambda = 1600$ the cut-off extension also occurs according to the mentioned scaling laws, $I_p + 5.5Up$ and $I_p + 4.5Up$ for N=2 and N=4, respectively.

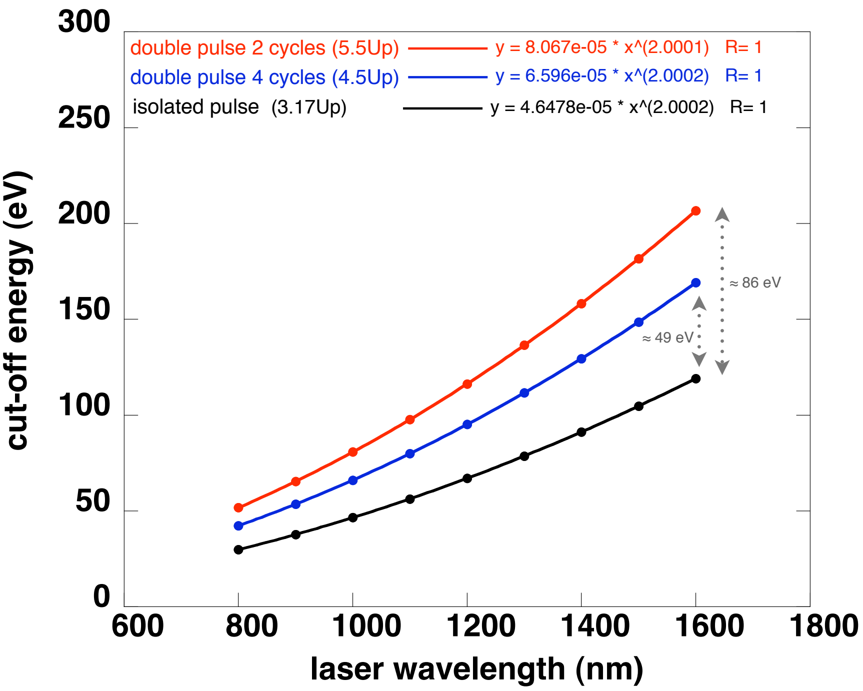

Figure 3.12: Cut-off scaling as a function of the laser wavelength for the double pulse configuration ($N = 2$ in red), for the double pulse configuration ($N = 4$ in blue) and for the isolated sin-like pulse (in black). The laser intensity is 1.57×10^{14} W/cm^2. Note that in order to predict quantitatively the cut-off spectrum in each particular case, the I_p of the corresponding atom must be taken into account.

3.3 Potential applications and conclusions

Let us now consider potential applications. The shaped field leads to a temporal expansion of the ionisation and recombination windows. The most energetic short trajectories are now ionised across the peak of the field, compensating for increased wavepacket spreading and maintaining the high-harmonic yield. In addition, taking advantage of the expanded range of times during which ionised electrons evolve in the continuum, a possible application is the probing of internuclear distance in diatomic molecules provided by the PACER (Probing Attosecond dynamics by Chirp Encoded Recollisions) technique [68]. With the shaped field, the range of excursion times for the short trajectories is expanded to $0.97T$, an increase of $\sim 50\%$ over the case of a single sine-like pulse.

In conclusion, in this section we have presented the possibility of extending the harmonic cut-off using two laser pulses of the same color. The present technique is based on controlling the delay between two CEP-locked ultra-short pulses The novelty of this method relies on that it is not based on the usual approaches, such as chirping and/or mixing different wavelengths to sculpt the input pulse. According to our 3D TDSE simulations the optimal delay found, provides a cut-off extension up to $5.5U_p + I_p$ for $N = 2$ and $4.5U_p + I_p$ for $N = 4$.

One important feature to highlight is that the amplitude of the resultant waveform is lower than the two replicas used for its synthesis. This fact turns quite important when the laser intensity exceeded the threshold of saturation of the target atom. Our analyses have shown that the underlying physics responsible for this extension is the shaping of the electron trajectories to reach higher acquired kinetic energy at rescattering. These kinetic energies reach values enough to generate the cut-off extension, while the whole process remains below the saturation threshold.

We point out that since the form of classical trajectories remains the same, scaling with the laser period, this mechanism works for all range of wavelengths providing the same extensions. In particular, these extension reported above turn important in the case of long wavelength driving lasers, since Up and therefore tha cut-off frequency scales quadratically with λ. Thus, long cut-off extensions can be achieved uniquely constrained by the experimental limitations associated with the manipulation of the ultra-short pulses, and, as long as the intensity and/or wavelength do not rebases the critical values that make important the effect of the magnetic drift, as we shown in chapter 1.

Finally, we highlight that the present technique is focussed only on the temporal synthesis of the interacting laser pulses. It is worth to mention that several works based on both, temporal and spatial synthesis, carried out very recently by Ciappina, the present author and co-workers, suggest the possibility to achieve dramatic cut-off extensions reaching photons in the rage of keV energies from laser pulses centered around $\lambda = 800nm$ [69, 70, 71].

3.4 HHG at ultra-high laser intensities: Non Adiabatic Turn-on driving laser pulses

The increase of laser intensity produces the saturation of atomic ionization. Above this threshold the harmonic efficiency is known to decrease and also the generated plasma affects negatively the phase matching of the harmonic propagation. These limitations seem fundamental and discourages adopting this strategy for the generation of high energetic photons [72]. Note, however, that in spite of the neutral atom is totally depleted, ions, which have higher saturation limits, can become alternative sources of ultra-high order harmonic generation, as demonstrated experimentally in [73]. However, there are potential advantages for considering ultra-high intensities as a method to achieve a plateau of high harmonics. One of these advantages relies on that this approach does not require the development of new intense sources, as the current technology of Ti:Sa amplifiers provides already ultrashort pulses with intensities well above saturation of commonly used targets. Additionally, there are experimental evidences which confirm that ultrashort pulses with intensities above threshold produce phase-locked structureless harmonic spectra, making possible the generation of isolated XUV pulses [74, 75, 76]. This later process will be studied in the next section.

In this section we will explore the possibilities of effciecient HHG in the soft x-ray region, by employing a limiting case of saturation in less of an optical period, during the pulse turn-on. To achieve this regime, tha laser pulses should have a very steep turn-on, and thus are referred as Non-Adiabatic Turn-on (NAT). One practical advantage of NAT pulses is that they have been shown to be less affected by propagation phase matching effects [77]. Also, very recently, the robustness of the single-atom results against propagation for NAT pulses has been also confirmed numerically [76]. According to these results, the main limitation for using ultra-high laser intensities to generate shorter wavelengths would be the degradation of the harmonic efficiency with the intensity in the single-atom response. In the following we will demonstrate that this degradation can be avoided using NAT pulses. In particular, we shall show in the single atom response that it is possible to generate high energetic coherent radiation using intensities around two orders of magnitude above the saturation threshold. At these intensities values, the extension of the cut-off reaches short wavelengths in the soft x-ray region ($\leq 1nm$), reaching the present frontier [55, 79] of high-order harmonic generation. We should highlight that the possibility of generating laser pulses with rapid rising edges has been recently reported in the context of filamentation in molecular aligned gases [80, 81, 82, 83].

3.4.1 Classical analysis

As was exposed in section 1, a qualitative description of high-order harmonic generation can be retrieved by the three step model.

Fig. 3.13 displays the classical energies of recombination for three different pulse envelopes. In Fig. 3.13(a) for a monochromatic field and in Fig. 3.13(b),(c) for two ultrashort pulses (1.5 cycles FWHM) with the same envelope and different CEP, with the explicit form,

$$E(t) = E_0 \sin^2\left(\frac{\omega_0 t}{6}\right) \sin(\omega_0 t + \phi) \tag{3.2}$$

where E_0 is the field amplitude, and ϕ is the CEP. Through the analysis of this figure it is possible to identify that the conventional short and long trajectories are characterized by electrons ionized at the last part of the turn-on and later, i.e. with the most energetic recollisions corresponding to electrons ionized near the field maxima. Note that in the case of $\phi = 0$ (Fig. 3.13(b)) a new kind of trajectories emerges in the turn-on (labeled as a NAT) different from the usual

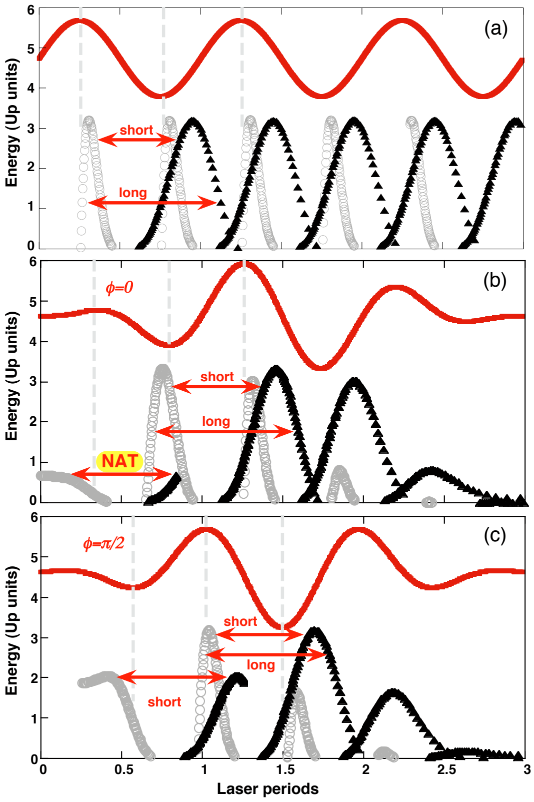

Figure 3.13: Recombination (first rescatering) energies of ionized electrons as a function of the ionization time (grey circles) and recombination time (black triangles), for three different driving laser pulses: (a) constant envelope, and (b) and (c) as described in Eq. (3.2) with (b) $\phi = 0$ and (c) $\phi = \pi/2$. The driving field used in each case is shown in red solid lines. Note that for the case $\phi = 0$ (panel b), a new set of trajectories emerges in the turn-on, labeled as NAT.

long and short. These second class of trajectories, correspond to the electrons ionized during the initial part of the turn on (see Fig. 3.14). Note that this kind of trajectories follow the opposite trend: the most energetic rescatterings originate from electrons ionized almost a quarter cycle before the first field maximum. The emergence of these trajectories is connected with the fast turn-on of the laser pulse, therefore we will refer them as NAT trajectories. Next, as we shall see, this is connected to the decay in efficiency of the radiation generated by the conventional short and long type trajectories. This decay is due to the fast depopulation of the ground state during the excursion of the electron through the continuum. As a result, at the time of rescattering, the ground state is depopulated and the dipole amplitude is small and it results in a lack of efficiency in the HHG produced by long and short types trajectories.

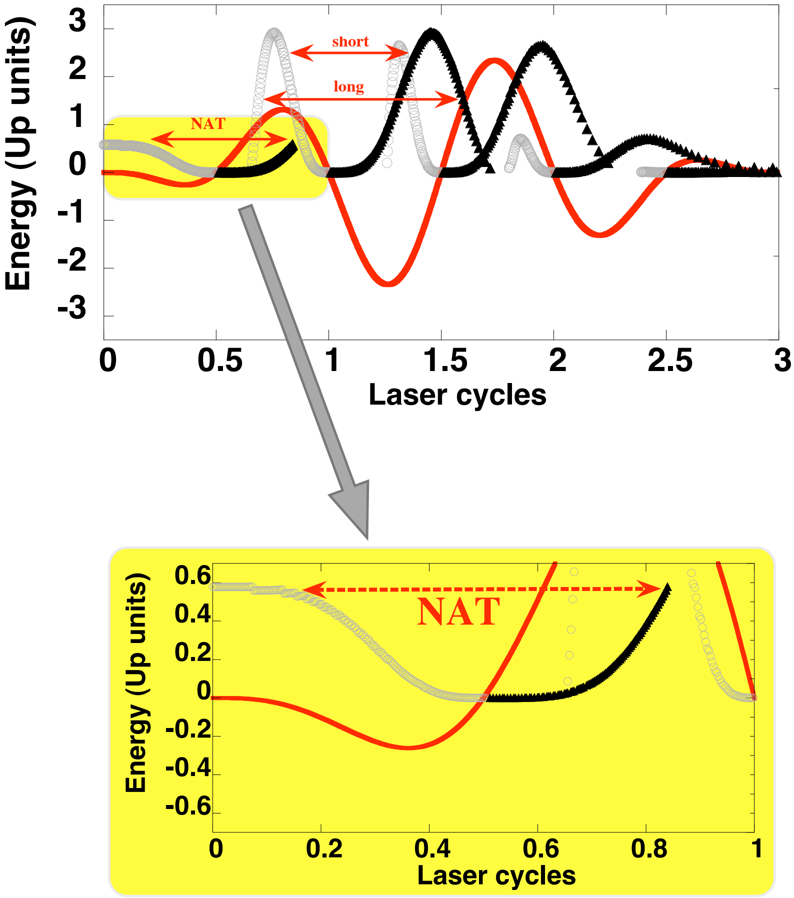

Figure 3.14: A detailed view of Fig. 3.13(b) ($\phi = 0$) in which is highlighted the NAT trajectories emerging in the turn-on. Note that in this case the electrons ionized at the beginning of the laser pulse (in the early turn-on), recombine during the first cycle with energies around $0.5U_p$.

3.4.2 Full quantum description: 3D TDSE quantum analysis

In order to estimate the relative contributions to the harmonic spectrum of the different trajectories let us consider the absolute value of the complex dipole amplitude (assuming constant transition matrix elements)

$$|d(t)| \propto |a_0^*(t)||a_{\mathbf{v}}(t)| \tag{3.3}$$

Where $a_0(t)$ is the probability amplitude of the ground state and $a_{\mathbf{v}}(t)$ is the probability amplitude of the free electron state with velocity v, at the time of rescattering, t. Let us now use for the probability amplitudes that extracted from the results of the exact 3D numerical integration of the time-dependent Schrödinger equation (TDSE): $|a_0(t)|$ is found projecting of the total wavefunction on the ground state, and $|a_v(t)|$ is estimated computing the ground-state depletion during a small time-window around the corresponding ionization time t_0 (i.e. the initial time of the trajectory associated to the rescattering at time t). Specifically

$$|a_v(t)|^2 \simeq \frac{d}{dt}|a_0|^2\bigg|_{t_0} \Delta t \tag{3.4}$$

being Δt a small time interval, whose particular value is not important for the relative comparison between different trajectories, as long as it is kept unchanged. The values of the ionization and rescattering times (t_0 and t) for a particular trajectory are extracted from the classical analysis of Fig. 3.13. This permits us to associate each pair (t_0, t) to a well-defined trajectory, either NAT or long or short type. In order to compare the harmonic efficiency at different laser intensities, we focus on the yield at a fixed harmonic photon energy, W_0.

In Fig. 3.15(a) we plot the results for the yield estimated using Eq. (3.4) corresponding to the recolission energy at the spectral cut-off, for different intensities. Therefore, our procedure will be the following: for each laser intensity, we use Fig. 3.13 to determine the ionization time t_0, and the rescattering time t corresponding to the electronic trajectories with recollision kinetic energy $W_0 - I_p$. We use W_0=73 eV, corresponding to the cut-off energy of the harmonic spectrum in hydrogen at the threshold intensity for saturation [63]. Long and short curves in Fig. 3.15(a) show a descendent behavior with increasing field amplitude, which is connected with the degradation of the harmonic generation by these type of trajectories . The reason behind this can be found in the analysis of the probability amplitudes that conform the dipole transition, as written in Eq. (3.3). Fig. 3.15(b) and Fig. 3.15(c) show the probability amplitudes of the ground and continuum states at rescattering, $|a_0(t)|$ and $|a_v(t)|$. As it is apparent, the decrease in the efficiency of the harmonics radiated by long and short type trajectories is connected with the fast ionization of the ground state for intensities above saturation and, therefore, with the decrease of $|a_0|$. Despite the fact that depletion of the ground state population increases the population of electrons in the continuum, i.e. $|a_\mathbf{v}|$ increases when $|a_\mathbf{0}|$ decreases, the product of both amplitudes has a net decrease and the efficiency of the dipole transition falls. In contrast, for the case of NAT trajectories, the behavior is the opposite:

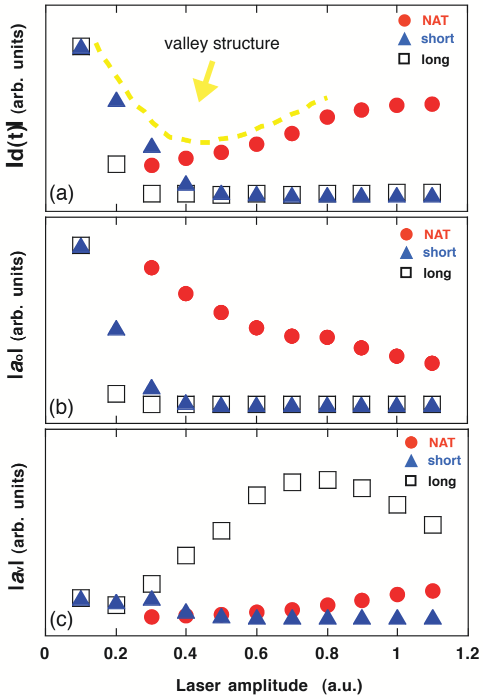

Figure 3.15: Estimations of (a) the relative contributions to the harmonic yield at $W_0 = 73$ eV, (b) the probability amplitude of the ground state, and (c) the corresponding continuum state at the moment of recollision for the sets of trajectories highlighted in Fig. 3.13(b). Contributions of NAT trajectories are shown as red circles, long trajectories as open squares and short as blue triangles. The dashed line in (a) is a sketch of the resulting valley structure for the total radiation yield (sum of the above contributions). The laser amplitudes E are given in atomic units (a.u.), corresponding to intensities $E^2 \times 3.5 \times 10^{16} W/cm^2$.

as they are originated at the first part of the turn-on, the ionization is moderate, even in the case of field amplitudes one order of magnitude above saturation (i.e. intensities two orders of magnitude above saturation). At rescattering, therefore, there is still a significant population in the ground state, and the product of probability amplitudes does not vanish. Therefore, the dipole amplitude is found to increase gradually with the field amplitude. As a result, the global behavior of the harmonic yield with the laser amplitude (Fig. 3.15(a)) follows the form of a valley: First, a decrease connected with the degradation of the efficiency of the short and long trajectories, followed by an increase as the efficiency of the NAT trajectories becomes the relevant contribution to the dipole spectrum. NAT trajectories will eventually be degraded for ultraintense fields well above the atomic unit ($3.5 \times 10^{16}\ W/cm^2$), however for these intensities we should expect also a decay connected with the breaking of the dipole approximation and the associated drift of the electron trajectories away from the ion due to the interaction with the magnetic field [84].

3.4.2.1 Harmonic spectrum

In order to test our analysis, Fig. 3.16 shows the spectra at intensities corresponding to threshold of saturation, saturation and deep saturation regimes, extracted from the exact integration of the 3D TDSE in hydrogen. Below and at the saturation threshold ($I \leq 3.5 \times 10^{14}$ W/cm^2) the increase in laser intensity does not affect strongly the harmonic yield, although it extends the harmonic plateau accordingly to the cut-off law, Eq. 1.13. Above saturation the harmonic yield begins to decrease until a minimum is reached at $I \simeq 5.6 \times 10^{15}$ W/cm^2, corresponding to the bottom of the valley structure sketched in Fig. 3.15(a). For higher intensities the harmonic yield increases as a consequence of the emergence of the contribution of the NAT-type trajectories to the radiation spectrum. Fig. 3.17 represents the full 3D TDSE spectrum for the deep saturation cases for hydrogen. Note that the cut-off exceeds the water window region (in yellow) reaching photon energies in the range of keV according to the estimated cut-off frequency $\simeq I_p + 0.5Up$, associated to NAT trajectories. The potentiality of this technique relies on the possibility to achieve keV photons from driving laser pulses centered in 800nm.

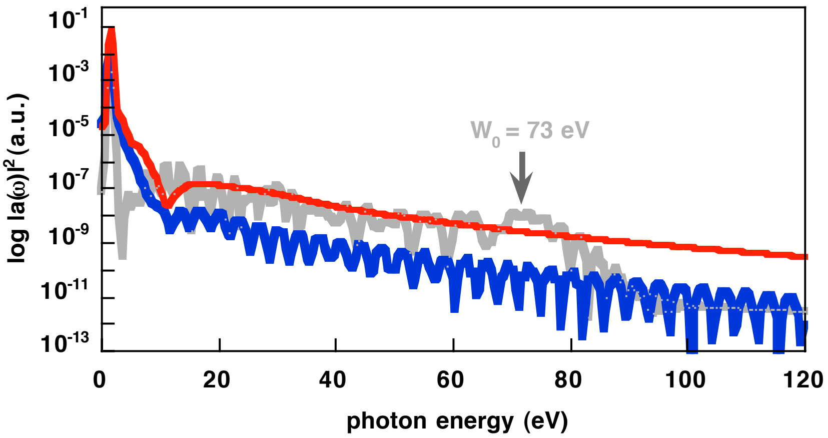

Figure 3.16: Spectra resulting from the exact integration of the 3-dimensional time dependent Schrödinger equation in hydrogen for the laser pulse described in Eq. (3.2) with $\phi = 0$ (Fig. 3.13(b)), for different values of the field intensity: threshold of saturation ($I = 3.5 \times 10^{14}$ W/cm^2, light grey line), saturation ($I = 5.6 \times 10^{15}$ W/cm^2, blue line) and deep saturation ($I = 4.2 \times 10^{16}$ W/cm^2, red line).

In order to study the NAT harmonic emission in the full quantum context we resort again to the time-frequency analysis. In Fig. 3.18 is plotted the time-frequency analysis performed by the wavelet transformation for the three intensity values of the the Fig. 3.16(a), corresponding to the NAT-type pulse plotted in Fig. 3.13(b). In order to compare with the classical predictions we also have superimposed the classical rescattering energies computed from the trajectories labeled in Fig. 3.13(b). By inspection of the three plots of Fig. 3.18 it is easy to see that in the case of threshold of saturation (Fig. 2.11(a)) short and long trajectories are responsible of the harmonic generation. When the intensity exceeds the saturation limit, the harmonic efficiency produced by long and short trajectories is gradually degraded (Fig. 3.18(b)). Note that, at this intensity regime, there are evidences that the NAT trajectories turn important. Fig. 3.18(c) shows the deep saturation case where only NAT trajectories survive due to the atom being completely depleted, except in approximately the first half period of the driving laser pulse. For this reason, short and long trajectories are not involved in the harmonic generation at these high intensity values and obviously there are not interferences between both. According to these results, in deep saturation

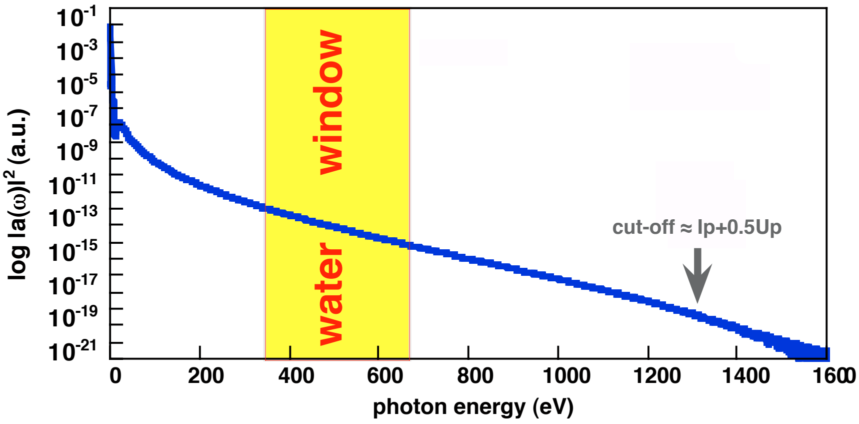

Figure 3.17: Full 3D TDSE spectrum for the deep saturation case in hydrogen. The water window region (283 eV-583 eV) is delimited by the yellow area. The arrow points the estimated cut-off frequency $\simeq I_p + 0.5U_p$, associated to NAT trajectories.

regime, only NAT trajectories are responsible of the harmonic radiation. This is the cause of the absence of modulations in the harmonic spectrum of the deep saturation case plotted in Fig. 3.16 and consequently, it is connected to the fact that the attosecond obtained from the deep saturation spectrum is noise-less and narrow.

Regarding to the behavior with the CEP, when a few cycle input laser pulse as described by Eq. (3.2) is used, the interaction of NAT pulses with matter is strongly dependent on the CEP, ϕ. Therefore, if the CEP of the ultra-short pulse changes from $\phi = 0$ to $\pi/2$ (see Fig. 3.13(c)) the energy diagram for the trajectories radically changes. In this case, the only relevant trajectories for harmonic generation are the conventional short and long type, consequently NAT trajectories are not useful, as the electron excursion is too short to acquire energy relevant for HHG before the total depopulation of the atom. It is also confirmed by the 3D TDSE simulations. However, is important to mention that the NAT-pulses support small CEP fluctuations ($\pm 0.1\pi$ rad) typical from the CEP-stabilized laser source the harmonic efficiency remains almost unaltered as it is shown in Fig. 3.19. This fact makes more realistic the experimental availability.

At this point, is important to mention that results presented above correspond to the single atom calculations. The macroscopic response is not included. The free electron plasma produced by the high ionization degree can induce a strong dephasing. This effect can degrade the macroscopic harmonic yield. On the other hand, there are experimental works [88] that suggest that the effect known as nonadiabatic self phase matching (NSPM) can be used to compensate the dephasing produced by the electron plasma, improving the phase matching. This fact could contribute to the harmonic signal emitted from individual atoms can grow

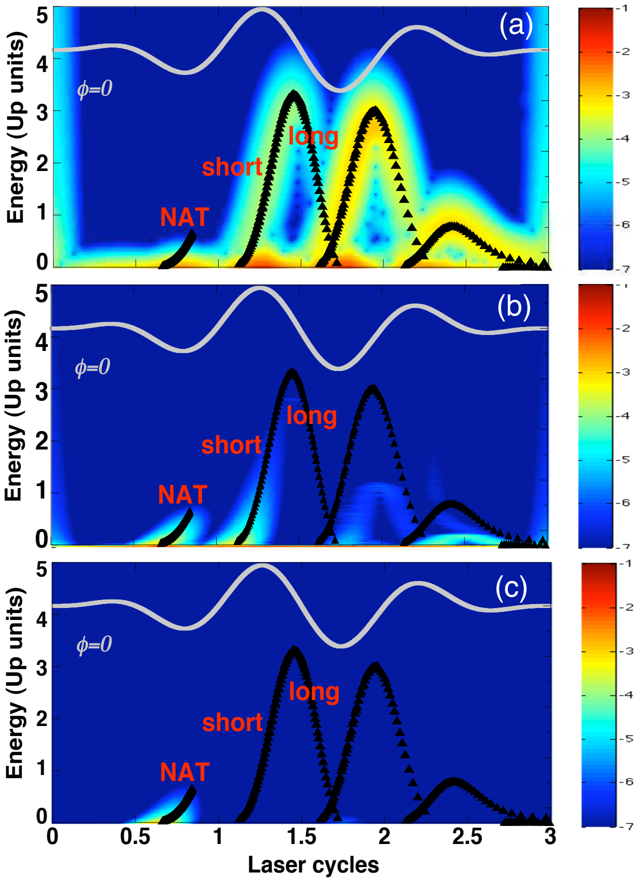

Figure 3.18: Time-frequency analysis of the dipole acceleration extracted from the numerical resolution of 3D TDSE, and (superimposed) classical rescattering energies of electrons as a function of the recombination time (black triangles) for the three laser intensities used in Fig. 3.16 (threshold of saturation ($I = 3.5 \times 10^{14}$ W/cm^2, light grey line), saturation ($I = 5.6 \times 10^{15}$ W/cm^2, blue line) and deep saturation ($I = 4.2 \times 10^{16}$ W/cm^2, red line)).

coherently in the macroscopic interaction medium. However, to include propagation effects via 3D TDSE is, nowadays, computationally intractable. Only SFA and SAF+ approaches provide the way to compute the macroscopic response in a reasonable time of computation. Nevertheless, the laser intensities necessary to the NAT effect emerges are beyond the tunnel regime where, as it is well known, the SFA and SFA+ could provide no reliable predictions.

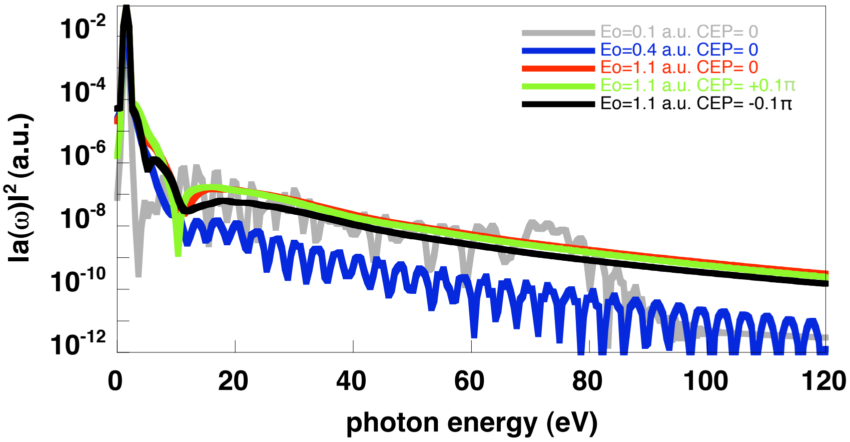

Figure 3.19: The same parameters as in Fig. 3.16 but here including small fluctuations in the CEP in the case of the deep saturation intensity (green, red and black lines). Note that as long as the CEP fluctuations are small ($\pm 0.1\pi$ rad) the harmonic efficiency practically remains unaltered.

3.4.3 Ionization gating with NAT pulses

According to our interpretation, the increase of the yields at ultrahigh intensities is a consequence of the non-adiabatic character of the pulse turn-on. Therefore one should expect that pulses with different shapes and temporal lengths but with similar turn-on will give very similar harmonic spectrum, due to the full ionization of the ground state occurs practically during the first stage of the interaction. To confirm this point, we have performed exact 3D TDSE calculations using a driving pulse with the same turn-on than Eq. (3.2), followed by two cycles of constant amplitude as it is plotted in Fig. 3.20(a). As it is shown in Fig. 3.20(b), for intensities in the deep saturation regime, it is found that the spectrum generated with the longer pulse, plotted in solid blue line in Fig. 3.20(a), overlaps the corresponding spectrum for the short pulse plotted in dotted light grey in the same plot. Note that the ground state depletion is quite similar (practically

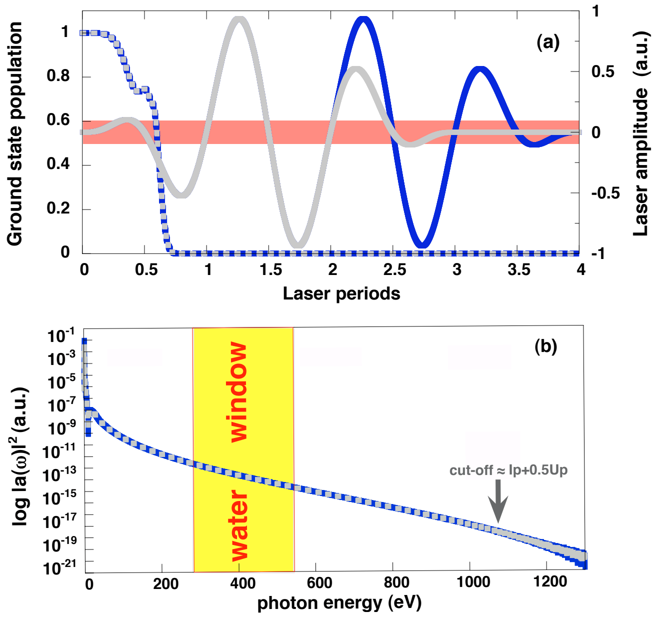

Figure 3.20: (a) NAT-type driving laser pulses with the same turn-on and different length. In solid grey is plotted the pulse described by Eq. (3.2) with $\phi = 0$. In solid blue is ploted a pulse with the same turn-on as that plotted in grey, but now, followed by two cycles of constant amplitude. The dotted grey lines represent the ground state population corresponding to the pulse in solid grey and the dotted blue lines represent the ground state population related to the pulse in solid blue. The horizontal red band delimits the estimated value of the barrier suppression for hydrogen. In (b) are plotted harmonic spectra in hydrogen generated by each one of driving laser pulses plotted in (a). The dotted grey line represents the spectrum generated by the driving laser pulse shown in solid grey in (a). The spectrum drawn in solid blue corresponds to the pulse plotted in solid blue in (a).

both are overlapped), and this fast depletion occurs in the turn-on of the pulse when the barrier suppression intensity (horizontal dashed lines in Fig. 3.20(a)) is exceeded. Therefore, is confirmed that pulse duration is irrelevant, as long as the turn on coincides. As we have shown in section 1.4 the conventional procedure to achieve a single attosecond pulse results from the Fourier synthesis of the higher frequency part of the harmonic plateau. As we will see in the next section one direct consequence of the harmonic spectra generated by NAT pulses is the possibility to synthesize isolated attosecond pulses along the totality of the plateau, including the low order harmonic region, using driving laser pulses with arbitrary temporal duration.

3.5 Attosecond synthesis from NAT pulses

In this section we shall show an approach to attempt the possibility to synthesize intenses isolated attosecond pulses beyond the conventional procedure. Our starting point is the case of NAT laser pulses interacting with a single atom studied in the precedent section.

3.5.1 Harmonic phase extraction

In order to investigate the temporal structure of the extended spectral range generated by NAT pulses, we apply a spectral filter to the high-order harmonic complex dipole acceleration, and then we use an inverse Fourier transform, to obtain the temporal structure of the resulting sub-cycle waveform. In addition, we also calculate the emission time, $t_e = \frac{\partial \phi}{\partial \omega}$, that as commented in section 1.4 account for the degree of synchronization of the harmonics during the emission process. In Fig. 3.21 is plotted the HHG spectra (in red) generated by NAT pulse and the corresponding emission times (in blue) in the two different regimes, threshold of saturation in panel (a) and and deep saturation in panel (b), for hydrogen. Note the different behaviour of the emission times between both regimes. In the case of deep saturation (panel (b)), the slope of the emission times is almost plane along the totality of the plateau. This fact allows to select a large bandwidth along the harmonic spectrum due to almost the totality of the plateau presents absence of modulations. Consequently, it makes to suspect that a single, narrow and intense attosecond pulse can be achieved. Fig. 3.22 shows the spectral filtering in hydrogen for the two intensity regimes of Fig. 3.21. We have simulated a high-pass filter similar to a metallic Zirconium filter. Note that the absence of modulations that the spectra generated by NAT-pulse presents allows to use a wide zone from the low order harmonics. Note also that we put the limit of the filter in the same point (around 47 eV) in both cases in Fig. 3.22. On the contrary, in a standard harmonic spectrum generated by the interference of long and short trajectories, only is possible to achieve an isolated attosecond pulse as long as the filter is located close to the cut-off. This fact confirms that in deep saturation practically all harmonics are generated simultaneously by an unique event governed by the NAT trajectories. We stress that the fluctuations of the emission times in the final part of the spectra in Fig. 3.21 correspond to numerical

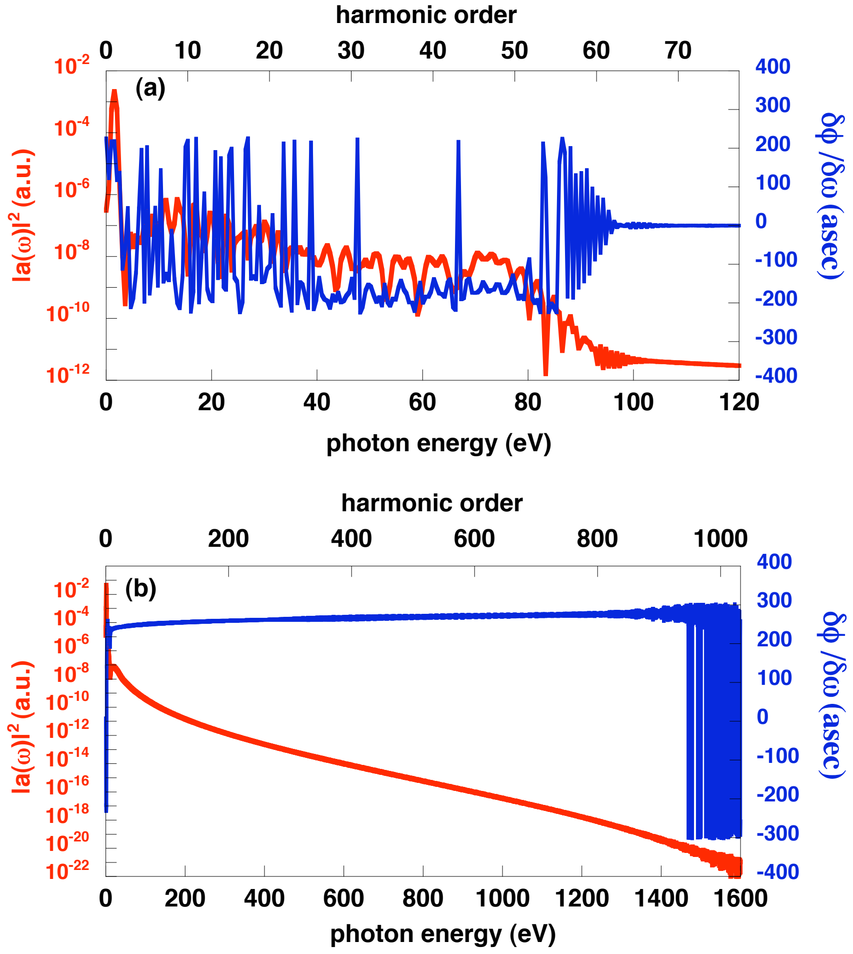

Figure 3.21: HHG spectra (in red) generated by NAT pulses and the corresponding emission times (in blue) for the threshold of saturation intensity (a) and deep saturation (b).

noise caused by the rapid oscillations that the dipole acceleration presents at the end of the cut-off. However, from the physical viewpoint, this fact is irrelevant and does not affect to the physical information reported in the plot.

By inspection of Fig. 3.22 is easy to conclude that the attosecond synthesized in the case of deep saturation (panel (d)) is narrower and cleaner that in the case of threshold of saturation (panel (c)). Note also that in deep saturation the attosecond is more intense, which agrees with the fact of a large spectral bandwidth is selected covering almost the totality of the harmonic plateau (from 47 eV to the cut-off). The insets (plots (e) and (f)) in Fig. 3.22 show, in detail, the

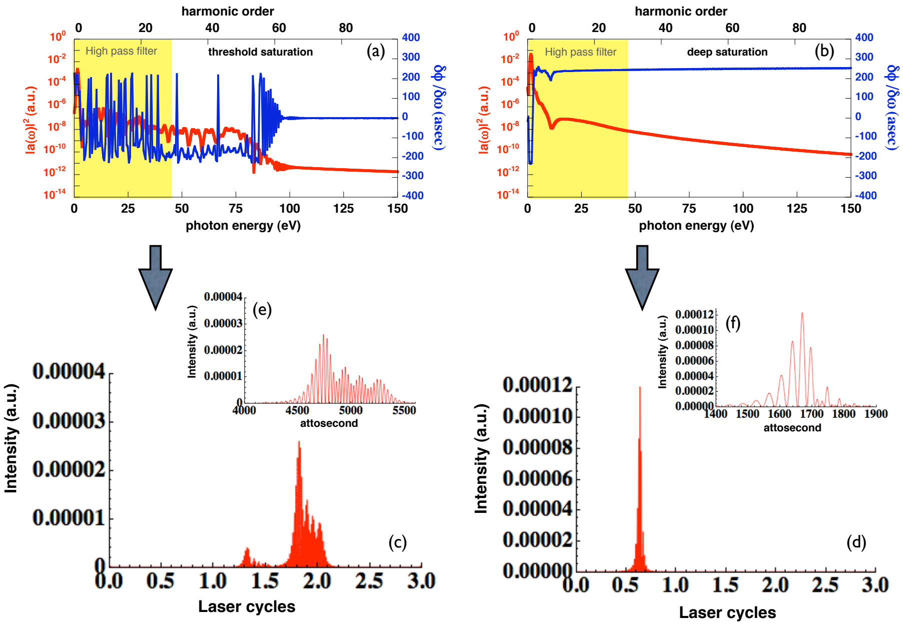

Figure 3.22: Temporal synthesis from HHG spectra in hydrogen. Plot (a) represents the HHG spectrum in threshold of ionization and plot (b) represents the deep saturation regime generated by NAT pulses (for the same parameters that in Fig. 3.20(b)). In both the HHG spectra are ploted in solid red line and the ionization times are ploted in solid blue line. The yellow area delimits the high-pass filter used (note that is identical in both cases, from 0 to 30st harmonic order). Plots (c) and (d) shows the corresponding sub-femtosecond temporal structures, respectively. The respective insets, (e) and (f), represent the zoom of these temporal structures. Note that the x-axes in the insets have been changed to attosecond units.

temporal structure and duration of the respective attosecond pulses.

To conclude, Fig. 3.23(a) shows the spectral filtering moving the high-pass filter

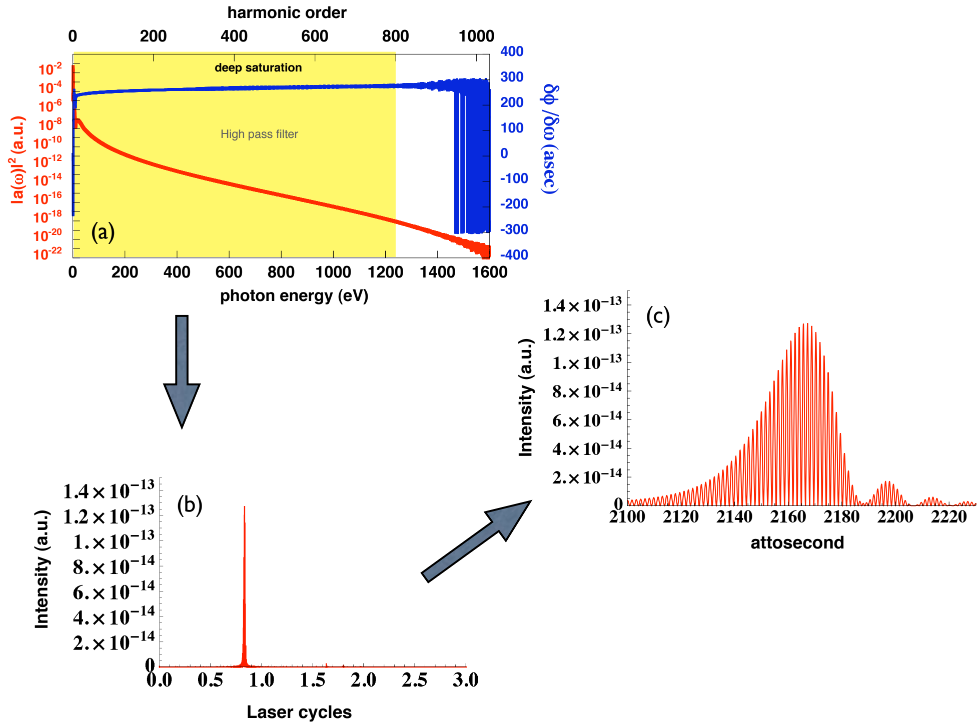

Figure 3.23: Temporal synthesis in the deep saturation regime for hydrogen (the parameters are the same of Fig. 3.20(b)). In this case the high pass filter used (in yellow) covers a wide zone in the harmonic spectrum (from 0 to 800st harmonic order). Note also that here the attosecond waveform is very narrow (see inset (c)) comparing with the cases of Fig. 3.22(d-f). Note, however that the attosecond intensity in this case drops orders of magnitude.

close to the cut-off zone in deep saturation and the corresponding attosecond pulse (panel (b)). In this case can be observed that the attosecond is very narrow (about 40 attoseconds FWHM the most intense, and the others substructures located in the tail its duration reach the subattosecond frontier (see panel (c))) in comparison with the case studied above, where the high-pass filter is located in the low harmonic order. However, note that in the present case the attosecond intensity falls orders of magnitude below the intensity of the attosecond synthesized in Fig. 3.22(d).

Summarizing, in this section it has been theoretically demonstrated that NAT-type input laser pulses are particularly resistant to the effects of saturation and, therefore, may play a fundamental role in harmonic generation with ultraintense fields.

Finally, it is worth stressing that the study presented in this chapter together with the results published in [53], constitute, as far as we know, the first theoretical work in the literature focussed on the identification of the physical mechanism responsible of this unusual growing of the harmonic yield that occurs, under particular conditions studied above, when the laser intensity is increased beyond this saturation limit. The potential of this technique relies on the possibility to achieve high energy photons, reaching values in the range of keV, using driving laser pulses centered at 800nm. This is the wavelength that nowadays provides the conventional laser sources based on CPA technology. Also it is worth to mention the possibility to synthesize intense and narrow intense attosecond pulses from NAT-laser pulses with arbitrary temporal duration. For the reasons mentioned above, it is reasonable to suggest that a research line on this direction deserves be carried out further.

4

Conclusions

> *" Science cannot solve the ultimate mystery of nature. And that is because, in the last analysis, we ourselves are a part of the mystery that we are trying to solve "*
>
> *Max Karl Ernest Ludwig Planck*

In summary, along this thesis has been carried out a theoretical investigation of the high order harmonic generation process beyond standard procedure. In the first part, we have developed a compact extension of the standard SFA, the SFA+. The two main novel aspects in which the SFA+ is based, consist of on one hand, to take into account the interaction of the electromagnetic field with the atomic ground state and, on the other hand, in not using the saddle point approximation, providing a fully quantum (not semiclassical) description. Our results have been tested against the 3D TDSE in a wide range of parameters with positive results. On this manner SFA+ is proven to be quantitative accurate in the description of the higher frequency part of the harmonic spectra, not only in tunnel, also in the multiphoton regime. Also SFA+ provides physical insights the contribution to the total acceleration spectrum of the different momentum components. In addition, two additional radiative processes to the conventional semiclassical electron rescattering, named *way-out* and *close-up*, are also identified. These mechanisms of radiation are demonstrated to be irrelevant in the qualitative understanding of the generation of the higher harmonics in the tunneling case, but not in the multiphoton regime. We also shown the successful applicability of the SFA+ to species different from hydrogen, such as helium. The potential extension of the SFA+ to study of simple molecules constitutes an open research line.

In the second part of this thesis we have investigated two new routes to achieve high energy photons via HHG. Our first method consists on to extend the harmonic cut-off sculpting the driving laser pulse delaying in time two pulse replicas. As we have shown, superposing these two replicas later, with an optimum delay between both, the resulting driving laser waveform is capable to produce dramatic cut-off extensions up to $I_p + 5.5Up$. The potentiality that this technique presents at long laser wavelengths has also been investigated.

Our second proposal emerges from the study the HHG process at high laser intensity, exceeding the saturation limit of the atomic target. In this context a detailed study carried out of the intra-cycle electron dynamics during the pulse turn-on together with the full quantum analysis reports, as a main result, that the loss of efficiency caused by the saturation effects can be compensated. Our numerical simulations predicts that coherent radiation beyond the water window could be achieved using particular interacting laser pulses, which we have denoted as *NAT* pulses, centered at $800nm$. In addition, we have demonstrate theoretically that NAT-type pulses provides a direct route to achieve a broad isolated and intense attosecond pulse. However, we take in mind that the experimental confirmation of this prediction still remains a challenge.

Appendix A

Derivation I

A.1 From Eqs.(2.4),(2.5) to Eqs.(2.8),(2.9), respectively

Substituting Eqs.(2.4) and (2.5) in Eq (2.6),

$$
\begin{aligned}
\langle\psi(t)|\hat{Q}\hat{a}\hat{P}|\psi(t)\rangle &= \left[\langle\phi_0|G_a^-(t_0,t)+\frac{1}{\hbar}\int_{t_0}^{t}\langle\phi_0|G_a^-(t_0,t_1)\hat{Q}V_i(t_1)\hat{Q}G^-(t_1,t)\hat{Q}dt_1\right]\hat{a} \\
&\quad \left[\frac{1}{\hbar}\int_{t_0}^{t}\hat{P}G^+(t,t_1)\hat{P}V_i(t_1)\hat{Q}G_a^+(t_1,t_0)|\phi_0\rangle dt_1\right] \\
&= \frac{1}{\hbar}\int_{t_0}^{t}\langle\phi_0|G_a^-(t_0,t)\hat{a}\hat{P}G^+(t,t_1)\hat{P}V_i(t_1)\hat{Q}G_a^+(t_1,t_0)|\phi_0\rangle dt_1 \\
&+ \frac{1}{\hbar^2}\int_{t_0}^{t}dt_2\langle\phi_0|G_a^-(t_0,t_2)\hat{Q}V_i(t_2)\hat{Q}G^-(t_2,t)\hat{Q}\hat{a} \\
&\quad \int_{t_0}^{t}\hat{P}G^+(t,t_1)\hat{P}V_i(t_1)\hat{Q}G_a^+(t_1,t_0)|\phi_0\rangle dt_1
\end{aligned}
\tag{A.1}
$$

Note that the first term in Eq. (A.1) corresponds to Eq. (2.8). In the following we will show the algebraic process to arrive to Eq. (2.9) from the last term in

Appendix A: From Eqs.(2.4),(2.5) to Eqs.(2.8),(2.9)

Eq. (A.1),

$$\begin{aligned}
& \frac{1}{\hbar^2}\int_{t_0}^{t} dt_2 \langle\phi_0|G_a^-(t_0,t_2)\hat{Q}V_i(t_2)\hat{Q}G^-(t_2,t)\hat{Q}\hat{a} \\
& \int_{t_0}^{t} \hat{P}G^+(t,t_1)\hat{P}V_i(t_1)\hat{Q}G_a^+(t_1,t_0)|\phi_0\rangle dt_1 \\
= & \frac{1}{\hbar^2}\int_{t_0}^{t}\int_{t_0}^{t} dt_2 dt_1 \langle\phi_0|G_a^-(t_0,t_2)\hat{Q}V_i(t_2)\hat{Q}G^-(t_2,t)\hat{Q}\hat{a} \\
& \hat{P}G^+(t,t_1)\hat{P}V_i(t_1)\hat{Q}G_a^+(t_1,t_0)|\phi_0\rangle \qquad (A.2)
\end{aligned}$$

and considering the identity,

$$\int_{t_0}^{t}\int_{t_0}^{t} dt_2 dt_1 f(t_2,t_1) = \int_{t_0}^{t} dt_2 \int_{t_0}^{t_2} dt_1 f(t_2,t_1) + \int_{t_0}^{t} dt_1 \int_{t_0}^{t_1} dt_2 f(t_2,t_1) \qquad (A.3)$$

we can write,

$$\begin{aligned}
& \frac{1}{\hbar^2}\int_{t_0}^{t}\int_{t_0}^{t} dt_1 dt_2 \langle\phi_0|G_a^-(t_0,t_2)\hat{Q}V_i(t_2)\hat{Q}G^-(t_2,t)\hat{Q}\hat{a} \\
& \hat{P}G^+(t,t_1)\hat{P}V_i(t_1)\hat{Q}G_a^+(t_1,t_0)|\phi_0\rangle \\
= & \frac{1}{\hbar^2}\int_{t_0}^{t} dt_2 \int_{t_0}^{t_2} dt_1 \langle\phi_0|G_a^-(t_0,t_2)\hat{Q}V_i(t_2)\hat{Q}G^-(t_2,t)\hat{Q}\hat{a} \\
& \hat{P}G^+(t,t_1)\hat{P}V_i(t_1)\hat{Q}G_a^+(t_1,t_0)|\phi_0\rangle \\
+ & \frac{1}{\hbar^2}\int_{t_0}^{t} dt_1 \int_{t_0}^{t_1} dt_2 \langle\phi_0|G_a^-(t_0,t_2)\hat{Q}V_i(t_2)\hat{Q}G^-(t_2,t)\hat{Q}\hat{a} \\
& \hat{P}G^+(t,t_1)\hat{P}V_i(t_1)\hat{Q}G_a^+(t_1,t_0)|\phi_0\rangle \\
& \equiv I_1 + I_2^\dagger \qquad (A.4)
\end{aligned}$$

where,

$$\begin{aligned}
I_2 \equiv & \frac{1}{\hbar^2}\int_{t_0}^{t} dt_1 \int_{t_0}^{t_1} dt_2 \langle\phi_0|G_a^-(t_0,t_1)\hat{Q}V_i(t_1)\hat{P}G^-(t_1,t)\hat{P}\hat{a} \\
& \hat{Q}G^+(t,t_2)\hat{Q}V_i(t_2)\hat{Q}G_a^+(t_2,t_0)|\phi_0\rangle \qquad (A.5)
\end{aligned}$$

interchanging t_2 and t_1,

$$\begin{aligned}
I_2 \equiv & \frac{1}{\hbar^2}\int_{t_0}^{t} dt_2 \int_{t_0}^{t_2} dt_1 \langle\phi_0|G_a^-(t_0,t_2)\hat{Q}V_i(t_2)\hat{P}G^-(t_2,t)\hat{P}\hat{a} \\
& \hat{Q}G^+(t,t_1)\hat{Q}V_i(t_1)\hat{Q}G_a^+(t_1,t_0)|\phi_0\rangle \qquad (A.6)
\end{aligned}$$

I_2 represents a process in which the state in $t_2 > t_1$ is more energetic than in t_1. In others words, this term represents the absorption of photons by the harmonic field. On this manner we arrive to the Eq. (2.9),

$$\begin{aligned} a_d(t) = I_2 \;\; &= \;\; \frac{1}{\hbar^2}\int_{t_0}^{t} dt_2 \int_{t_0}^{t_2} dt_1 \langle\phi_0|G_a^{-}(t_0,t_2)\hat{Q}V_i(t_2)\hat{Q}G^{-}(t_2,t)\hat{Q}\hat{a} \\ & \quad\;\; \hat{P}G^{+}(t,t_1)\hat{P}V_i(t_1)\hat{Q}G_a^{+}(t_1,t_0)|\phi_0\rangle \end{aligned} \tag{A.7}$$

Appendix A: From Eqs.(2.4),(2.5) to Eqs.(2.8),(2.9)

Appendix B

Derivation II

B.1 From Eqs.(2.8),(2.9) to Eq. (2.14)

Starting from Eq. (2.8) and including the identity $\int d\mathbf{k}|\mathbf{k}\rangle\langle\mathbf{k}| \equiv 1$,

$$\begin{aligned}
a_b(t) &= \frac{1}{\hbar}\int_{t_0}^{t}\langle\phi_0|G_a^-(t_0,t)\hat{a}\left[\int d\mathbf{k}|\mathbf{k}\rangle\langle\mathbf{k}|\right]\hat{P}G^+(t,t_1)\hat{P}V_i(t_1)\hat{Q}G_a^+(t_1,t_0)|\phi_0\rangle dt_1 \\
&= \int d\mathbf{k}\frac{1}{\hbar}\int_{t_0}^{t}\langle\phi_0|G_a^-(t_0,t)\hat{a}|\mathbf{k}\rangle\langle\mathbf{k}|\hat{P}G^+(t,t_1)\hat{P}V_i(t_1)\hat{Q}G_a^+(t_1,t_0)|\phi_0\rangle dt_1 \\
&= \int d\mathbf{k}\frac{1}{\hbar}\int_{t_0}^{t}\langle\phi_0|G_a^-(t_0,t)\hat{a}|\mathbf{k}\rangle\langle\mathbf{k}|G^+(t,t_1)|\mathbf{k}\rangle\langle\mathbf{k}|V_i(t_1)\frac{C_F}{r^n}G_a^+(t_1,t_0)|\phi_0\rangle dt_1 \\
&= \int d\mathbf{k}\left[-\frac{i}{\hbar}C_F\int_{t_0}^{t}dt_1 e^{i\epsilon_0(t-t_1)/\hbar}e^{-i\frac{1}{\hbar}\int_{t_1}^{t}\epsilon(\mathbf{k},\tau)d\tau}\langle\phi_0|\hat{a}|\mathbf{k}\rangle V_i(\mathbf{k},t_1)\langle\mathbf{k}|r^{-n}|\phi_0\rangle\right] \\
&= \int d\mathbf{k}a_b(\mathbf{k},t) \qquad\qquad \text{(B.1)}
\end{aligned}$$

Appendix B: From Eqs.(2.8),(2.9) to Eq. (2.14)

Appendix C

Derivation III

C.1 Wavepacked spreading: Derivation of Eq. (2.17)

Here we will calculate the spreading of the wavepacked during the excursion time $3T/4$. The electron kinetic energy in the ground state is $K = |\epsilon_0| = 1/2mv^2$. Consequently $v = \sqrt{\frac{2|\epsilon_0|}{m}}$ and the wavepacked spreads as,

$$\Delta x = v\frac{3}{4}T = \frac{3}{4}T\sqrt{\frac{2|\epsilon_0|}{m}} = \frac{3}{4}\frac{2\pi}{\omega_0}\sqrt{\frac{2|\epsilon_0|}{m}} = \frac{3\pi}{2\omega_0}\sqrt{\frac{2|\epsilon_0|}{m}} \tag{C.1}$$

According to the semiclassical model, during the rescattering, the electron energy is $K = 3.17U_p$. On this manner, the rescattering velocity $v_r = \sqrt{\frac{2(3.17U_p)}{m}}$ and the time spending by the wavepacket at the recombination in the origin is,

$$\delta_s = \frac{\Delta x}{v_r} = \frac{\frac{3\pi}{2\omega_0}\sqrt{\frac{2|\epsilon_0|}{m}}}{\sqrt{\frac{\sqrt{2(3.17U_p)}}{m}}} = \frac{3\pi}{2\omega_0}\sqrt{\frac{|\epsilon_0|}{3.17U_p}} \tag{C.2}$$

Appendix C: Wavepacked spreading: Derivation of Eq. (2.17)

Appendix D

Derivation IV

D.1 Derivation of the level shift (Eq. (2.18)).

Eq. (2.18) represents the energy shift which is evaluated as the time average of the interaction $V_i(\tau)$ over the collision time, δt_s,

$$\langle V_i(t)\rangle = (1/\delta t_s)\int_{t-\delta t_s}^{t}\left[-(q\hbar/mc)A(\tau)k_z + (q^2/2mc^2)A^2(\tau)\right]d\tau \tag{D.1}$$

where k_z is a relevant momentum of the state (Eq. (2.19)). Assuming a monochromatic field,

$$A(t) = \frac{E_0}{\omega_0}cos(\omega_0 t) = (2c/q)\sqrt{mU_p}cos(\omega_0 t + \phi) \tag{D.2}$$

and for the particular times when the higher energy rescattering takes place (field near 0, i.e. $(\omega_0 t + \phi) \simeq n\pi$), we find $\langle cos(\omega_0 t + \phi)\rangle \simeq sin(\omega_0 \delta t_s)/\omega_0 \delta t_s$ and $\langle cos^2(\omega_0 t + \phi)\rangle \simeq 1/2 + sin(2\omega_0 \delta t_s)/4\omega_0 \delta t_s$, therefore,

$$\Delta t_s \simeq U_p + \frac{2\hbar}{\omega_0 \delta t_s}\sqrt{\frac{U_p}{m}}k_z sin(\omega_0 \delta t_s) + \frac{U_p}{2\omega_0 \delta t_s}sin(2\omega_0 \delta t_s) \tag{D.3}$$

Starting from

$$\begin{aligned}
&\frac{1}{\delta t_s}\Big(-\frac{q\hbar}{mc}\Big)k_z\int_{t-\delta t_s}^{t}A(\tau)d\tau = \frac{1}{\delta t_s}\Big(-\frac{q\hbar}{mc}\Big)k_z\frac{2c}{|q|}\sqrt{mU_p}\int_{t-\delta t_s}^{t}cos(\omega_0\tau)d\tau\\
= \ &\frac{1}{\delta t_s}\Big(-\frac{q\hbar}{mc}\Big)k_z\frac{2c}{|q|}\sqrt{mU_p}\frac{1}{\omega_0}\big[sin(\omega_0\tau)\big]_{t-\delta t_s}^{t}\\
= \ &-sign(q)\frac{2\hbar}{\omega_0\delta t_s}k_z\sqrt{\frac{U_p}{m}}\big[sin(\omega_0 t)-sin(\omega_0(t-\delta t_s))\big]\\
= \ &-sign(q)\frac{2\hbar}{\omega_0\delta t_s}k_z\sqrt{\frac{U_p}{m}}\big[sin(\omega_0 t)-sin(\omega_0 t)cos(\omega_0\delta t_s)-cos(\omega_0 t)sin(\omega_0\delta t_s)\big]\\
&\approx -sign(q)\frac{2\hbar}{\omega_0\delta t_s}k_z\sqrt{\frac{U_p}{m}}sin(\omega_0\delta t) \qquad \text{(D.4)}
\end{aligned}$$

Consequently,

$$\begin{aligned}
&\frac{q^2}{2mc^2}\frac{4c^2}{|q|^2}mU_p\frac{1}{\delta t_s}\int_{t-\delta t_s}^{t}cos^2(\omega_0\tau)\\
= \ &\frac{q^2}{2mc^2}\frac{4c^2}{|q|^2}mU_p\frac{1}{2}+\frac{q^2}{2mc^2}\frac{4c^2}{|q|^2}mU_p\frac{1}{2\delta t_s}\int_{t-\delta t_s}^{t}cos(2\omega_0\tau)\\
= \ &U_p+\frac{U_p}{2\omega_0\delta t_s}\big[sin(2\omega_0\tau)\big]_{t-\delta t_s}^{t}\approx U_p+\frac{U_p}{2\omega_0\delta t_s}sin(2\omega_0\delta t_s) \qquad \text{(D.5)}
\end{aligned}$$

where t is assumed as an instant of recolision and for this reason we can approximate $sin(\omega_0 t)\approx 0$

Appendix E

Derivation V

E.1 Derivation of Eq. (2.19)

Computing the expectation value of the hamiltonian in the ground state,

$$\Big\langle H(t) \Big\rangle_{|\phi_0\rangle} = \epsilon_0 \Big\langle \frac{-q\hbar}{mc} Ap \Big\rangle + \Big\langle \frac{q^2}{2mc^2} A^2 \Big\rangle = \epsilon_0 + 2U_p cos^2(\omega_0 t) \tag{E.1}$$

Assuming the virial theorem, for the hydrogen atom the kinetic energy in absence of field is $K = -\epsilon_0$. When the field is present the kinetic energy is $K = -\epsilon_0 + 2U_p cos^2(\omega_0 t)$,

$$\frac{1}{2m}\Big(\hbar k_z - 2sign(q)\sqrt{mU_p} cos(\omega_0 t)\Big)^2 + K_x + K_y = -\epsilon_0 + 2U_p cos^2(\omega_0 t) \tag{E.2}$$

where K_x and K_y represent the kinetic energies corresponding to the transverse coordinates. Assuming the equipartition principle, the total energy for each other is,

$$H_{x,y} = \frac{1}{3}\big(\epsilon_0 + 2U_p cos^(\omega_0 t)\big) \tag{E.3}$$

According to the virial theorem and considering that the transverse perturbations are small, the kinetic energy corresponding to the perturbation is a half of the total energy. Consequently,

$$K_{x,y} = \frac{1}{3}\big(\epsilon_0 + 2U_p cos^(\omega_0 t)\big) \tag{E.4}$$

Substituting Eq. (E.4) in Eq. (E.2),

$$\begin{aligned}&\frac{1}{2m}\Big(\hbar k_z - sign(q)2\sqrt{mU_p}cos(\omega_0 t)\Big)^2 + \frac{2}{3}\big(-\epsilon_0 + U_p cos^2(\omega_0 t)\big)\\ =\;& -\epsilon_0 + 2U_p cos^2(\omega_0 t)\end{aligned} \tag{E.5}$$

consequently

$$\begin{aligned}&\frac{1}{2m}\Big(\hbar k_z - sign(q)2\sqrt{mU_p}cos(\omega_0 t)\Big)^2 - \frac{4}{3}U_p cos^2(\omega_0 t) + \frac{\epsilon_0}{3} = 0\\ &\frac{\hbar^2 k_z^2}{2m} - sign(q)2\hbar k_z\sqrt{\frac{U_p}{m}}cos(\omega_0 t) + \frac{3}{3}U_p cos^2(\omega_0 t) + \frac{\epsilon_0}{3} = 0\end{aligned} \tag{E.6}$$

Considering

$$\Big\langle 2\hbar k_z\sqrt{\frac{U_p}{m}}cos(\omega_0 t)\Big\rangle = -sign(q)2\hbar k_z\sqrt{\frac{U_p}{m}}\frac{sin(\omega_0\delta t_s)}{\omega_0\delta t_s} \tag{E.7}$$

and

$$\big\langle 2U_p cos^2(\omega_0 t)\big\rangle = U_p + \frac{U_p}{2}\frac{sin(\omega_0\delta t_s)}{\omega_0\delta t_s} \tag{E.8}$$

we have

$$\frac{\hbar^2 k_z^2}{2m} + 2\hbar k_z\sqrt{\frac{U_p}{m}}\frac{sin(\omega_0\delta t_s)}{\omega_0\delta t_s} + \frac{U_p}{6}\frac{sin(2\omega_0\delta t_s)}{\omega_0\delta t_s} + \frac{\epsilon_0}{3} + \frac{U_p}{3} = 0 \tag{E.9}$$

$$\begin{aligned}\mathrm{k}_z =\;& \frac{2\sqrt{mU_p}\frac{sin(\omega_0\delta t_s)}{\omega_0\delta t_s}}{\hbar} + \frac{m}{\hbar^2}\sqrt{\left(2\hbar\sqrt{\frac{U_p}{m}}\frac{sin(\omega_0\delta t_s)}{\omega_0\delta t_s}\right)^2 - 4\frac{\hbar^2}{2m}\left(\frac{U_p}{6}\frac{sin(2\omega_0\delta t_s)}{\omega_0\delta t_s} + \frac{\epsilon_0}{3} + \frac{U_p}{3}\right)}\\ =& \text{-}2/\hbar\sqrt{mU_p}\frac{sin(\omega_0\delta t_s)}{\omega_0\delta t_s}\\ &+\left(\;2\hbar\frac{m}{\hbar^2}\sqrt{\frac{U_p}{m}}\left|\frac{sin(\omega_0\delta t_s)}{\omega_0\delta t_s}\right|\right)\sqrt{1-\frac{1}{6}\left(\frac{1}{2}\frac{sin(2\omega_0\delta t_s)}{\omega_0\delta t_s} + \frac{\epsilon_0}{U_p} + 1\right)\frac{1}{\left(\frac{sin(\omega_0\delta t_s)}{\omega_0\delta t_s}\right)^2}} =\\ &\text{-}2/\hbar\sqrt{mU_p}\frac{sin(\omega_0\delta t_s)}{\omega_0\delta t_s}\left[1{+}sign(sin(\omega_0\delta t))\sqrt{1-\frac{1}{6}\left(\frac{1}{2}\frac{sin(2\omega_0\delta t_s)}{\omega_0\delta t_s} + \frac{\epsilon_0}{U_p} + 1\right)\frac{1}{\left(\frac{sin(\omega_0\delta t_s)}{\omega_0\delta t_s}\right)^2}}\,\right]\end{aligned} \tag{E.10}$$

where, we have chosen the solution with the positive sign which reproduce better the 3D TDSE results.

Appendix F

Derivation VI

F.1 Derivation of Eq. (2.20)

Rewriting Eq. (2.16) as

$$a_d(t) = I_1 = \frac{1}{\hbar^2}\int_{t-\delta t_s}^{t} dt_2 \int_{t_0}^{t_2} dt_1 \langle\phi_0|G_a^-(t_0,t_2)\hat{Q}V_i(t_2)\hat{Q}G^-(t_2,t)\hat{Q}\hat{a}$$
$$\hat{P}G^+(t,t_1)\hat{P}V_i(t_1)\hat{Q}G_a^+(t_1,t_0)|\phi_0\rangle \qquad \text{(F.1)}$$

where we need to approximate the operators $\hat{Q}G^-(t_2,t)\hat{Q}$ and $\hat{Q}V_i(t_2)\hat{Q}$. On the one hand,

$$\hat{Q}G^-(t_2,t)\hat{Q} = i\hat{Q}e^{\frac{i}{\hbar}\int_{t_2}^{t}H(\tau)d\tau}\hat{Q} \approx i\hat{Q}e^{\frac{i}{\hbar}(\epsilon_0+\Delta_s)(t-t_2)}\hat{Q} \qquad \text{(F.2)}$$

due to

$$\hat{Q}H(\tau)\hat{Q} \approx \hat{Q}H_a + V_i\hat{Q} \approx \hat{Q}\langle H_a\rangle_{|\phi_0\rangle} + \Delta_s\hat{Q} = \hat{Q}\epsilon_0 + \Delta_s\hat{Q} \qquad \text{(F.3)}$$

On the other hand,

$$\hat{Q}V_i(t_2)\hat{Q} = \hat{Q}H - H_a\hat{Q} \approx \hat{Q}\frac{p^2}{2m} + \Delta_s - H_a\hat{Q} \qquad \text{(F.4)}$$

Substituting (F.2) and (F.4) in (F.1),

$$\begin{aligned} a_d(t) &= \frac{1}{\hbar^2}\int_{t-\delta t_s}^{t} dt_2 \int_{t_0}^{t_2} dt_1 \langle\phi_0|G_a^-(t_0,t_2)\hat{Q}\left(\frac{p^2}{2m}+\Delta_s-H_a\right) i\hat{Q}e^{\frac{i}{\hbar}(\epsilon_0+\Delta_s)(t-t_2)}\hat{Q}\hat{a} \\ &\quad \hat{P}G^+(t,t_1)\hat{P}V_i(t_1)\hat{Q}G_a^+(t_1,t_0)|\phi_0\rangle \\ &= \frac{1}{\hbar^2}\int_{t-\delta t_s}^{t} dt_2 \int_{t_0}^{t_2} dt_1 \langle\phi_0|G_a^-(t_0,t_2)e^{\frac{i}{\hbar}(\epsilon_0+\Delta_s)(t-t_2)}\hat{Q}\left(\frac{p^2}{2m}+\Delta_s-H_a\right)\hat{Q}\hat{a} \\ &\quad \hat{P}G^+(t,t_1)\hat{P}V_i(t_1)\hat{Q}G_a^+(t_1,t_0)|\phi_0\rangle \end{aligned} \tag{F.5}$$

Note that developing the bracket in Eq. (F.5) it splits in two terms. On the one hand,

$$\begin{aligned} &\frac{1}{\hbar^2}\int_{t-\delta t_s}^{t} dt_2 \int_{t_0}^{t_2} dt_1 \langle\phi_0|G_a^-(t_0,t_2)e^{\frac{i}{\hbar}(\epsilon_0+\Delta_s)(t-t_2)}\hat{Q}\big(\Delta_s-H_a\big)\hat{Q}\hat{a} \\ &\qquad\qquad \hat{P}G^+(t,t_1)\hat{P}V_i(t_1)\hat{Q}G_a^+(t_1,t_0)|\phi_0\rangle \end{aligned} \tag{F.6}$$

$$\begin{aligned} &= \frac{1}{\hbar^2}\int_{t-\delta t_s}^{t} dt_2 \int_{t_0}^{t_2} dt_1 \langle\phi_0|ie^{\frac{i}{\hbar}\epsilon_0(t_2-t_0)}e^{\frac{i}{\hbar}(\epsilon_0+\Delta_s)(t-t_2)}\hat{Q}\big(\Delta_s-H_a\big)\hat{Q}\hat{a} \\ &\qquad\qquad \hat{P}G^+(t,t_1)\hat{P}V_i(t_1)\hat{Q}G_a^+(t_1,t_0)|\phi_0\rangle \end{aligned} \tag{F.7}$$

$$\begin{aligned} &= \frac{-1}{\hbar^2}\int_{t-\delta t_s}^{t} dt_2 e^{\frac{i}{\hbar}\epsilon_0(t-t_0)}e^{\frac{i}{\hbar}\Delta_s(t-t_2)}\big(\Delta_s-\epsilon_0\big)\int_{t_0}^{t_2} dt_1 \langle\phi_0|\hat{a} \\ &\qquad\qquad \hat{P}G^+(t,t_1)\hat{P}V_i(t_1)\hat{Q}G_a^+(t_1,t_0)|\phi_0\rangle \end{aligned} \tag{F.8}$$

$$\begin{aligned} &= \frac{i}{\hbar}\int_{t-\delta t_s}^{t} dt_2 e^{\frac{i}{\hbar}\Delta_s(t-t_2)}\big(\Delta_s-\epsilon_0\big)\int_{t_0}^{t_2} dt_1 \langle\phi_0|G_a^-(t_0,t_2)\hat{a} \\ &\qquad\qquad \hat{P}G^+(t,t_1)\hat{P}V_i(t_1)\hat{Q}G_a^+(t_1,t_0)|\phi_0\rangle \end{aligned} \tag{F.9}$$

$$\begin{aligned} \approx \frac{i}{\hbar}\int_{t-\delta t_s}^{t} dt_2 e^{\frac{i}{\hbar}\Delta_s(t-t_2)}\big(\Delta_s-\epsilon_0\big)a_b(t) &= \big(\Delta_s-\epsilon_0\big)a_b(t)\frac{i}{\hbar}\frac{e^{-\frac{i}{\hbar}\Delta_s\delta t_s}-1}{\frac{i}{\hbar}\Delta_s} \\ &\approx -\left(1-\frac{\epsilon_0}{\Delta_s}\right)a_b(t) \end{aligned} \tag{F.10}$$

where we have approximate to 0 the value of the integral in the limit $t-\delta t_s$. It can be considered as a realistic approximation due to the wavefunction overlapping in the continuum, in this lapse of time just before the rescattering event, is negligible.

The other term in Eq. (F.5) can be written as,

$$\begin{multline}\frac{1}{\hbar^2}\int_{t-\delta t_s}^{t} dt_2 \int_{t_0}^{t_2} dt_1 \langle\phi_0|G_a^-(t_0,t_2)e^{\frac{i}{\hbar}(\epsilon_0+\Delta_s)(t-t_2)}\frac{p^2}{2m}\hat{Q}\hat{a} \\ \hat{P}G^+(t,t_1)\hat{P}V_i(t_1)\hat{Q}G_a^+(t_1,t_0)|\phi_0\rangle \tag{F.11}\end{multline}$$

at this point, and taking into account the approximation reported above we can consider as a valid the following commutation $\frac{p^2}{2m}\hat{Q}\hat{a} \longrightarrow \hat{Q}\hat{a}\frac{p^2}{2m}$. Substituting,

$$\begin{multline}\frac{1}{\hbar^2}\int_{t-\delta t_s}^{t} dt_2 \int_{t_0}^{t_2} dt_1 \langle\phi_0|G_a^-(t_0,t_2)e^{\frac{i}{\hbar}(\epsilon_0+\Delta_s)(t-t_2)}\hat{Q}\hat{a}\hat{P}\frac{p^2}{2m} \\ G^+(t,t_1)\hat{P}V_i(t_1)\hat{Q}G_a^+(t_1,t_0)|\phi_0\rangle \tag{F.12}\end{multline}$$

and using again the identity, $\int d\mathbf{k}|\mathbf{k}\rangle\langle\mathbf{k}| \equiv 1$,

$$\begin{multline}\frac{1}{\hbar^2}\int_{t-\delta t_s}^{t} dt_2 \int d\mathbf{k} \int_{t_0}^{t_2} dt_1 \langle\phi_0|G_a^-(t_0,t_2)e^{\frac{i}{\hbar}(\epsilon_0+\Delta_s)(t-t_2)}\hat{Q}\hat{a}|\mathbf{k}\rangle\langle\mathbf{k}|\hat{P}\frac{p^2}{2m} \\ G^+(t,t_1)\hat{P}V_i(t_1)\hat{Q}G_a^+(t_1,t_0)|\phi_0\rangle \tag{F.13}\end{multline}$$

Again this equation splits in two members. The term in the left-hand side can be written as a function of $a_b(\mathbf{k},t)$ and the term of the right-hand side, using the same criteria that in Eq. (F.10), can be approximated by $-\int d\mathbf{k}\frac{\hbar^2k^2/2m}{\Delta_s}$. Consequently,

$$\begin{aligned} a_d(t) &= -\int d\mathbf{k}\left[1-\frac{\epsilon_0}{\Delta_s}+\frac{\hbar^2k^2/2m}{\Delta_s}\right]a_b(\mathbf{k},t) \\ &= -\int d\mathbf{k}\left[1+\frac{\hbar^2k^2/2m-\epsilon_0}{\Delta_s}\right]a_b(\mathbf{k},t) \end{aligned} \tag{F.14}$$

Appendix F: Derivation of Eq. (2.20)

References

[1] T. H. Maiman, Nature, **187**, 493 (1960) 1

[2] D. Stickland and G. Mourou, Opt. Commun. **56**, 219 (1985) 1

[3] Gy. Farkas and Cs. Tóth, Phys. Lett. A **168**, 447-450 (1992) 12

[4] A. Baltuška, Th. Udem, M. Uiberacker, M. Hentschel, E. Goulielmakis, Ch. Gohle, R. Holzwarth, V. Yakovlev, A. Scrinzi, Th. W. Hnsch, and F. Krausz Nature **421**, 611 (2003) 1

[5] E. Goulielmakis, V. Yakovlev, A. Cavalieri, M. Uiberacker, V. Pervak, A. Apolonski, R. Kienberger, U. Kleineberg, and F. Krausz Science **317**, 769 (2007) 1

[6] N. H. Burnett, H. A. Baldis, M. C. Richardson, and G. D. Enright, Appl. Phys. Letters **31**, 172 (1977) 2

[7] A. McPherson, G. Gibson, H. Jara, U. Johann, T. S. Luk, I. A. McIntyre, K. Boyer, and C. K. Rhode, J. Opt. Soc. Am. B **21**, 595-601 (1987) 2

[8] M. Ferray, A. L'Huillier, X. F. Li, L. A. Lompre, G. Mainfray, and C. Manus, J. Phys. B: At. Mol. Opt. Phys. **21**, L31-L35 (1998) 2

[9] J. L. Krause, K. J. Schafer and K. C. Kulander, Phys. Rev. A **45**, 4998 (1992) 3

[10] K. C. Kulander, K. J. Schafer and J. L. Krause, M. Gavrila, (Ed.), 247300, Academic Press, ISBN 0-12-003901-X, New York, (1992) 3

[11] H. G. Muller, Laser Phys. **9**, 138148 (1999) 3

[12] D. Bauer and P. Koval, Comp. Phys. Comm. **174**, 396-421 (2006) 3

[13] S. Pabst and R. Santra, Phys. Rev. Lett. **111**, 233005 (2013) 3

[14] J. Rodríguez Vázquez de Aldana PhD Thesis, *Interaction of atoms with intense laser fields: theoretical study and numerical models* , Universidad de Salamanca (2001) 4

[15] M. Göppert-Mayer, Ann. Phys. **9**, 273 (1931) 4

[16] P. L. DeVries, J. Opt. Soc. Am. B **7**, 517 (1990) 5

[17] K. J. LaGattuta, J. Opt. Soc. Am. B **7**, 639 (1990) 5

[18] J. L. Krause, K. J. Schafer and K. C. Kulander, Phys. Rev. Lett. **68**, 3535-3538 (1992) 6, 8

[19] K. Schafer, B. Yang, L. F. DiMauro, and K. C. Kulander, Phys. Rev. Lett. **70**, 1599-1602 (1993) 6

[20] P. B. Corkum, Phys. Rev. Lett. **71**, 1994-1997 (1993) 6

[21] M. Lewenstein, Ph. Balcou, M. Yu. Ivanov, A. L'Huillier, P. B. Corkum, Phys. Rev. A **49**, 2117 (1994) 9, 11

[22] M. Hentschel, R. Kienberger, Ch. Spielmann, G. A. Reider, N. Milosevic, T. Brabec, P. Corkum, U. Heinzmann, M. Drescher and F. Kraus, Nature **414**, 509 (2001) 12

[23] P. M. Paul, E. S. Toma, P. Breger, G. Mullot, F. Aug, Ph. Balcou, H. G. Muller, and P. Agostini, Science **292**, 1689 (2001) 12

[24] M. Drescher, M. Hentschel, R. Kienberger, M. Uiberacker, V. Yakovlev, A. Scrinzi, Th. Westerwalbesloh, U. Kleineberg, U. Heinzmann and F. Krausz, Nature **419**, 803 (2002) 12

[25] Y. Mairesse, A. de Bohan, L. J. Frasinski, H. Merdji, L. C. Dinu, P. Monchicourt, P. Breger, M. Kovačev, R. Taïeb, B. Carré, H. G. Muller, P. Agostini, and P. Salières, Science **302**, 1540-1543 (2003) 12

[26] A. Zaïr, M. Holler, A. Guandalini, F. Schapper, J. Biegert, L. Gallmann, U. Keller, A. S. Wyatt, A. Monmayrant, and I. A. Walmsley, E. Cormier, T. Auguste, J. P. Caumes, and P. Salières, Phys. Rev. Lett. **100**, 143902 (2008) 12

[27] E. Goulielmakis, V. S. Yakovlev, A. L. Cavalieri, M. Uiberacker, V. Pervak, A. Apolonski, R. Kienberger, U. Kleineberg, and F. Krausz, Science **10**, 769-775 (2007) 12

[28] P. Salières, B. Carré, L. Le Déroff, F. Grasbon, G. G. Paulus, H. Walther, R. Kopold, W. Becker, D. B. Milŏsević, A. Sanpera and M. Lewenstein, Science **292**(5518) 902-905 (2001)

[29] J. D. Jackson, *Classical Electrodynamic Jonh Wiley and Sons* ISBN 0-471-43132-X (1975)

[30] V.P. Krainov, J. Opt. Soc. Am. B, **14**, 425 (1997) 19

[31] J. A. Pérez-Hernández, L. Roso and L. Plaja, Opt. Express **17**, 9891-9903 (2009) 21

[32] M. Janjusevic and Y. Hahn, J. Opt. Soc. Am. B **7**, 592-597 (1990) 22

[33] P. Krstić and M. H. Mittleman, J. Opt. Soc. Am. B **7**, 587-591 (1990) 22

[34] O. Smirnova, M. Spanner, and M. Ivanov, J. Phys. B: At. Mol. Opt. Phys. **39**, S307-321 (2006) 22

[35] M. V. Frolov, N. L. Manakov, and A. F. Starace, Phys. Rev. Lett. **100**, 173001-1-4 (2008) xvii, 22, 29, 30

REFERENCES

[36] M.V. Frolov N. L. Manakov, T. S. Sarantseva, M.Yu. Emelin, M.Yu. Ryabikin, and Anthony F. Starace, Phys. Rev. Lett. **102**, 243901 (2009) 22, 52

[37] A.-T. Le, T. Morishita and C. D. Lin, Phys. Rev. A **78**, 023814 (2008) 22, 60

[38] L.V. Keldysh, Zh. Eksp. Teor. Fiz. **47**, 1945 (1964) [Sov. Phys. JETP **20**, 1307 (1965)] 24

[39] P. Colosimo, G. Doumy, C. I. Blaga, J. Wheeler, C. Hauri, F. Catoire, J. Tate, R. Chirla, A. M. March, G. G. Paulus, H. G. Muller, P. Agostini, and L. F. Di Mauro, Nature Phys. **4**, 386-389 (2008) 28

[40] J. Tate, T. Auguste, H. G. Muller, P. Sali'eres, P. Agostini and L. F. Di Mauro, Phys. Rev. Lett. **98**, 013901 (2007) xvii, 29, 30, 31, 34, 52

[41] K. Schiessl, K. L. Ishikawa, E. Persson, J. Burgdöfer, Phys. Rev. Lett. **99**, 253903 (2007) xvii, xxvii, 29, 30, 31, 32, 52

[42] G. Sansone, E. Benedetti, F. Calegari, C. Vozzi, L. Avaldi, R. Flammini, L. Poletto, P. Villores, C. Altucci, R. Velotta, S. Stagira, S. De Silvestri, and M. Nisoli, Science **314**, 443-446 (2006) 29

[43] J. M. Combes, A. Grossmann, and Ph. Tchamitchian, in Wavelets (Springer-Verlag, Berlin, 1989) 36

[44] C. K. Chui, An Introduction to Wavelets, (Academic Press, New York, 1992) 36

[45] P. Antoine B. Piraux and A. Maquet, Phys. Rev. A **51**, 1750(R) (1995) 36

[46] X.-M. Tong and S.-I. Chu, Phys. Rev. A **61**, 021802(R) (2000) 36

[47] M. B. Gaarde, Opt. Express **8**, 529 (2001) 37

[48] P. Moreno, L. Plaja and L. Roso, *Laser Phys.* **7**, 602 (1997) 42, 53

[49] R. Numico, P. Moreno, L. Plaja and L. Roso, *J. Opt. Soc. Am. B* **31**, 4163 (1998) 42, 53

[50] X. M. Tong and C. D. Lin, J. Phys. B: At. Mol. Opt. Phys. **38**, 25932600 (2005) 47, 59

[51] E. Clementi and C. Roetti, Atomic data and nuclear data tables **14**, 177-478 (1974) 48

[52] Ph. Balcou, P. Salières and A. L'Huiller, Proceeding of a NATO Advanced Research Workshop on Super-Intense Laser-Atom Physics **316**, (1993). ISBN 0-306-44587-5 51

[53] J. A. Pérez-Hernández, L. Roso, A. Zaïr and L. Plaja, Opt. Express **19**, 19430-19439 (2011) 52, 84

[54] T. Popmintchev, M.C. Chen, A. Bahabad, M. Gerrity, P. Sidorenko, O. Cohen, I. P. Christov, M. M. Murnane, and H. C. Kapteyn, Proc. Natl. Acad. Sci. USA **106**, 10516 (2009) 52

[55] T. Popmintchev *et al.*, Science **336**, 1287 (2012) 52, 69

[56] L. E. Chippereld, J. S. Robinson, J. W. G. Tisch, and J. P. Marangos, Phys. Rev. Lett. **102**, 063003 (2009) 52, 61

[57] S. Haessler, T. Balčiūnas, G. Fan, T. Witting, R. Squibb, L. Chipperfield, A. Zar, G. Andriukaitis, A. Pugžlys, J. W. G. Tisch, J. P. Marangos, A. Baltuška, arXiv:1308.5510 (2012) 53

[58] J. J. Carrera, X. M. Tong and S-I. Chu, Phys. Rev. A **74**, 023404 (2006) 53

[59] Y. Oishi, M. Kaku, A. Suda, F. Kannari and K. Midorikawa, Opt. Express **14**, 7230 (2006)

[60] Z. Zeng, Y. Cheng, X. Song, X. Li and Z. Xu, Phys. Rev. Lett. **98**, 203901(2007)

[61] A. D. Bandrauk, S. Barmaki and G. L. Kamta, *Phys. Rev. Lett.* **98**, 013001 (2007) 53

[62] P. Moreno, L. Plaja, V. Malyshev, and L. Roso, Phys. Rev. A **51**, 4746-4753 (1995) 53

[63] V. V. Strelkov, A. F. Sterjantov, N. Yu Shubin, and V. T. Platonenko, J. Phys. B: At. Mol. Opt. Phys. **39**, 577-589 (2006) 53, 72

[64] J. A. Pérez-Hernández, D. J. Hoffmann, A. Zair, L. E. Chipperfield, L. Plaja, C. Ruiz, J. P. Marangos and L. Roso, J. Phys. B: At. Mol. Opt. Phys. **42**, 134004 (2009) 53

[65] M. Th. Hassan, A. Wirth, I. Grguras, A. Moulet, T. T. Luu, J. Gagnon, V. Pervak, and E. Goulielmakis, Rev. of Scientific Instruments **83**, 111301 (2012) 54

[66] J. W. Cooper, Phys. Rev. **128**, 681-693 (1962) 60

[67] H. J. Worner, H. Niikura, J. B. Bertrand, P. B. Corkum and D. M. Villeneuve, Phys. Rev. Lett. **102**, 103901 (2009) 60

[68] S. Baker, J. S. Robinson, C. A. Haworth, H. E. Teng, R. A. Smith, C. C. Chirilă, M. Lein, J. W. G. Tisch and J. P. Marangos, Science **312**, 424 (2006) 67

[69] M. F. Ciappina, J. Biegert, R. Quidant, M. Lewenstein, Phys. Rev. A **85**, 033828 (2012) 68

[70] M. F. Ciappina, J. A. Pérez-Hernández, T. Shaaran, J. Biegert, R. Quidant, M. Lewenstein, Physical Review A **86**, 023413 (2012) 68

[71] J. A. Pérez-Hernández, M. F. Ciappina, M. Lewenstein, L. Roso, A. Zaïr, Phys. Rev. Lett. **110**, 053001 (2013) 68

[72] H. Xiong, H. Xu, Y. Fu, J. Yao, B. Zeng, W. Chu, Y. Cheng, Z. Xu, E. J. Takahashi, K. Midorikawa, and X. Liu, and J. Chen, Opt. Lett. **34**, 17471749 (2009) 68

[73] P. Arpin, T. Popmintchev, N. L. Wagner, A. L. Lytle, O. Cohen, H. C. Kapteyn, and M. M. Murnane, Phys. Rev. Lett. **103**, 143901 (2009) 68

[74] M. Schnürer, Ch. Spielmann, P. Wobrauschek, C. Streli, N. H. Burnett, C. Kan, K. Ferencz, R. Koppitsch, Z. Cheng, T. Brabec, and F. Krausz, Phys. Rev. Lett. **80**, 3236-3239 (1998) 68

[75] K. T. Kim, C. M. Kim, M. G. Baik, G. Umesh, and C. H. Nam, Phys. Rev. A **69**, 051805(R) (2004) 68

[76] F. Ferrari, F. Calegari, M. Lucchini, C. Vozzi, S. Stagira, G. Sansone and M. Nisoli, Nat. Photonics **4**, 875-879 (2010) 68, 69

[77] M. Geissler, G. Tempea and T. Brabec, Phys. Rev. A **62**, 033817 (2000) 69

[78] J. Seres, E. Seres, A. J. Verhoef, G. Tempea, C. Streli, P. Wobrauschek, V. Yakovlev, A. Scrinzi, C. Spielmann and F. Krausz, Nature **433**, 596 (2005)

[79] E. Seres, J. Seres, C. Spielmann, Appl. Phys. Lett. **89**, 181919 (2006) 69

[80] J. Wu, H. Cai, A. Couairon and H. Zeng, Phys. Rev. A **80**, 013828 (2009) 69

[81] J. Wu, H. Cai, Y. Peng and H. Zeng, Phys. Rev. A **79**, 041404(R) (2009) 69

[82] H. Cai, J. Wu, Y. Peng, H. Zeng, Opt. Express **17**, 5822 (2009) 69

[83] H. Cai, J. Wu, X. Bai, H. Pan, H. Zeng Opt. Lett. **35**, 49 (2010) 69

[84] J. Vazquez de Aldana and L. Roso, Opt. Express **5**, 144-148 (1999) 74

[85] J. A. Pérez-Hernández, J. Ramos, L. Roso and L. Plaja, Laser Phys. **20**, 1044-1050 (2010)

[86] J. C. Baggesen and L. B. Madsen, J. Phys. B: At. Mol. Opt. Phys. **44**, 115601 (2011)

[87] D. J. Diestler, Phys. Rev. A **78**, 033814 (2008)

[88] E. Seres, J. Seres, F. Krausz and C. Spielmann, Phys. Rev. Lett. **92**, 143901 (2004) 77